Numerical Analysis of Friction Reduction due to Surface Textures in the Mixed Lubrication Regime

Zur Erlangung des akademischen Grades eines

Doktors der Ingenieurwissenschaften (Dr.-Ing.)

von der KIT-Fakultät für Maschinenbau des
Karlsruher Instituts für Technologie (KIT)
angenommene

Dissertation

von

M.Sc. Erik Arne Hansen

Tag der mündlichen Prüfung: 05.10.2023

Hauptreferentin: Prof. Dr.-Ing. Bettina Frohnapfel
Korreferent: Prof. Dr. Peter Gumbsch

Abstract

Surface texturing of lubricated tribological contacts is a promising technique for reducing energy losses and increasing machine efficiency. While the friction reducing mechanism of surface textures in the hydrodynamic lubrication regime has been well researched in the past, the experimentally observed friction reduction in the mixed lubrication regime has not yet been explained satisfactorily. In order to evaluate the suitability of numerical approaches for this problem, the still open question is analyzed whether simulations based on the Reynolds equation can be employed to investigate the experimentally observed friction reduction due to surface texturing in the mixed lubrication regime. The developed model is first employed in the hydrodynamic regime to identify the most accurate numerical discretization scheme in the case of textured surfaces. Gap heights measured in experiments with ball-on-disk tribometers are then used to validate the numerical approach for surface texture investigations. In the next step, a digital twin of a pin-on-disk tribometer is created by integrating real-life topographies into the numerical model. Subsequently, the friction behaviour of the developed digital twin is validated in the mixed lubrication regime with experimental Stribeck curves for untextured specimens. Moreover, it is shown that the hydrodynamic load carrying capacity of the tribological contact scales consistently with the dynamic viscosity of the lubricant, both experimentally and through simulations. Lastly, the impact of surface textures in the form of dimples is analyzed with the presented digital twin. The results confirm within the mixed lubrication regime that an increased hydrodynamic load carrying capacity can only be obtained when the inlet region of the lubricated contact is textured with dimple depths in the magnitude of the minimum gap height. At the same time, this cannot explain the experimentally observed friction reduction for fully textured surfaces with dimples that are significantly deeper than the minimum gap height. Thus, the current work suggests that this friction reduction might not be caused by a greater surface separation due to an increased load carrying capacity, but rather by a shift from dry to boundary friction in locally starved parts of the tribological contact.

Kurzfassung

Das Texturieren der Oberflächen von geschmierten tribologischen Kontakten ist eine vielversprechende Methode, um Energieverluste zu verringern und die Effizienz von Maschinen zu steigern. Während der reibungsreduzierende Mechanismus von Oberflächentexturen im hydrodynamischen Regime bereits ausführlich untersucht worden ist, kann die experimentell beobachtete Reibungsreduktion im Mischreibungsbereich bislang nicht zufriedenstellend erklärt werden. Um die Tauglichkeit numerischer Ansätze für dieses Problem zu beurteilen, wird im Rahmen dieser Dissertation die noch offene Frage analysiert, ob auf der Reynoldsgleichung basierende Simulationen eingesetzt werden können, um die experimentell beobachtete Reibungsreduktion aufgrund von Oberflächentexturen im Mischreibungsbereich zu untersuchen. Das entwickelte Modell wird zunächst im hydrodynamischen Regime verwendet, um das genaueste numerische Diskretisierungsschema im Fall von texturierten Oberflächen zu identifizieren. Anschließend werden Spalthöhenmessungen aus Experimenten mit Kugel-Scheibe Tribometern benutzt, um die numerische Herangehensweise für Untersuchungen von Oberflächentexturen zu validieren. Als nächster Schritt wird ein digitaler Zwilling eines Stift-Scheibe Tribometers erzeugt, indem Topografien der realen Probekörper in das numerische Modell integriert werden. Daraufhin wird das Reibverhalten des digitalen Zwillings im Mischreibungsbereich durch den Vergleich mit experimentellen Stribeck Kurven validiert. Außerdem wird im Fall von untexturierten Probekörpern mit Experimenten und Simulationen gezeigt, dass die hydrodynamische Tragfähigkeit des tribologischen Kontaktes konsistent mit der dynamischen Viskosität des Schmiermittels skaliert. Als letztes werden Oberflächentexturen in der Form von Näpfchen mit dem entwickelten digitalen Zwilling untersucht. Die Ergebnisse bestätigen im Mischreibungsbereich, dass eine Erhöhung der hydrodynamischen Tragfähigkeit nur erreicht werden kann, wenn die Einströmregion des geschmierten Kontaktes mit Näpfchentiefen in der Größenordnung der minimalen Spalthöhe texturiert wird. Dies kann jedoch die experimentell beobachtete Reibungsreduktion im Fall von vollständig texturierten Oberflächen mit Näpfchen, welche deutlich tiefer als die minimale Spalthöhe sind, nicht erklären. Daher wird in dieser Arbeit schlussendlich die Theorie vorgeschlagen, dass die Reibungsreduktion nicht durch eine größere Trennung der Oberflächen aufgrund einer erhöhten hydrodynamischen Tragfähigkeit, sondern stattdessen durch einen Übergang von Trocken- zu Grenzreibung in lokal mit Schmiermittel unterversorgten Bereichen des tribologischen Kontaktes verursacht wird.

Contents

1 Introduction

Friction phenomena have been scientifically investigated for hundreds of years, for example by Leonardo da Vinci, Guillaume Amontons, Charles-Augustin de Coulomb, Frank Philip Bowden or David Tabor [14]. However according to a review by Peter Jost [51], it was only in 1966 that the significant economic potential of implementing new technologies with the specific aim of friction reduction was evaluated for the first time. Consequently, the field of tribology was established and defined as the science and technology of interactive surfaces in relative motion [51]. This broad definition consolidates mechanical, thermal, environmental and electric effects that influence the friction of surface contacts, for example by means of lubrication, wear, corrosion or oxidation [88]. The associated technologies to reduce friction and wear focus on tailoring lubricants, materials and component designs to maximize the efficiency of machine elements [45]. This can be achieved by lubricant additives [82, 87] or catalytic elements in coatings or powders [10] that locally create tribofilms. Further technologies are the depositing of diamond-like carbon coatings [13, 99] or surface texturing [27]. In 2017, it was estimated that about 23% of the world's total energy consumption was used solely to overcome friction and wear [45]. Moreover, it was approximated that these losses could be potentially reduced by 40% in a course of 15 years by taking advantage of new tribological technologies [45]. On a global scale, this would result in a reduction of approximately 9% in the total energy consumption and annual financial savings of 1.4% in the gross domestic product [45]. Within this calculation, the transport sector was identified to show the largest potential for savings [45]. In the case of passenger cars, it is calculated that internal friction losses consume 16.5% of the fuel energy for vehicles with combustion engines [44] and 4% of the grid charging energy for battery powered electric cars [46]. Aiming at a further reduction of these losses, tribological technologies bear a considerable potential to save financial resources and reduce the emissions that are associated with fuel consumption and generation of electric energy [46].

1.1 Friction Reduction of Lubricated Contacts through Surface Texturing

Under lubricated conditions, the friction behaviour of a tribological contact can be quantified by the Stribeck curve [85], which plots the friction coefficient C_f of the contact as a function of the relative velocity U of the surfaces. The graph obtained is schematically depicted in red in Figure 1.1 and can be categorized into three regimes [82]:

1. For low velocities, the friction coefficient stays at a high and almost constant value. In this domain, the lubricant film is not capable of building up any significant fluid pressure. Thus, the friction behaviour is dominated by the contact of roughness asperities on the surfaces. This is referred to as boundary lubrication.
2. For further increasing velocities, a sudden steep drop of the friction coefficient occurs. This happens because the fluid pressure is growing strong enough to increasingly separate the surfaces. The remaining part of the contact load is still carried by the surface contact of roughness asperities, which dominate the friction behaviour. This regime is called mixed lubrication.

3. If U keeps increasing, a minimum of the friction coefficient will be passed and C_f will rise with the velocity. In this domain, both surfaces are completely separated by the lubricant film. Thus, the full-film regime of hydrodynamic lubrication is reached.

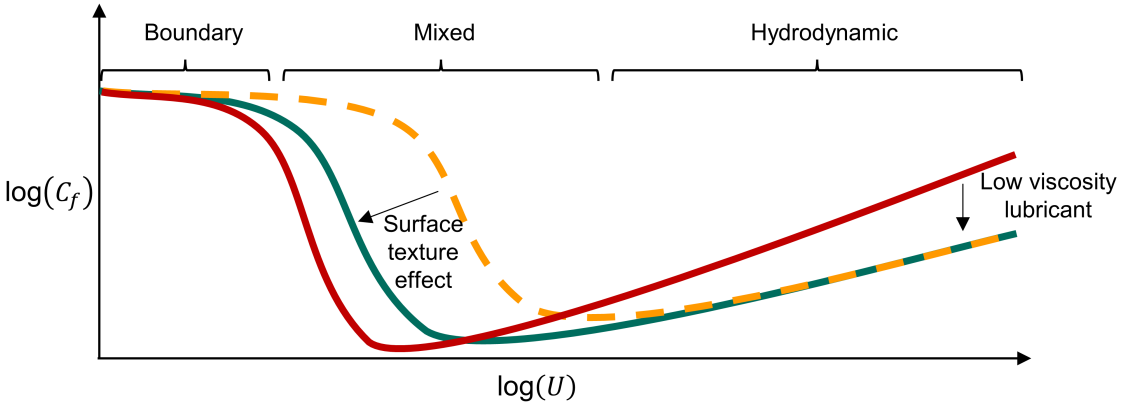

Figure 1.1: Schematic sketch of a Stribeck curve when the dynamic viscosity is decreased and surface textures are added.

Within the hydrodynamic regime, the friction can be easily reduced by employing lubricants with a lower dynamic viscosity, thus reducing for example churning or pumping losses of a machine [83]. At the same time, the lubricant's load carrying capacity decreases which results in a lower surface separation and a shift of the mixed lubrication regime towards higher velocities. Both effects are visualized by the yellow curve in Figure 1.1. Depending on the operating speed, a lower dynamic viscosity can consequently either lead to lower or higher losses, for example in the journal bearings of a lubricated system.

As shown by the green curve in Figure 1.1, this can be partially rectified by applying surface textures within the tribological contact since they have shown to decrease the friction in the mixed lubrication regime [54]. Thus, the advantageous properties of low viscosity lubricants can be utilized in the hydrodynamic regime while their detrimental effects in the mixed lubrication regime can be weakened. Considering whole lubricated systems (such as engines) that contain multiple components which operate at the same time in different regimes of the Stribeck curve, the right combination of low dynamic viscosity and surface texturing can integrally lead to a friction reduction of the whole machine. However, the proper design of the surface textures is all but straight forward since wrongly sized textures can also result in friction increase [59].

Achieving friction reduction in lubricated contacts through surface texturing has gained a significant amount of attention in the tribology community in the recent decades [27, 36, 37, 59, 2, 61]. As employed texture shape, microscopic dimples were firstly suggested by Etsion and Burstein in 1996 [28]. The advantage of this shape is that it can be easily produced in large quantities with laser surface texturing [27] and that the created textures have shown to reduce friction in the mixed lubrication regime significantly [54]. Previously suggested explanations for this friction reduction are that the dimples can act as lubricant reservoirs to prevent starvation [36], entrap wear debris [36], cause a smaller contact area resulting in less adhesion during boundary lubrication [36, 2] and increase the hydrodynamic lift of the lubricant flow [40, 36].

1.2 Research Question and Approach

In particular, the improvement of the hydrodynamic lift has been studied extensively in the literature, mostly using simulations [36]. Studies investigating the optimum dimple parameters to maximize the efficiency of surface textures are mainly carried out in the hydrodynamic lubrication regime under conditions where the dimple depth is of a similar magnitude to the minimum gap height. Under these conditions, it has been demonstrated in the literature that based on the Reynolds equation [72], the maximum hydrodynamic lift is achieved by approximating a Rayleigh step through texturing of the contact's inlet region [23, 36]. This optimum Rayleigh step shape can even be described by an analytical solution for a two-dimensional flow [41, Ch. 8.6]. In more realistic three-dimensional problems, the Rayleigh step must also be bounded at the sides to prevent side leakage [20].

While this mechanism is generally understood, problems arise when the results obtained are used to explain the friction reduction due to the surface textures in the mixed lubrication regime with higher load carrying capacities [19]. The reason for this is first that simulations of fully textured surfaces generally result in a load carrying decrease [19] while fully textured surfaces have proven in experiments to be capable of significant friction reduction [16, 79]. The second reason is that surface contact occurs when the minimum gap height approaches the roughness height, which is usually much smaller than the optimum texture depth determined experimentally [16, 79]. At the same time, the results obtained by simulations in the hydrodynamic regime suggest that the optimum dimple depths should rather be of the same magnitude as the minimum gap height [19], thus creating a contradiction with the experimentally observed friction reduction in the mixed lubrication regime.

Due to a lack of complementary simulations of textured surfaces in the mixed lubrication regime, it is currently not clear whether this contradiction can eventually be resolved. At the same time, resolving this contradiction is a fundamental requirement in order to legitimize simulations based on the Reynolds equation for numerical investigations which optimize the dimple shape or aim at understanding the underlying mechanism of the friction reduction. The novelty of the present thesis is to close this knowledge gap by performing a numerical analysis of textured surfaces in the mixed lubrication regime in order to address the following research question: can simulations based on the Reynolds equation be employed to investigate the experimentally observed friction reduction due to surface texturing in the mixed lubrication regime?

During the conducted analysis in this dissertation, the surface textures are examined in tribometers which artificially replicate the tribological contact conditions within certain machine elements. For example, ball-on-disk tribometers reflect the non-conformal contacts within ball bearings while pin-on-disk tribometers relate to the conformal contacts within journal bearings. As this procedure isolates the tribological contact from the rest of the machine element, it allows the conditions within the tribological contact to be more accurately controlled and monitored. Furthermore, any changes in the friction behaviour can be traced directly to the tribological contact because interfering effects introduced by other components are minimized. Ultimately, this allows to analyze, identify and understand the different physical phenomena responsible for changes in the friction behaviour.

The chosen approach to tackle the research question within this thesis is divided into the following steps. As the basis of this numerical work, the employed fundamental model of a generalized lubricated contact within a pin-on-disk tribometer is presented in Chapter 2. The model is able to account for the interplay between piezoviscosity, compressibility, cavitation, elastic deformation and fluid pressure using the Reynolds equation. By additionally incorporating roughness effects on the fluid and contact

pressure, the two-scale model eventually provides a closed system of equations to compute the Stribeck curve over the whole range from the boundary through mixed to the hydrodynamic lubrication regime.

Chapter 3 presents the algorithms of two newly developed solvers for the assembled system of equations. The first one is the elasto-hydrodynamic lubrication - Fischer-Burmeister-Newton-Schur (EHL-FBNS) solver. It describes the computation of the fluid pressure distribution in the hydrodynamic regime and is subsequently extended to the homogenized mixed-elasto-hydrodynamic lubrication - Fischer-Burmeister-Newton-Schur (HMEHL-FBNS) solver to provide the friction coefficient over all lubrication regimes of the Stribeck curve.

The EHL-FBNS solver is then used in Chapter 4 to identify the best discretization scheme for the most accurate numerical solution of the discontinuous gap profiles caused by surface textures. Moreover, it is used to evaluate the applicability of the Reynolds equation by comparing the simulation results to measured gap heights of ball-on-disk tribometer experiments for cases in which the dimple depth is significantly larger than the minimum gap height. While this has not been possible with previously existing tools, it is shown that such geometries can be simulated by means of the EHL-FBNS solver.

With the knowledge gained, the HMEHL-FBNS solver is employed in Chapter 5 to create a digital twin of a pin-on-disk tribometer with untextured specimens. After a brief description of the experimental procedure, the virtual reconstruction of the tribological contact with real-life post-test topographies is described. To validate this novel approach, the Hersey number of a pin-on-disk tribometer is derived and the agreement of the simulation results with the experiments is analyzed by comparing the Stribeck curves for untextured specimens.

A literature review of the current knowledge on friction reduction through surface texturing is presented at the beginning of Chapter 6. Afterwards, surface textures are applied to the previously developed digital twin and simulations are performed for different texturing patterns and texture dimensions. Lastly, the numerical findings are compared with experimental results. This will ultimately allow to discuss whether simulations based on the Reynolds equation can be employed to investigate the experimentally observed friction reduction due to surface texturing in the mixed lubrication regime.

Chapters 3, 4 and 5 contain direct quotations from journal articles by [Hansen et al., 2022] and [Hansen et al., 2023]. Furthermore, Chapters 5 and 6 are put into context with a journal article by [Hansen et al., 2020]. The articles have been previously published by the author of this thesis. While the quotations are highlighted and major changes to the original version are marked, the nomenclature is adjusted without further comment to be consistent within the present dissertation. The real-life experiments of the publication by [Hansen et al., 2023] were conducted by the co-author of the article, Gerda Vaitkunaite, at the Institute of Reliability and Microstructure (IAM-ZM) and are not a direct part of this thesis but are used as references for the comparison with the simulations. The scientific color map batlow is used for several figures in this thesis to avoid visual distortion of the data and not to exclude readers with colour-vision deficiencies [21].

2 Fundamental Model

In this chapter, the fundamental model of a generalized lubricated tribological contact within a pin-on-disk tribometer is presented. The aim of the model is to provide a closed system of equations that allows to compute the Stribeck curve for any gap geometry. Furthermore, this chapter exhibits all of the assumptions incorporated within the model to facilitate further discussions about their validity in later chapters.

2.1 Friction Coefficient of a Pin-on-Disk Tribometer

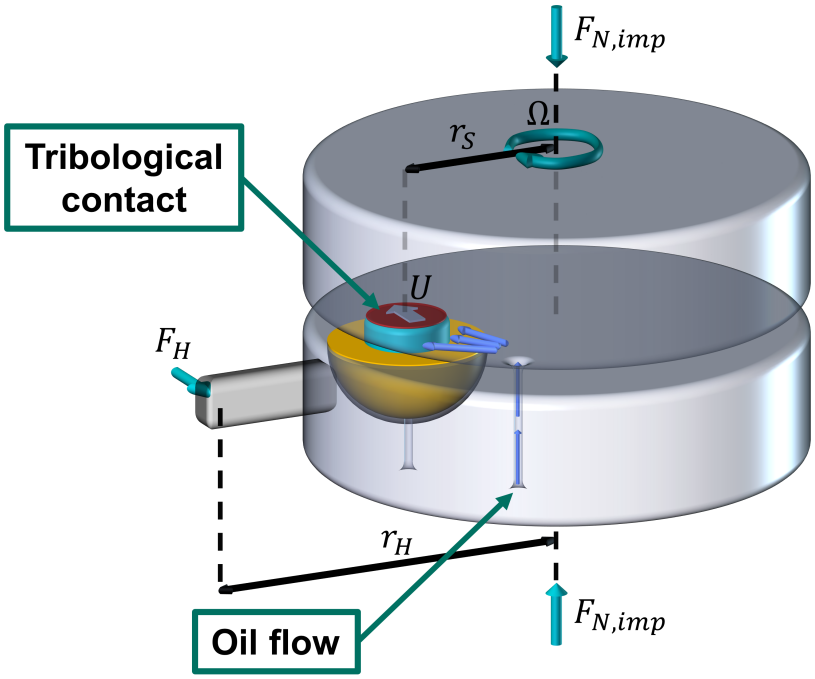

Figure 2.1: Schematic sketch of a pin-on-disk tribometer.

A pin-on-disk tribometer is schematically depicted in Figure 2.1. It consists of a pin that is mounted at the sliding radius r_S on a lower base plate. Additionally, a rotating disk is pressed against the pin with an imposed normal load $F_{N,imp}$. The angular velocity Ω of the disk induces the sliding velocity $U = \Omega r_S$ in the tribological contact between pin and disk. In front of the pin, an opening in the base plate supplies a constant oil flow which is drawn into the tribological contact by the rotating disk. The base plate is prevented from following the rotation of the disk by a holding force F_H that is measured at the holding radius r_H. This allows to deduce the friction force F_T transmitted by the tribological contact through a torque balance:

$$F_T = \frac{r_H}{r_S} F_H. \tag{2.1}$$

This friction force is used to define the friction coefficient as:

$$C_f = \mathrm{abs}\left(\frac{F_T}{F_{N,imp}}\right). \tag{2.2}$$

In order to simulate complementary Stribeck curves, it is necessary to establish a model that provides a closed system of equations to compute the above described friction force at the imposed normal load. These equations are derived in the following for a generalized lubrication gap such that they can be applied subsequently to specific applications like a pin-on-disk tribometer.

2.2 Load and Friction Force

First, the imposed normal load $F_{N,imp}$ is required to be met by the normal force F_N that is transmitted through the tribological contact area A_{trib}, excluding the contribution of the ambient pressure p_{amb}. This defines the load balance equation (LBE) as:

$$F_{N,imp} \stackrel{!}{=} F_N(p_{tot}) = \iint\limits_{A_{trib}} p_{tot} - p_{amb} \mathrm{d}x_2 \mathrm{d}x_1, \tag{2.3}$$

where $p_{tot}(x_1, x_2)$ is the total pressure at any position (x_1, x_2) within the tribological contact. The employed cartesian coordinate system will be elaborated in more detail in the next section. The friction force acting on the lower surface can be computed analogously by integrating the total tangential stress τ_{tot}:

$$F_T(\tau_{tot}) = \iint\limits_{A_{trib}} \tau_{tot} \mathrm{d}x_2 \mathrm{d}x_1. \tag{2.4}$$

2.3 Generalized Lubrication Gap

The generalized lubrication gap is schematically depicted in Figure 2.2 and consists of an upper and a lower surface that move with their individual velocities U_{up} and U_{low} along x_1-direction. The gap in between is filled with a lubricant whose fluid pressure p_{fl} acts upon both surfaces. At some positions, the surfaces get into contact with each other and directly exert the contact pressure p_{con} upon each other. At each time t and each position (x_1, x_2), the x_3-coordinate of the upper and lower surface is denoted by z_{up} and z_{low}. This allows the gap height to be expressed as $h(x_1, x_2, t) = z_{up}(x_1, x_2, t) - z_{low}(x_1, x_2, t)$.

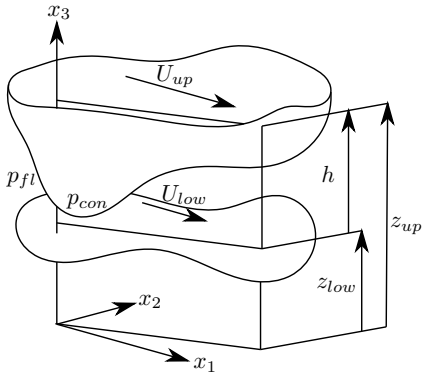

Figure 2.2: Schematic sketch of a generalized lubrication gap. The figure is adapted from the publication by [Hansen et al., 2022].

As will be shown later in Section 2.6, it is eventually sufficient to consider only the resulting gap height h instead of treating the upper and lower surface separately. Sticking to this concept, the gap height can be expressed as [41, Ch. 19.2]:

$$h = h_d + h_{ri} + h_{el}, \tag{2.5}$$

where h_d describes the rigid body displacement of both surfaces and h_{ri} represents the variation of the gap height due to the shape of the rigid profiles. Furthermore, $h_{el}(p_{tot})$ denotes the elastic gap height deformation due to the fluid and contact pressure, whose superposition is denoted as the total pressure:

$$p_{tot} = p_{fl} + p_{con}. \tag{2.6}$$

Analogously, the total tangential stress τ_{tot} can be decomposed into a contribution due to the viscous stress of the fluid $\tau_{fl,1}$ and the tangential stress due to surface contact $\tau_{con,1}$ acting at the lower surface in x_1-direction:

$$\tau_{tot} = \tau_{fl,1}\big|_{x_3=z_{low}} + \tau_{con,1}\big|_{x_3=z_{low}}. \tag{2.7}$$

2.4 Conservation Equations of a Contiunuum

Equations to compute the stresses and deformations within the considered lubrication gap can be derived when both the solid and fluid are treated as respective continua. In this case, it is possible to describe the behaviour of each continuum at any time t and any position (x_1, x_2, x_3) within a cartesian coordinate system by the differential form of conservation laws. The first conservation law is the equation of mass conservation [84, Ch. 2.1, P. 37]:

$$\frac{\partial \rho}{\partial t} + \frac{\partial}{\partial x_i}(\rho u_i) = 0, \tag{2.8}$$

where ρ is the density and the velocity components are denoted by u_i with $i = 1, 2, 3$. As a second conservation law, for $j = 1, 2, 3$ the three equations of momentum conservation read [84, Ch. 2.2, P. 45]:

$$\rho \frac{\mathrm{d}u_j}{\mathrm{d}t} = \rho k_j + \frac{\partial \sigma_{ij}}{\partial x_i}, \tag{2.9}$$

where $\frac{\mathrm{d}u_j}{\mathrm{d}t} = \frac{\partial u_j}{\partial t} + u_i \frac{\partial u_j}{\partial x_i}$ is the total derivative of u_j, while k_j provides the components of the gravitational acceleration and σ_{ij} denotes the stress tensor. As a consequence of the additional law of angular momentum conservation, it can be proven that the stress tensor is symmetric $\sigma_{ij} = \sigma_{ji}$ [84, Ch. 2.3, P. 49]. It should be noted that Equations (2.8) and (2.9) are generally valid for the continuum of either a fluid or a solid, but the stress tensor σ_{ij} depends on the aggregate phase of the respective continuum. As detailed in the next sections, σ_{ij} is either a function of the velocity components u_i or the displacement components v_i.

2.5 Gap Height Deformation

In this section, the deformation of the upper and lower surfaces due to the total pressure within the lubrication gap is derived from the equations of momentum conservation. Assuming a static continuum for the solid, Equation (2.9) reduces to [12, Ch. 4.1, P. 197]:

$$0 = \rho k_j + \frac{\partial \sigma_{ij}}{\partial x_i}. \tag{2.10}$$

First, an expression for the stress tensor is required. According to Hooke's law, the stress tensor σ_{ij} is proportional to the strain tensor $e_{sl,ij}$. For small displacements v_i, the strain tensor can by provided by [12, Ch. 4.1, P. 167]:

$$e_{sl,ij} = \frac{1}{2}\left(\frac{\partial v_i}{\partial x_j} + \frac{\partial v_j}{\partial x_i}\right). \tag{2.11}$$

In the case of an isotropic elastic material, the stress tensor can then be expressed by the following material law [12, Ch. 4.1, P. 183]:

$$\sigma_{ij} = \frac{E}{1+\nu}\left(e_{sl,ij} + \frac{\nu}{1-2\nu} e_{sl,kk}\delta_{ij}\right), \tag{2.12}$$

where δ_{ij} denotes the Kronecker delta and Young's modulus E and Poisson ratio ν are material specific parameters. Substituting this expression into the Equation (2.10) results in Navier's displacement equations (NDE) [12, Ch. 4.1, P. 199], [55, Ch. 7, P. 18]:

$$\frac{\partial^2 v_j}{\partial x_k \partial x_k} + \frac{1}{1-2\nu}\frac{\partial^2 v_k}{\partial x_j \partial x_k} = -\frac{2(1+\nu)}{E}\rho k_j. \tag{2.13}$$

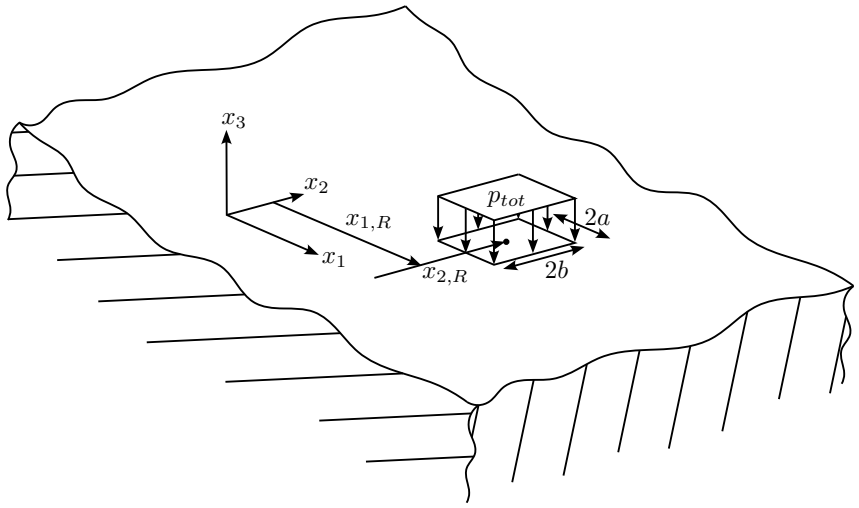

Figure 2.3: Schematic sketch of an elastic half-space that is subjected to a constant total pressure over a rectangular surface.

In order to find an analytical expression for the surface displacement, the upper and the lower surfaces are respectively approximated as an elastic half-space as shown in Figure 2.3. When the gravitational term is neglected and the elastic half-space is subjected to the total pressure p_{tot} acting on its surface, the following analytical expression of the surface displacement $v_3|_{x_3=0}$ at any position (x_1, x_2) can be derived by potential theory [65] from the NDE [55, Ch. 8, P. 28-29], [70]:

$$v_3|_{x_3=0} = \frac{1-\nu^2}{\pi E} \int_{-\infty}^{\infty}\int_{-\infty}^{\infty} \frac{p_{tot}(x_1', x_2')}{\sqrt{(x_1 - x_1')^2 + (x_2 - x_2')^2}} \mathrm{d}x_2' \mathrm{d}x_1'. \tag{2.14}$$

This equation can be further specified in the case that p_{tot} is constant across the rectangular area $x_{1,R} - a \leq x_1 \leq x_{1,R} + a$ and $x_{2,R} - b \leq x_2 \leq x_{2,R} + b$, where the center of the rectangle is at position $(x_{1,R}, x_{2,R})$. Outside of the rectangle, the total pressure p_{tot} is zero. Under these conditions, the equation above becomes [49, Ch. 3.3, P. 54], [65]:

$$\begin{aligned} v_3|_{x_3=0} =& \frac{1-\nu^2}{\pi E} \int_{x_{1,R}-a}^{x_{1,R}+a}\int_{x_{2,R}-b}^{x_{2,R}+b} \frac{1}{\sqrt{(x_1 - x_1')^2 + (x_2 - x_2')^2}} \mathrm{d}x_2' \mathrm{d}x_1' p_{tot}(x_{1,R}, x_{2,R}) \\ =& \frac{1-\nu^2}{\pi E} K(x_1 - x_{1,R}, x_2 - x_{2,R}) p_{tot}(x_{1,R}, x_{2,R}), \end{aligned} \tag{2.15}$$

where the kernel K is a function of the distances to the center of the rectangle $\tilde{x}_1 = x_1 - x_{1,R}$ and $\tilde{x}_2 = x_2 - x_{2,R}$ [49, Ch. 3.3, P. 54], [65]:

$$\begin{aligned} K(\tilde{x}_1, \tilde{x}_2) = & \left((\tilde{x}_1 + a) \ln \left(\frac{(\tilde{x}_2 + b) + \sqrt{(\tilde{x}_2 + b)^2 + (\tilde{x}_1 + a)^2}}{(\tilde{x}_2 - b) + \sqrt{(\tilde{x}_2 - b)^2 + (\tilde{x}_1 + a)^2}} \right) \right. \\ & + (\tilde{x}_2 + b) \ln \left(\frac{(\tilde{x}_1 + a) + \sqrt{(\tilde{x}_2 + b)^2 + (\tilde{x}_1 + a)^2}}{(\tilde{x}_1 - a) + \sqrt{(\tilde{x}_2 + b)^2 + (\tilde{x}_1 - a)^2}} \right) \\ & + (\tilde{x}_1 - a) \ln \left(\frac{(\tilde{x}_2 - b) + \sqrt{(\tilde{x}_2 - b)^2 + (\tilde{x}_1 - a)^2}}{(\tilde{x}_2 + b) + \sqrt{(\tilde{x}_2 + b)^2 + (\tilde{x}_1 - a)^2}} \right) \\ & \left. + (\tilde{x}_2 - b) \ln \left(\frac{(\tilde{x}_1 - a) + \sqrt{(\tilde{x}_2 - b)^2 + (\tilde{x}_1 - a)^2}}{(\tilde{x}_1 + a) + \sqrt{(\tilde{x}_2 - b)^2 + (\tilde{x}_1 + a)^2}} \right) \right). \end{aligned} \tag{2.16}$$

Keeping in mind that the combined displacement of the upper and lower surface is the eventually desired quantity and considering that both surfaces behave analogously, the combined displacement reads:

$$\begin{aligned} v_3' &= \left(\frac{1-\nu_{low}^2}{\pi E_{low}} + \frac{1-\nu_{up}^2}{\pi E_{up}} \right) K(x_1 - x_{1,R}, x_2 - x_{2,R}) p_{tot}(x_{1,R}, x_{2,R}) \\ &= \frac{2}{\pi E'} K(x_1 - x_{1,R}, x_2 - x_{2,R}) p_{tot}(x_{1,R}, x_{2,R}), \end{aligned} \tag{2.17}$$

where the reduced elastic modulus is defined as [89, Ch. 1.3.5]:

$$E' = \frac{2}{\frac{1-\nu_{low}^2}{E_{low}} + \frac{1-\nu_{up}^2}{E_{up}}}. \tag{2.18}$$

So far, only the displacement due to one rectangle of constant total pressure was considered. Superimposing the displacements due to $N_{x_1,R}N_{x_2,R}$ rectangles eventually allows to express the gap height deformation h_{el} at any position (x_1, x_2) and time t as a function of a variable total pressure field that is discretized into said rectangles [Hansen et al., 2022]:

$$\begin{aligned} h_{el}(x_1, x_2, t) &= \sum^{N_{x_1,R}} \sum^{N_{x_2,R}} v_3' \\ &= \sum^{N_{x_1,R}} \sum^{N_{x_2,R}} \frac{2}{\pi E'} K(x_1 - x_{1,R}, x_2 - x_{2,R}) p_{tot}(x_{1,R}, x_{2,R}, t). \end{aligned} \tag{2.19}$$

2.6 Reynolds Equation

In this section, the Reynolds equation [72] is derived from the equations of mass and momentum conservation. The Reynolds equation is of great importance because it allows to compute the fluid pressure within the lubrication gap at significantly lower computational costs than the complete Navier-Stokes equations (NSE) and it can be coupled easily with the previously introduced gap height deformation. Considering the lubricant as a fluid continuum, the equation of momentum conservation (2.9) can be reformed using the total derivative:

$$\rho \frac{\mathrm{d}u_j}{\mathrm{d}t} = \rho \left(\frac{\partial u_j}{\partial t} + u_i \frac{\partial u_j}{\partial x_i} \right) = \rho k_j + \frac{\partial \sigma_{ij}}{\partial x_i}. \tag{2.20}$$

Furthermore, the stress tensor can be divided into a contribution due to the fluid pressure p_{fl} and the viscous stress tensor τ_{ij} [84, Ch. 2.2],[78, Ch. 3.4, P. 56-57]:

$$\sigma_{ij} = -p_{fl}\delta_{ij} + \tau_{ij}, \tag{2.21}$$

Assuming a Newtonian fluid behaviour, the viscous stress tensor is proportional to the strain rate tensor $e_{fl,ij}$ [78, P. 5,63-64]:

$$e_{fl,ij} = \frac{1}{2} \left(\frac{\partial u_i}{\partial x_j} + \frac{\partial u_j}{\partial x_i} \right). \tag{2.22}$$

For an isotropic Newtonian fluid, the stress tensor can then eventually be provided by the following material law [78, P. 63,65-66]:

$$\sigma_{ij} = -p_{fl}\delta_{ij} - \frac{2}{3}\mu e_{fl,kk}\delta_{ij} + 2\mu e_{fl,ij}, \tag{2.23}$$

where μ denotes the dynamic viscosity. Substituting the obtained stress tensor into the equations of momentum conservation (2.20) yields the NSE [78, P. 68]:

$$\rho \left(\frac{\partial u_j}{\partial t} + u_i \frac{\partial u_j}{\partial x_i} \right) = \rho k_j - \frac{\partial}{\partial x_j} \left(p_{fl} + \frac{2}{3}\mu \frac{\partial u_k}{\partial x_k} \right) + \frac{\partial}{\partial x_i} \left(\mu \left(\frac{\partial u_i}{\partial x_j} + \frac{\partial u_j}{\partial x_i} \right) \right). \tag{2.24}$$

In order to simplify the mathematical problem by reducing it only to its dominant terms, an order of magnitude analysis can be performed for the considered lubrication gap. To do so, mass conservation and NSE are first put into dimensionless form by decomposing quantities into their dimensionless value

and their dimensional reference value, respectively denoted by the upper index * and lower index $_{ref}$ [41, Ch. 7.2]:

$$\begin{aligned}
&x_1 = x_1^* x_{1,ref}; \quad x_2 = x_2^* x_{2,ref}; \quad x_3 = x_3^* x_{3,ref}; \quad t = t^* t_{ref};\\
&u_1 = u_1^* u_{1,ref}; \quad u_2 = u_2^* u_{2,ref}; \quad u_3 = u_3^* u_{3,ref};\\
&k_1 = k_1^* k_{1,ref}; \quad k_2 = k_2^* k_{2,ref}; \quad k_3 = k_3^* k_{3,ref};\\
&p_{fl} = p_{fl}^* p_{ref}; \quad \rho = \rho^* \rho_{ref}; \quad \mu = \mu^* \mu_{ref}.
\end{aligned} \tag{2.25}$$

For narrow lubricated gaps, some reference quantities can be directly estimated from the geometry sizes and operating conditions:

$$\begin{aligned}
&x_{1,ref} = L; \quad x_{2,ref} = L;\\
&x_{3,ref} = H; \quad t_{ref} = \frac{L}{U};\\
&u_{1,ref} = U; \quad u_{2,ref} = U;\\
&k_{1,ref} = g; \quad k_{2,ref} = g; \quad k_{3,ref} = g;\\
&\rho_{ref} = \rho_0; \quad \mu_{ref} = \mu_0,
\end{aligned} \tag{2.26}$$

where U is a characteristic velocity of the fluid, L a characteristic length in the direction of U, H a characteristic gap height, g the gravitational acceleration, ρ_0 the density of the lubricant's liquid phase at ambient pressure and μ_0 the dynamic viscosity of the lubricant's liquid phase at ambient pressure. Using the same dimensional values L, U and g for different components of some reference quantities allows a generalization of the following considerations for any alignment of the velocity U within the x_1-x_2-plane and any direction of the gravitational field. The reference quantities $u_{3,ref}$ and p_{ref} remain unknown for now because their values arise as a consequence of the imposed operating conditions to keep the system of equations in equilibrium. Subsequently, this means that they can be deduced from said equations. Inserting the decompositions of the equation set (2.25) and the estimated reference values of equation set (2.26) into the equation of mass conservation (2.8) yields after multiplication with $L/(U\rho_0)$:

$$\frac{\partial \rho^*}{\partial t^*} + \frac{\partial}{\partial x_1^*}\left(\rho^* u_1^*\right) + \frac{\partial}{\partial x_2^*}\left(\rho^* u_2^*\right) + \frac{u_{3,ref} L}{UH}\frac{\partial}{\partial x_3^*}\left(\rho^* u_3^*\right) = 0. \tag{2.27}$$

If the reference values are estimated adequately for the considered problem, the dimensionless quantities turn out to be of magnitude 1. Assuming that this still holds when derivatives are applied, the magnitude of each term is solely defined by its remaining coefficient. In the general case where none of the terms in the mass conservation can be neglected, all terms are of magnitude 1. This in turn allows to deduce the magnitude of $u_{3,ref}$ from equation (2.27) as:

$$u_{3,ref} = \frac{UH}{L}. \tag{2.28}$$

The same approach can be applied to the NSE (2.24). Once they are additionally multiplied with $H^2/(\mu_0 U)$, some coefficients can be expressed by the Reynolds number $Re = \rho_0 UH/\mu_0$, Froude number $Fr = U^2/(gL)$ and Euler number $Eu = p_{ref}/(\rho_0 U^2)$. The subsequent step is to identify negligible terms with an order of magnitude analysis as shown in Equations (2.29-2.31). For lubrication problems with narrow gaps, the relation between gap height and length is commonly $H/L \ll 1$, which allows to neglect most of the viscous terms except for the ones of magnitude 1. If additionally $ReH/L \ll 1$ holds,

the inertial terms can be neglected in comparison to the largest viscous terms. If lastly also $Fr > 1$ holds, then the gravitational terms are even smaller than the inertial terms and also negligible. The applicability of the simplifications in case of the pin-on-disk tribometer can be confirmed through the characteristic values provided in table 2.1.

x_1^*-direction :

$$\cancel{Re}\,\cancel{\frac{H}{L}}\,\rho^*\left(\frac{\partial u_1^*}{\partial t^*}+u_1^*\frac{\partial u_1^*}{\partial x_1^*}+u_2^*\frac{\partial u_1^*}{\partial x_2^*}+u_3^*\frac{\partial u_1^*}{\partial x_3^*}\right)=\cancel{\frac{Re}{Fr}}\,\cancel{\frac{H}{L}}\,\rho^* k_1^*-EuRe\frac{H}{L}\frac{\partial p_{fl}^*}{\partial x_1^*}-\cancel{\left(\frac{H}{L}\right)^2}\frac{\partial}{\partial x_1^*}\left(\frac{2}{3}\mu^*\left(\frac{\partial u_1^*}{\partial x_1^*}+\frac{\partial u_2^*}{\partial x_2^*}+\frac{\partial u_3^*}{\partial x_3^*}\right)\right)$$
$$+\cancel{\left(\frac{H}{L}\right)^2}\frac{\partial}{\partial x_1^*}\left(2\mu^*\frac{\partial u_1^*}{\partial x_1^*}\right)+\cancel{\left(\frac{H}{L}\right)^2}\frac{\partial}{\partial x_2^*}\left(\mu^*\left(\frac{\partial u_2^*}{\partial x_1^*}+\frac{\partial u_1^*}{\partial x_2^*}\right)\right)+\frac{\partial}{\partial x_3^*}\left(\mu^*\left(\frac{\partial u_3^*}{\partial x_1^*}\cancel{\left(\frac{H}{L}\right)^2}+1\frac{\partial u_1^*}{\partial x_3^*}\right)\right), \tag{2.29}$$

x_2^*-direction :

$$\cancel{Re}\,\cancel{\frac{H}{L}}\,\rho^*\left(\frac{\partial u_2^*}{\partial t^*}+u_1^*\frac{\partial u_2^*}{\partial x_1^*}+u_2^*\frac{\partial u_2^*}{\partial x_2^*}+u_3^*\frac{\partial u_2^*}{\partial x_3^*}\right)=\cancel{\frac{Re}{Fr}}\,\cancel{\frac{H}{L}}\,\rho^* k_2^*-EuRe\frac{H}{L}\frac{\partial p_{fl}^*}{\partial x_2^*}-\cancel{\left(\frac{H}{L}\right)^2}\frac{\partial}{\partial x_2^*}\left(\frac{2}{3}\mu^*\left(\frac{\partial u_1^*}{\partial x_1^*}+\frac{\partial u_2^*}{\partial x_2^*}+\frac{\partial u_3^*}{\partial x_3^*}\right)\right)$$
$$+\cancel{\left(\frac{H}{L}\right)^2}\frac{\partial}{\partial x_1^*}\left(\mu^*\left(\frac{\partial u_1^*}{\partial x_2^*}+\frac{\partial u_2^*}{\partial x_1^*}\right)\right)+\cancel{\left(\frac{H}{L}\right)^2}\frac{\partial}{\partial x_2^*}\left(2\mu^*\frac{\partial u_2^*}{\partial x_2^*}\right)+\frac{\partial}{\partial x_3^*}\left(\mu^*\left(\frac{\partial u_3^*}{\partial x_2^*}\cancel{\left(\frac{H}{L}\right)^2}+1\frac{\partial u_2^*}{\partial x_3^*}\right)\right), \tag{2.30}$$

x_3^*-direction :

$$\cancel{Re}\,\cancel{\left(\frac{H}{L}\right)^2}\,\rho^*\left(\frac{\partial u_3^*}{\partial t^*}+u_1^*\frac{\partial u_3^*}{\partial x_1^*}+u_2^*\frac{\partial u_3^*}{\partial x_2^*}+u_3^*\frac{\partial u_3^*}{\partial x_3^*}\right)=\cancel{\frac{Re}{Fr}}\,\cancel{\frac{H}{L}}\,\rho^* k_3^*-EuRe\frac{\partial p_{fl}^*}{\partial x_3^*}-\cancel{\frac{H}{L}}\frac{\partial}{\partial x_3^*}\left(\frac{2}{3}\mu^*\left(\frac{\partial u_1^*}{\partial x_1^*}+\frac{\partial u_2^*}{\partial x_2^*}+\frac{\partial u_3^*}{\partial x_3^*}\right)\right)$$
$$+\frac{\partial}{\partial x_1^*}\left(\mu^*\left(\frac{\partial u_1^*}{\partial x_3^*}\cancel{\frac{H}{L}}+\frac{\partial u_3^*}{\partial x_1^*}\cancel{\left(\frac{H}{L}\right)^3}\right)\right)+\frac{\partial}{\partial x_2^*}\left(\mu^*\left(\frac{\partial u_2^*}{\partial x_3^*}\cancel{\frac{H}{L}}+\frac{\partial u_3^*}{\partial x_2^*}\cancel{\left(\frac{H}{L}\right)^3}\right)\right)+\cancel{\frac{H}{L}}\frac{\partial}{\partial x_3^*}\left(2\mu^*\frac{\partial u_3^*}{\partial x_3^*}\right). \tag{2.31}$$

Parameter	H	L	U	g	μ_0	ρ_0	$\frac{H}{L}$	$Re\frac{H}{L}$	Fr
Value	$1\,\mu m$	$8\,mm$	$1\,m\,s^{-1}$	$9.81\,m\,s^{-2}$	$0.024\,Pa\,s$	$850\,kg\,m^{-3}$	$1.250\cdot10^{-4}$	$4.427\cdot10^{-4}$	12.74

Table 2.1: Characteristic values of the pin-on-disk tribometer.

Expressed again in dimensional form, the remaining terms of the NSE read:

x_1-direction :

$$\frac{\partial p_{fl}}{\partial x_1}=\frac{\partial}{\partial x_3}\left(\mu\frac{\partial u_1}{\partial x_3}\right), \tag{2.32}$$

x_2-direction :

$$\frac{\partial p_{fl}}{\partial x_2}=\frac{\partial}{\partial x_3}\left(\mu\frac{\partial u_2}{\partial x_3}\right), \tag{2.33}$$

x_3-direction :

$$\frac{\partial p_{fl}}{\partial x_3}=0. \tag{2.34}$$

Equation (2.34) allows the deduction that the fluid pressure does not change in x_3-direction. Assuming furthermore that μ is also constant along the x_3-direction, the integration of Equations (2.32) and (2.33) results in analytical expressions for the velocity components u_1 and u_2 and their derivatives [69]:

$$u_1 = \frac{1}{2\mu}\frac{\partial p_{fl}}{\partial x_1}\left(x_3^2 - (z_{low}+z_{up})\,x_3 + z_{low}z_{up}\right) + (U_{up}-U_{low})\left(\frac{x_3}{z_{up}-z_{low}} - \frac{z_{low}}{z_{up}-z_{low}}\right) + U_{low}, \tag{2.35}$$

$$u_2 = \frac{1}{2\mu}\frac{\partial p_{fl}}{\partial x_2}\left(x_3^2 - (z_{low}+z_{up})\,x_3 + z_{low}z_{up}\right), \tag{2.36}$$

$$\frac{\partial u_1}{\partial x_3} = \frac{1}{2\mu}\frac{\partial p_{fl}}{\partial x_1}\left(2x_3 - (z_{low}+z_{up})\right) + \frac{U_{up}-U_{low}}{z_{up}-z_{low}}, \tag{2.37}$$

$$\frac{\partial u_2}{\partial x_3} = \frac{1}{2\mu}\frac{\partial p_{fl}}{\partial x_2}\left(2x_3 - (z_{low}+z_{up})\right), \tag{2.38}$$

where the boundary conditions $u_1(x_3 = z_{low}) = U_{low}$, $u_1(x_3 = z_{up}) = U_{up}$, $u_2(x_3 = z_{low}) = 0$ and $u_2(x_3 = z_{up}) = 0$ are employed. Next, the equation of mass conservation (2.8) is integrated over the gap height [69]:

$$\int_{z_{low}}^{z_{up}} \frac{\partial \rho}{\partial t}\mathrm{d}x_3 + \int_{z_{low}}^{z_{up}} \frac{\partial}{\partial x_1}\left(\rho u_1\right)\mathrm{d}x_3 + \int_{z_{low}}^{z_{up}} \frac{\partial}{\partial x_2}\left(\rho u_2\right)\mathrm{d}x_3 + \int_{z_{low}}^{z_{up}} \frac{\partial}{\partial x_3}\left(\rho u_3\right)\mathrm{d}x_3 = 0. \tag{2.39}$$

In order to reshape this this equation, the Leibniz theorem is used [69]:

$$\frac{\mathrm{d}}{\mathrm{d}t}\int_{z_{low}}^{z_{up}} f(x_1,x_2,x_3,t)\mathrm{d}x_3 = \int_{z_{low}}^{z_{up}} \frac{\partial}{\partial t} f(x_1,x_2,x_3,t)\mathrm{d}x_3 + f(x_1,x_2,z_{up},t)\frac{\mathrm{d}}{\mathrm{d}t}z_{up} - f(x_1,x_2,z_{low},t)\frac{\mathrm{d}}{\mathrm{d}t}z_{low}. \tag{2.40}$$

Assuming additionally that the density stays constant along the x_3-direction and introducing the gap height $h = z_{up} - z_{low}$ allows to express the terms of Equation (2.39) as:

$$\begin{aligned}
\int_{z_{low}}^{z_{up}} \frac{\partial \rho}{\partial t}\mathrm{d}x_3 &= \frac{\partial}{\partial t}\int_{z_{low}}^{z_{up}} \rho \mathrm{d}x_3 - \rho\frac{\partial}{\partial t}z_{up} + \rho\frac{\partial}{\partial t}z_{low} \\
&= \frac{\partial}{\partial t}\left(\rho(z_{up}-z_{low})\right) - \rho\frac{\partial}{\partial t}z_{up} + \rho\frac{\partial}{\partial t}z_{low} \\
&= \frac{\partial}{\partial t}\left(\rho h\right) - \rho\frac{\partial}{\partial t}z_{up} + \rho\frac{\partial}{\partial t}z_{low},
\end{aligned} \tag{2.41}$$

$$\begin{aligned}
\int_{z_{low}}^{z_{up}} \frac{\partial}{\partial x_1}\left(\rho u_1\right)\mathrm{d}x_3 &= \frac{\partial}{\partial x_1}\int_{z_{low}}^{z_{up}} \rho u_1 \mathrm{d}x_3 - \rho U_{up}\frac{\partial}{\partial x_1}z_{up} + \rho U_{low}\frac{\partial}{\partial x_1}z_{low} \\
&= \frac{\partial}{\partial x_1}\left(\rho\int_{z_{low}}^{z_{up}} u_1 \mathrm{d}x_3\right) - \rho U_{up}\frac{\partial}{\partial x_1}z_{up} + \rho U_{low}\frac{\partial}{\partial x_1}z_{low},
\end{aligned} \tag{2.42}$$

$$\int_{z_{low}}^{z_{up}} \frac{\partial}{\partial x_2}(\rho u_2)\,\mathrm{d}x_3 = \frac{\partial}{\partial x_2}\int_{z_{low}}^{z_{up}} \rho u_2 \mathrm{d}x_3$$
$$= \frac{\partial}{\partial x_2}\left(\rho \int_{z_{low}}^{z_{up}} u_2 \mathrm{d}x_3\right), \tag{2.43}$$
$$\int_{z_{low}}^{z_{up}} \frac{\partial}{\partial x_3}(\rho u_3)\,\mathrm{d}x_3 = \rho W_{up} - \rho W_{low}.$$
$$= \rho\left(W_{up} - W_{low}\right). \tag{2.44}$$

Exploiting total derivatives, the velocity components $W_{up} = u_3(x_3 = z_{up})$ and $W_{low} = u_3(x_3 = z_{low})$ reveal to be [69]:

$$W_{up} = \frac{\mathrm{d}}{\mathrm{d}t}z_{up} = \frac{\partial}{\partial t}z_{up} + \left.\frac{\mathrm{d}x_1}{\mathrm{d}t}\right|_{z_{up}} \frac{\partial}{\partial x_1}z_{up} + \left.\frac{\mathrm{d}x_2}{\mathrm{d}t}\right|_{z_{up}} \frac{\partial}{\partial x_2}z_{up} = \frac{\partial}{\partial t}z_{up} + U_{up}\frac{\partial}{\partial x_1}z_{up}, \tag{2.45}$$
$$W_{low} = \frac{\mathrm{d}}{\mathrm{d}t}z_{low} = \frac{\partial}{\partial t}z_{low} + \left.\frac{\mathrm{d}x_1}{\mathrm{d}t}\right|_{z_{low}} \frac{\partial}{\partial x_1}z_{low} + \left.\frac{\mathrm{d}x_2}{\mathrm{d}t}\right|_{z_{low}} \frac{\partial}{\partial x_2}z_{low} = \frac{\partial}{\partial t}z_{low} + U_{low}\frac{\partial}{\partial x_1}z_{low}. \tag{2.46}$$

Inserting the above derived expressions into the equation of mass conservation (2.39) results in [69]:

$$\frac{\partial}{\partial t}(\rho h) + \frac{\partial}{\partial x_1}\left(\rho \int_{z_{low}}^{z_{up}} u_1 \mathrm{d}x_3\right) + \frac{\partial}{\partial x_2}\left(\rho \int_{z_{low}}^{z_{up}} u_2 \mathrm{d}x_3\right) = 0. \tag{2.47}$$

Substituting the analytical expressions (2.35) and (2.36) for u_1 and u_2 to perform the integration finally yields the Reynolds equation [69], [41, Ch. 7.5]:

$$\frac{\partial}{\partial x_1}\left(\frac{\rho h^3}{12\mu}\frac{\partial p_{fl}}{\partial x_1}\right) + \frac{\partial}{\partial x_2}\left(\frac{\rho h^3}{12\mu}\frac{\partial p_{fl}}{\partial x_2}\right) - \frac{\partial}{\partial x_1}(\rho h u_m) - \frac{\partial}{\partial t}(\rho h) = 0, \tag{2.48}$$

where $u_m = (U_{up} + U_{low})/2$ is the mean entrainment velocity. Implicitly contained within the Reynolds equation are the viscous stress components $\tau_{fl,1} = \tau_{31}$ and $\tau_{fl,2} = \tau_{32}$ [69]. Using the stress tensor of a Newtonian fluid provided by Equation (2.23), recalling the negligence of certain viscous terms in the NSE due to $H/L \ll 1$ and substituting the derivatives of u_1 and u_2 according to Equations (2.37) and (2.38) allows to express the viscous stresses of the fluid as:

$$\begin{aligned}
\tau_{fl,1} =& \mu\left(\cancel{\frac{\partial u_3}{\partial x_1}} + \frac{\partial u_1}{\partial x_3}\right)\\
=& \mu\left(\frac{1}{2\mu}\frac{\partial p_{fl}}{\partial x_1}\left(2x_3 - (z_{low} + z_{up})\right) + \frac{U_{up} - U_{low}}{z_{up} - z_{low}}\right)\\
=& \frac{2\overline{x}_3 - h}{2}\frac{\partial p_{fl}}{\partial x_1} + \frac{\mu u_r}{h},
\end{aligned} \tag{2.49}$$
$$\begin{aligned}
\tau_{fl,2} =& \mu\left(\cancel{\frac{\partial u_3}{\partial x_2}} + \frac{\partial u_2}{\partial x_3}\right)\\
=& \mu\left(\frac{1}{2\mu}\frac{\partial p_{fl}}{\partial x_2}\left(2x_3 - (z_{low} + z_{up})\right)\right)\\
=& \frac{2\overline{x}_3 - h}{2}\frac{\partial p_{fl}}{\partial x_2},
\end{aligned} \tag{2.50}$$

where the auxiliary height coordinate $\overline{x}_3 = x_3 - z_{low}$ and relative velocity $u_r = U_{up} - U_{low}$ are used to reshape the equations. Summarized, the necessary assumptions to derive the Reynolds Equation (2.48) are:

- the continuum representation of mass and momentum conservation,
- the material law of an isotropic Newtonian fluid,
- the negligence of most viscous, all inertial and all gravitational terms in the NSE due to an order of magnitude analysis with $H/L \ll 1$, $ReH/L \ll 1$ and $Fr > 1$,
- the boundary conditions of $u_1(x_3 = z_{low}) = U_{low}$, $u_1(x_3 = z_{up}) = U_{up}$, $u_2(x_3 = z_{low}) = 0$ and $u_2(x_3 = z_{up}) = 0$
- and that the dynamic viscosity μ and density ρ are constant along the x_3-direction.

2.7 Cavitation

Cavitation is a commonly occurring phenomenon in lubrication flows and causes parts of the liquid lubricant to transform into its gaseous phase when the fluid pressure p_{fl} reaches the cavitation pressure p_{cav} [17]. In order to consider this in simulations, various cavitation models have been developed. However, some of them do not ensure that the equation of mass conservation is fulfilled to in the cavitation zone. In particular when the flow transitions from a cavitated zone into a full-film region, which can happen for example in certain surface texture configurations, a mass-conserving cavitation model is essential to obtain a correct downstream fluid pressure distribution [7]. This issue can be resolved with the Jakobsson-Floberg-Olsson (JFO) cavitation model [47, 66] which fulfills the equation of mass conservation also within the cavitation zone [17]. It was coupled to the Reynolds equation in the subsequent implementations of Elrod [26], Giacopini *et al.* [34], Bertocchi *et al.* [11], Woloszynski *et al.* [94] and [Hansen et al., 2022]. The employment of the JFO model is elaborated in the following.

In order to ensure that the equation of mass conservation is fulfilled in both the full-film and cavitation region, it is necessary to find an expression of the Reynolds equation which remains valid in both domains. This is achieved by introducing the reduced pressure $p = p_{fl} - p_{cav}$ and the cavity fraction $\theta = 1 - \frac{\rho}{\rho_l}$, where ρ_l denotes the density of the liquid phase while ρ represents the density of the mixture of gaseous and liquid phase. When the lubricant is completely cavitated, ρ is assumed to be zero which causes the cavity fraction to be equal to one. Furthermore, the following constraints mathematically ensure that the cavity fraction is zero in the full-film region, that the reduced pressure is zero in the cavitation zone and that both of them cannot become lower than zero at any point within the lubricant's continuum [11]:

$$p\theta = 0, \quad p \geq 0, \quad \theta \geq 0. \tag{2.51}$$

The next step is to assume that the dynamic viscosity behaves analogously to the density [63] and that the cavitation pressure p_{cav} is a constant. Then, substituting the expressions $p_{fl} = p + p_{cav}$, $\rho = \rho_l (1 - \theta)$ and $\mu = \mu_l (1 - \theta)$ into Equation (2.48) yields the Reynolds equation incorporating mass-conserving cavitation:

$$\frac{\partial}{\partial x_1}\left(\frac{\rho_l h^3}{12\mu_l}\frac{\partial p}{\partial x_1}\right) + \frac{\partial}{\partial x_2}\left(\frac{\rho_l h^3}{12\mu_l}\frac{\partial p}{\partial x_2}\right) - \frac{\partial}{\partial x_1}\left(\rho_l h u_m (1-\theta)\right) - \frac{\partial}{\partial t}\left(\rho_l h (1-\theta)\right) = 0, \tag{2.52}$$

where μ_l denotes the dynamic viscosity of the liquid phase while μ represents the dynamic viscosity of the mixture of gaseous and liquid phase. Applying the same approach to Equations (2.49) and (2.50) results in the viscous stresses of the fluid incorporating mass-conserving cavitation:

$$\tau_{fl,1} = \frac{2\overline{x}_3 - h}{2} \frac{\partial p}{\partial x_1} + \frac{\mu_l u_r}{h} (1 - \theta), \tag{2.53}$$

$$\tau_{fl,2} = \frac{2\overline{x}_3 - h}{2} \frac{\partial p}{\partial x_2}. \tag{2.54}$$

2.8 Piezoviscosity and Compressibility of the Liquid Phase

In case of high pressures being generated within the lubrication gap, piezoviscosity and compressibility can noticeably affect the fluid pressure and vice versa. Depending on whether piezoviscosity is completely neglected or considered with either the Barus or the Roelands model, the dynamic viscosity of the liquid phase reads [89, Ch. 1.3.3], [63]:

$$\mu_l = \begin{cases} \mu_0 \\ \mu_0 \exp\left(\alpha_B \left(p_{fl} - p_{cav}\right)\right) \\ \mu_0 \exp\left(\left(\ln\left(\mu_0\right) + 9.67\right) \cdot \left(-1 + \left(1 + \frac{(p_{fl} - p_{cav})}{p_{0,R}}\right)^{z_R}\right)\right), \end{cases} \tag{2.55}$$

where the pressure viscosity index is provided by $z_R = \frac{\alpha_R p_{0,R}}{\ln(\mu_0 + 9.67)}$ [64], α_B or α_R represent the pressure viscosity coefficient respectively of the Barus or Rolands model, $p_{0,R}$ denotes a constant in the Roelands equation and μ_0 is the dynamic viscosity of the lubricant's liquid phase at ambient pressure. Similarly, depending on whether compressibility is neglected or incorporated through the Dowson-Higginson model, the density of the liquid phase is provided by [89, Ch. 1.3.4], [11, 63]:

$$\rho_l = \begin{cases} \rho_0 \\ \rho_0 \frac{C_1 + C_2 (p_{fl} - p_{cav})}{C_1 + (p_{fl} - p_{cav})}, \end{cases} \tag{2.56}$$

where C_1 and C_2 are lubricant dependent constants of the Dowson-Higginson model and ρ_l describes the density of the lubricant's liquid phase at ambient pressure.

2.9 Roughness

Especially for lubrication gaps that operate under mixed lubrication, roughness effects influence the friction behaviour of the tribological contact due to two reasons: first, the fluid pressure generation can be enhanced or weakened depending on the shape and orientation of the roughness profile when the gap height is of a similar magnitude as the height of the roughness asperities. This can be modelled by roughness influence factors in the Reynolds equation. Second, surface contact is determined on the roughness scale when the roughness asperities of both surfaces get into contact with each other. This means that the contact pressure p_{con} can also be expressed as a roughness dependent quantity. Within the next subsections, it is first described how the roughness effects are incorporated into the Reynolds equation. In the following subsection, it is elaborated how the contact pressure depends on the roughness.

2.9.1 Homogenization of the Reynolds Equation

The most popular method to incorporate roughness effects into the Reynolds equation is the flow factor method developed by Patir and Cheng [67, 68]. However, this method has shortcomings when non-symmetrical or oblique roughnesses are employed because it cannot model any sideways deflection of the flow. In contrast, the homogenization theory [5] can take this effect into account and therefore represents a more versatile approach [3]. Since its applicability has been demonstrated on several occasions in the literature [56, 4, 74], it is also employed in the following. Staying consistent with Equation (2.5), the idea is first to split the gap height into a macroscopic gap height h_0 and its microscopic variation h_1:

$$h = h_0(X_1, X_2, T) + h_1(\xi_1, \xi_2, \kappa) \tag{2.57}$$

At the same time, the coordinates x_1, x_2, t are split into macroscopic coordinates X_1, X_2, T and microscopic coordinates ξ_1, ξ_2, κ. It is assumed that h_1 is periodic, where λ_{ξ_1} and λ_{ξ_2} describe the length and width of the periodic domain and λ_κ represents the corresponding periodic time span. Additionally, it is assumed that λ_{ξ_1} is significantly smaller than the characteristic length on the macro-scale L, thus resulting in a magnitude ratio of $\epsilon = \lambda_{\xi_1}/L \ll 1$. Employing this magnitude ratio, the decomposed coordinates can be expressed through the original coordinates:

$$\vec{X} = \begin{pmatrix} X_1 \\ X_2 \end{pmatrix} = \begin{pmatrix} x_1 \\ x_2 \end{pmatrix} = \vec{x}, \tag{2.58}$$

$$T = t, \tag{2.59}$$

$$\vec{\xi} = \begin{pmatrix} \xi_1 \\ \xi_2 \end{pmatrix} = \begin{pmatrix} \frac{x_1}{\epsilon} \\ \frac{x_2}{\epsilon} \end{pmatrix} = \frac{\vec{x}}{\epsilon}, \tag{2.60}$$

$$\kappa = \frac{t}{\epsilon}. \tag{2.61}$$

This allows to determine their partial derivatives as:

$$\frac{\partial X_1}{\partial x_1} = 1; \quad \frac{\partial X_2}{\partial x_2} = 1; \quad \frac{\partial T}{\partial t} = 1; \tag{2.62}$$

$$\frac{\partial \xi_1}{\partial x_1} = \frac{1}{\epsilon}; \quad \frac{\partial \xi_2}{\partial x_2} = \frac{1}{\epsilon}; \quad \frac{\partial \kappa}{\partial t} = \frac{1}{\epsilon}, \tag{2.63}$$

which can be substituted into the partial derivatives with respect to the original coordinates:

$$\nabla_{\vec{x}} = \begin{pmatrix} \frac{\partial}{\partial x_1} \\ \frac{\partial}{\partial x_2} \end{pmatrix} = \begin{pmatrix} \frac{\partial}{\partial X_1}\frac{\partial X_1}{\partial x_1} \\ \frac{\partial}{\partial X_2}\frac{\partial X_2}{\partial x_2} \end{pmatrix} + \begin{pmatrix} \frac{\partial}{\partial \xi_1}\frac{\partial \xi_1}{\partial x_1} \\ \frac{\partial}{\partial \xi_2}\frac{\partial \xi_2}{\partial x_2} \end{pmatrix} = \nabla_{\vec{X}} + \frac{\nabla_{\vec{\xi}}}{\epsilon}, \tag{2.64}$$

$$\frac{\partial}{\partial t} = \frac{\partial}{\partial T} + \frac{1}{\epsilon}\frac{\partial}{\partial \kappa}. \tag{2.65}$$

Contrary to the gap height, the density and dynamic viscosity of the liquid phase and cavity fraction are assumed to be functions of the macroscopic coordinates only:

$$\rho_l(\vec{x}, t) \approx \rho_l(\vec{X}, T), \tag{2.66}$$

$$\mu_l(\vec{x}, t) \approx \mu_l(\vec{X}, T), \tag{2.67}$$

$$\theta(\vec{x}, t) \approx \theta(\vec{X}, T), \tag{2.68}$$

while the following expression is suggested for the decomposition of the reduced pressure :

$$p = p_0(\vec{X}, T) + \epsilon p_1(\vec{\xi}, \kappa). \tag{2.69}$$

Next, the above provided expressions are substituted into the Reynolds Equation (2.51):

$$\begin{aligned} &\left(\nabla_{\vec{X}} + \frac{\nabla_{\vec{\xi}}}{\epsilon}\right) \cdot \left(\frac{\rho_l h^3}{12\mu_l}\left(\nabla_{\vec{X}} + \frac{\nabla_{\vec{\xi}}}{\epsilon}\right)\left(p_0(\vec{X}, T) + \epsilon p_1(\vec{\xi}, \kappa)\right)\right) \\ &- \left(\nabla_{\vec{X}} + \frac{\nabla_{\vec{\xi}}}{\epsilon}\right) \cdot \left(h\rho_l \begin{pmatrix} u_m \\ 0 \end{pmatrix}(1-\theta)\right) - \left(\frac{\partial}{\partial T} + \frac{1}{\epsilon}\frac{\partial}{\partial \tau}\right)(\rho_l h(1-\theta)) = 0. \end{aligned} \tag{2.70}$$

This equation can be sorted into terms with the coefficients of ϵ^{-2}, ϵ^{-1}, ϵ^0 and ϵ^1. It is fulfilled, if all of the four terms are required to be equal to zero, thus creating four new equations:

$$\epsilon^{-2}: \qquad 0 \stackrel{!}{=} \nabla_{\vec{\xi}} \cdot \left(\frac{\rho_l h^3}{12\mu_l} \underbrace{\nabla_{\vec{\xi}} p_0(\vec{X}, T)}_{=0}\right), \tag{2.71}$$

$$\begin{aligned} \epsilon^{-1}: \qquad 0 \stackrel{!}{=} &\nabla_{\vec{X}} \cdot \left(\frac{\rho_l h^3}{12\mu_l} \underbrace{\nabla_{\vec{\xi}} p_0(\vec{X}, T)}_{=0}\right) + \nabla_{\vec{\xi}} \cdot \left(\frac{\rho_l h^3}{12\mu_l}\left(\nabla_{\vec{X}} p_0(\vec{X}, T) + \nabla_{\vec{\xi}} p_1(\vec{\xi}, \kappa)\right)\right) \\ &- \nabla_{\vec{\xi}} \cdot \left(h\rho_l \begin{pmatrix} u_m \\ 0 \end{pmatrix}(1-\theta)\right) - \frac{\partial}{\partial \kappa}\left(\rho_l h(1-\theta(\vec{X}, T))\right), \end{aligned} \tag{2.72}$$

$$\epsilon^0: \quad 0 \stackrel{!}{=} \nabla_{\vec{X}} \cdot \left(\frac{\rho_l h^3}{12\mu_l} \left(\nabla_{\vec{X}} p_0(\vec{X}, T) + \nabla_{\vec{\xi}} p_1(\vec{\xi}, \kappa) \right) \right) + \nabla_{\vec{\xi}} \cdot \left(\frac{\rho_l h^3}{12\mu_l} \underbrace{\nabla_{\vec{X}} p_1(\vec{\xi}, \kappa)}_{=0} \right), - \nabla_{\vec{X}} \cdot \left(h\rho_l \begin{pmatrix} u_m \\ 0 \end{pmatrix} \left(1 - \theta(\vec{X}, T) \right) \right) - \frac{\partial}{\partial T} \left(h\rho_l \left(1 - \theta(\vec{X}, T) \right) \right), \tag{2.73}$$

$$\epsilon^1: \quad 0 \stackrel{!}{=} \nabla_{\vec{X}} \cdot \left(\frac{\rho_l h^3}{12\mu_l} \underbrace{\nabla_{\vec{X}} p_1(\vec{\xi}, \kappa)}_{=0} \right). \tag{2.74}$$

Taking into account that some of the partial derivatives are directly equal to zero because p_0 is only a function of the macroscopic and p_1 is only a function of the microscopic coordinates, causes Equations (2.71) and (2.74) to be fulfilled by default. Keeping additionally in mind that the density and dynamic viscosity of the liquid phase and the cavity fraction are also assumed to depend only upon the macroscopic coordinates allows to express Equation (2.72) as:

$$\nabla_{\vec{\xi}} \left(\frac{\rho_l h^3}{12\mu_l} \nabla_{\vec{\xi}} p_1 \right) = \rho_l u_m \frac{\partial h}{\partial \xi_1} (1 - \theta) + \rho_l \frac{\partial h}{\partial \kappa} (1 - \theta) - \frac{\rho_l}{12\mu_l} \left(\frac{\partial h^3}{\partial \xi_1} \frac{\partial p_0}{\partial X_1} + \frac{\partial h^3}{\partial \xi_2} \frac{\partial p_0}{\partial X_2}. \right) \tag{2.75}$$

This equation can be fulfilled if p_1 is of the following form:

$$p_1(\vec{\xi}, \kappa) = 12\mu_l u_m (1 - \theta) \chi_1(\vec{\xi}, \kappa) + \frac{\partial p_0}{\partial X_1} \chi_2(\vec{\xi}, \kappa) + \frac{\partial p_0}{\partial X_2} \chi_3(\vec{\xi}, \kappa). \tag{2.76}$$

Substituting this expression into Equation (2.75) and comparing terms with the same macroscopic coefficients yields the set of local problems whose solutions are denoted by χ_1, χ_2 and χ_3:

$$\rho_l(1 - \theta): \quad \nabla_{\vec{\xi}} \cdot \left(h^3 \nabla_{\vec{\xi}} \chi_1 \right) = \frac{\partial h}{\partial \xi_1} + \frac{1}{u_m} \frac{\partial h}{\partial \kappa}, \tag{2.77}$$

$$\frac{\rho_l}{12\mu_l} \frac{\partial p_0}{\partial X_1}: \quad \nabla_{\vec{\xi}} \cdot \left(h^3 \nabla_{\vec{\xi}} \chi_2 \right) = -\frac{\partial h^3}{\partial \xi_1}, \tag{2.78}$$

$$\frac{\rho_l}{12\mu_l} \frac{\partial p_0}{\partial X_2}: \quad \nabla_{\vec{\xi}} \cdot \left(h^3 \nabla_{\vec{\xi}} \chi_3 \right) = -\frac{\partial h^3}{\partial \xi_2}. \tag{2.79}$$

Next, Equation (2.76) is substituted into Equation (2.73) which is afterwards averaged over the periodic length λ_{ξ_1}, width λ_{ξ_2} and time span λ_κ:

$$0 = \frac{1}{\lambda_{\xi_1} \lambda_{\xi_2} \lambda_\kappa} \int_{\lambda_{\xi_1}} \int_{\lambda_{\xi_2}} \int_{\lambda_\kappa} \nabla_{\vec{X}} \cdot \left(\frac{\rho_l h^3}{12\mu_l} \left(\nabla_{\vec{X}} p_0 + \nabla_{\vec{\xi}} \left(12\mu_l u_m (1 - \theta) \chi_1 + \frac{\partial p_0}{\partial X_1} \chi_2 \right) + \frac{\partial p_0}{\partial X_2} \chi_3 \right) \right) - h\rho_l \begin{pmatrix} u_m \\ 0 \end{pmatrix} (1 - \theta) - \frac{\partial}{\partial T} \left(h\rho_l (1 - \theta) \right) \, \mathrm{d}\kappa \, \mathrm{d}\xi_2 \, \mathrm{d}\xi_1 \tag{2.80}$$

Introducing the mean gap height:

$$\overline{h}(h_0) = \frac{1}{\lambda_{\xi_1} \lambda_{\xi_2} \lambda_\kappa} \int_{\lambda_{\xi_1}} \int_{\lambda_{\xi_2}} \int_{\lambda_\kappa} h \, \mathrm{d}\kappa \, \mathrm{d}\xi_2 \, \mathrm{d}\xi_1 \tag{2.81}$$

into Equation (2.80) finally yields the homogenized Reynolds equation:

$$
\begin{aligned}
0 = \nabla_{\vec{X}} \cdot & \left(\frac{\rho_l \overline{h}^3}{12 \mu_l} \underbrace{\frac{1}{\lambda_{\xi_1} \lambda_{\xi_2} \lambda_\kappa} \int_{\lambda_{\xi_1}} \int_{\lambda_{\xi_2}} \int_{\lambda_\kappa} \frac{h^3}{\overline{h}^3} \begin{pmatrix} 1 + \frac{\partial \chi_2}{\partial \xi_1} & \frac{\partial \chi_3}{\partial \xi_1} \\ \frac{\partial \chi_2}{\partial \xi_2} & 1 + \frac{\partial \chi_3}{\partial \xi_2} \end{pmatrix} \mathrm{d}\kappa \, \mathrm{d}\xi_2 \, \mathrm{d}\xi_1}_{A(h_0)} \nabla_{\vec{X}} p_0 \right) \\
- \nabla_{\vec{X}} \cdot & \left(\rho_l \overline{h} u_m \underbrace{\frac{1}{\lambda_{\xi_1} \lambda_{\xi_2} \lambda_\kappa} \int_{\lambda_{\xi_1}} \int_{\lambda_{\xi_2}} \int_{\lambda_\kappa} \frac{h}{\overline{h}} \begin{pmatrix} 1 - h^2 \frac{\partial \chi_1}{\partial \xi_1} \\ -h^2 \frac{\partial \chi_1}{\partial \xi_2} \end{pmatrix} \mathrm{d}\kappa \, \mathrm{d}\xi_2 \, \mathrm{d}\xi_1}_{\vec{b}(h_0)} (1 - \theta) \right) \\
- \frac{\partial}{\partial T} & \left(\rho_l \overline{h} \underbrace{\frac{1}{\lambda_{\xi_1} \lambda_{\xi_2} \lambda_\kappa} \int_{\lambda_{\xi_1}} \int_{\lambda_{\xi_2}} \int_{\lambda_\kappa} \frac{h}{\overline{h}} \, \mathrm{d}\kappa \, \mathrm{d}\xi_2 \, \mathrm{d}\xi_1}_{=1} (1 - \theta) \right),
\end{aligned}
\tag{2.82}
$$

where A and $\vec{b}$ are tensors containing the homogenization factors of the Reynolds equation. For the sake of simplicity, it is assumed that the cavitation constraints only depend upon macroscopic quantities, thus yielding:

$$
p_0 \theta = 0, \quad p_0 \geq 0, \quad \theta \geq 0. \tag{2.83}
$$

In order to obtain the homogenized viscous stresses of the fluid, Equations (2.69) and (2.76) are substituted into Equations (2.53) and (2.54) and averaged over $\lambda_{\xi_1} \lambda_{\xi_2} \lambda_\kappa$:

$$
\begin{aligned}
\begin{pmatrix} \overline{\tau}_{fl,1} \\ \overline{\tau}_{fl,2} \end{pmatrix} = & \frac{\overline{h}(2r_\tau - 1)}{2} \underbrace{\frac{1}{\lambda_{\xi_1} \lambda_{\xi_2} \lambda_\kappa} \int_{\lambda_{\xi_1}} \int_{\lambda_{\xi_2}} \int_{\lambda_\kappa} \frac{h}{\overline{h}} \begin{pmatrix} 1 + \frac{\partial \chi_2}{\partial \xi_1} & \frac{\partial \chi_3}{\partial \xi_1} \\ \frac{\partial \chi_2}{\partial \xi_2} & 1 + \frac{\partial \chi_3}{\partial \xi_2} \end{pmatrix} \mathrm{d}\kappa \, \mathrm{d}\xi_2 \, \mathrm{d}\xi_1}_{C(h_0)} \nabla_{\vec{X}} p_0 \\
& + \frac{6 \mu_l u_m}{\overline{h}} (2r_\tau - 1) \underbrace{\frac{1}{\lambda_{\xi_1} \lambda_{\xi_2} \lambda_\kappa} \int_{\lambda_{\xi_1}} \int_{\lambda_{\xi_2}} \int_{\lambda_\kappa} \overline{h} h \begin{pmatrix} \frac{\partial \chi_1}{\partial \xi_1} \\ \frac{\partial \chi_1}{\partial \xi_2} \end{pmatrix} \mathrm{d}\kappa \, \mathrm{d}\xi_2 \, \mathrm{d}\xi_1}_{\vec{d}(h_0)} (1 - \theta) \\
& + \frac{\mu_l (1 - \theta) u_r}{\overline{h}} \begin{pmatrix} 1 \\ 0 \end{pmatrix} \underbrace{\frac{1}{\lambda_{\xi_1} \lambda_{\xi_2} \lambda_\kappa} \int_{\lambda_{\xi_1}} \int_{\lambda_{\xi_2}} \int_{\lambda_\kappa} \frac{\overline{h}}{h} \, \mathrm{d}\kappa \, \mathrm{d}\xi_2 \, \mathrm{d}\xi_1}_{=1},
\end{aligned}
\tag{2.84}
$$

where $\overline{x}_3 = r_\tau h$ was used to provide the viscous stresses at an arbitrary fraction r_τ of the gap height h and the tensors C and $\vec{d}$ contain the homogenization factors of the viscous stresses.

2.9.2 Surface Contact

As described in the previous subsection, the homogenization factors depend upon the solutions χ_1, χ_2 and χ_3 of the local problems, which can be computed numerically for a gap height distribution h that consists of a microscopic variation h_1 of any macroscopic gap height h_0. For a decreasing h_0, this will at some point lead to the roughness asperities of both surfaces touching each other and being deformed due to the occurring asperity contact pressure. This can be modelled by splitting h_1 into its known rigid $h_{1,ri}$ and unknown elastic $h_{1,el}$ contributions on the micro-scale:

$$h = h_0 + h_1 = h_0 + h_{1,ri} + h_{1,el}, \tag{2.85}$$

where the elastic deformation can be connected to the $N_{\xi_1,R}N_{\xi_2,R}$ discrete asperity contact pressures p_{asp} with the elastic-half space theory provided earlier in Section 2.5:

$$h_{1,el}(\xi_1,\xi_2,\kappa) = \sum^{N_{\xi_1,R}} \sum^{N_{\xi_2,R}} \frac{2}{\pi E'} K(\xi_1 - \xi_{1,R}, \xi_2 - \xi_{2,R}) p_{asp}(\xi_{1,R}, \xi_{2,R}, \kappa). \tag{2.86}$$

At last, this closes the system of equations on the microscopic scale. For a known rigid microscopic variation $h_{1,ri}$ of any imposed macroscopic gap height h_0, the equilibrium of $h_{1,el}$ and p_{asp} can be computed with Equation (2.86), when $p_{asp} = 0$ is required to hold in non-contact regions of $h > 0$ while $p_{asp} \geq 0$ is allowed in contact regions of $h = 0$. Negative gap heights $h < 0$ are only allowed in regions where the upper limit Hrd due to the hardness of the softer surface is reached for p_{asp}. At these points, $p_{asp} = Hrd$ is enforced and h is subsequently truncated at zero, where the truncated amount of h can be interpreted as a plastic deformation.

Before the solutions χ_1, χ_2 and χ_3 of the local problems are computed, h again needs to be truncated at a lower threshold of $h > 0$ such that the system of equations does not become singular. Analogously to the homogenization factors, the mean contact pressure on the macroscopic scale can lastly be determined by averaging over $\lambda_{\xi_1}\lambda_{\xi_2}\lambda_\kappa$:

$$\overline{p}_{con}(h_0) = \frac{1}{\lambda_{\xi_1}\lambda_{\xi_2}\lambda_\kappa} \int_{\lambda_{\xi_1}} \int_{\lambda_{\xi_2}} \int_{\lambda_\kappa} p_{asp} \,\mathrm{d}\kappa \,\mathrm{d}\xi_2 \,\mathrm{d}\xi_1. \tag{2.87}$$

2.9.3 Coupling to the Macroscopic Scale

Finally, the macroscopic coordinates can be assigned by decomposing h_0:

$$h_0(X_1, X_2, T) = h_{0,d} + h_{0,ri}(X_1, X_2, T) + h_{0,el}(p_{tot}(X_1, X_2, T)), \tag{2.88}$$

where $h_{0,d}$ represents the rigid body displacement on the macro-scale, $h_{0,ri}$ denotes the rigid macroscopic gap height variation while the corresponding macroscopic elastic gap height deformation $h_{0,el}$ reads:

$$h_{0,el}(X_1, X_2, T) = \sum^{N_{X_1,R}} \sum^{N_{X_2,R}} \frac{2}{\pi E'} K(X_1 - X_{1,R}, X_2 - X_{2,R}) p_{tot}(X_{1,R}, X_{2,R}, T). \tag{2.89}$$

The total pressure is finally provided by:

$$p_{tot} = p_{0,fl} + \overline{p}_{con} = p_0 + p_{cav} + \overline{p}_{con}. \tag{2.90}$$

Lastly, the product of mean contact pressure $\overline{p}_{con}$ and boundary friction coefficient $C_{f,b}$ is used to determine the mean tangential contact stress in x_1-direction:

$$\overline{\tau}_{con,1} = \text{sign}(u_r) C_{f,b} \overline{p}_{con}. \tag{2.91}$$

Superimposing it with the homogenized viscous stress in x_1-direction yields the total tangential stress at the lower surface:

$$\tau_{tot} = \overline{\tau}_{fl,1}\big|_{r_\tau=0} + \overline{\tau}_{con,1}. \tag{2.92}$$

3 Numerical Solvers

This chapter provides an overview of the two solvers that were subsequently developed to simulate the conditions within a generic lubrication gap by solving the equations provided in the previous chapter. The first solver is able to determine the equilibrium of fluid pressure build-up, elastic deformation and cavitation through the elasto-hydrodynamic lubrication Fischer-Burmeister-Newton-Schur (EHL-FBNS) algorithm which was published in the article *An EHL Extension of the Unsteady FBNS Algorithm* by [Hansen et al., 2022]. While this single-scale solver is only applicable in the full-film region, its extension into the homogenized mixed elasto-hydrodynamic lubrication Fischer-Burmeister-Newton-Schur (HMEHL-FBNS) algorithm is capable to model the whole Stribeck curve by also taking the roughness scale and surface contact into account. This subsequent work was published in the article *Establishment and Calibration of a Digital Twin to Replicate the Friction Behaviour of a Pin-on-Disk Tribometer* by [Hansen et al., 2023].

3.1 EHL-FBNS Solver

"In the case of lubrication flows in narrow gaps, the Reynolds equation [72] is a handy tool to determine the hydrodynamic pressure distribution in a simpler way than by using the full Navier-Stokes equations [41, Ch. 7]. Since cavitation commonly occurs in lubrication flows, various models have been developed to describe this phenomenon [17]. Especially when it occurs within surface textures, mass-conserving properties of the cavitation model are required to properly describe the flow's transition from the cavitation region to the full-film region, because this full-film reformulation interface has a great effect on the extension of the cavitated area and the subsequent downstream rise in pressure within the full-film region [7]. The required mass-conserving properties can be taken into account with the Jakobsson-Floberg-Olsson (JFO) [47, 66] cavitation model [17]. Starting from the cavitation algorithm of Elrod [26], Giacopini *et al.* [34] developed a one-dimensional finite element method (FEM) solver that couples the Reynolds equation with the mass-conserving JFO cavitation model through a complementarity formulation. This work was extended by Bertocchi *et al.* [11] to consider two-dimensional problems with compressible, piezoviscous and shear-thinning fluid behaviour. The arising complementarity problem was reformulated to be expressed by an unconstrained system of equations by Woloszynski *et al.* [94], resulting in the Fischer-Burmeister-Newton-Schur (FBNS) algorithm. As demonstrated by Woloszynski *et al.*, the FBNS algorithm is of remarkable computational efficiency also for high spatial resolutions.

In many cases, the fluid pressure can deform the lubricated surfaces notably, leading to the regime of elasto-hydrodynamic lubrication (EHL) [60]. Various solvers have been developed to tackle EHL problems, some of the most prominent ones are the finite difference method (FDM) multigrid solver of Venner and Lubrecht [89] and the FEM solver of Habchi [39]. Some algorithms are also capable of simulating surface contact along with the Reynolds equation [98, 92, 97, 96, 48]. Since the full-film reformulation interface is often not of relevance in EHL problems, many EHL solvers do not employ mass-conserving cavitation models. However, in some cases - such as starved lubrication - mass-conserving cavitation is crucial and has been considered in several works [18, 58]. Among them, the coupling of pressure, mass-conserving cavitation, elastic deformation, a roughness asperity contact model and the FBNS algorithm was achieved by Ferretti [30, 31]. In contrast to Ferretti's work, the FBNS algorithm is coupled

with the elastic deformation of an elastic half-space within this [...manuscript], thus presenting the new EHL-FBNS algorithm. Due to the half-space assumption, the elastic deformation is a linear convolution of a kernel function with the fluid pressure field. This allows exploiting the fast Fourier transform (FFT) to speed up the computation of the elastic deformation [91]. Furthermore, a proportional integral derivative (PID) controller is employed to meet the load balance equation through adjustment of the rigid body displacement as already introduced by Wang *et al.* [93]. Eventually, the EHL-FBNS algorithm is capable of efficiently computing the solution of large problems that require the consideration of both mass-conserving cavitation and elastic deformation at the same time" [Hansen et al., 2022].

3.1.1 Governing Equations

In dimensionless form, the Reynolds equation (2.52) incorporating mass-conserving cavitation reads [Hansen et al., 2022]:

$$G = \underbrace{\frac{\partial}{\partial x_1^*}\left(\xi_{Po}^* \frac{\partial p^*}{\partial x_1^*}\right) + \left(\frac{x_{1,ref}}{x_{2,ref}}\right)^2 \frac{\partial}{\partial x_2^*}\left(\xi_{Po}^* \frac{\partial p^*}{\partial x_2^*}\right)}_{\text{Poiseuille term}} \underbrace{- \frac{\partial}{\partial x_1^*}\left(\xi_{Co}^* (1-\theta)\right)}_{\text{Couette term}} \underbrace{- \frac{\partial}{\partial t^*}\left(\xi_{Ti}^* (1-\theta)\right)}_{\text{Unsteady term}}. \tag{3.1}$$

"It can be derived by inserting the following non-dimensional quantities (indicated by *) and reference quantities (denoted by the index $_{ref}$) into and reformulating Equation (2.52):

$$\begin{aligned} x_1 = x_1^* x_{1,ref}, \quad x_2 = x_2^* x_{2,ref}, \quad t = t^* t_{ref}, \quad \rho_l = \rho^* \rho_{ref}, \\ \mu_l = \mu^* \mu_{ref}, \quad h = h^* h_{ref}, \quad u_m = u_m^* u_{m,ref}, \quad p = p^* p_{ref}. \end{aligned} \tag{3.2}$$

Similar to Venner and Lubrecht [89, Ch. 6.3], the coefficients of the Poiseuille, Couette and unsteady term within the dimensionless Reynolds equation can be consolidated as" [Hansen et al., 2022]:

$$\xi_{Po}^* = \frac{\rho^* h^{*3}}{\mu^*}, \quad \xi_{Co}^* = 12 \frac{x_{1,ref} u_{m,ref} \mu_{ref}}{h_{ref}^2 p_{ref}} \rho^* h^* u_m^*, \quad \xi_{Ti}^* = 12 \frac{x_{1,ref}^2 \mu_{ref}}{t_{ref} h_{ref}^2 p_{ref}} \rho^* h^*. \tag{3.3}$$

Furthermore, the cavitation constraints read in dimensionless form:

$$p^* \theta = 0, \quad p^* \geq 0, \quad \theta \geq 0. \tag{3.4}$$

The solver is implemented such that simulations can be performed either with constant or fluid pressure dependent dynamic viscosity and density as described by Equations (2.55) and (2.56). Further variety is incorporated in the dimensionless gap height equation:

$$h^* = h_d^* + h_{ri}^* + h_{el}^*. \tag{3.5}$$

If completely rigid geometries are assumed, the dimensionless elastic gap height deformation h_{el}^* is set to zero. Otherwise, it is computed as a function of the fluid pressure p_{fl} according to Equations (2.19) and (3.2). Lastly, the dimensionless rigid body displacement h_d^* is either set to a constant imposed value or - if an imposed normal load is prescribed - it is determined by the solver such that the load balance equation (2.3) is fulfilled by p_{fl}.

3.1.2 Algorithm

"The set of equations described above can be solved numerically with the EHL-FBNS algorithm presented in the following. This new algorithm is based on the FBNS algorithm developed by Woloszynski *et al.* [94] and extends it by taking elastic surface deformation and the load balance equation into account [...]. [After putting the Reynolds equation into dimensionless form,] the complimentary constraints (3.4) are replaced by the Fischer-Burmeister equation in non-dimensional form [94]:

$$F = p^* + \theta - \sqrt{p^{*2} + \theta^2}. \tag{3.6}$$

The EHL-FBNS algorithm uses the Newton-Raphson method to determine the values of p^* and θ such that G and F get sufficiently close to 0, thus solving the dimensionless Reynolds Equation (3.1) and the dimensionless Fischer-Burmeister Equation (3.6). By evaluating the discretized form of G and F at each discrete position, a system of equations is created. The discretized equations are obtained though the finite volume method (FVM), where the second order midpoint rule is applied to evaluate surface and volume integrals. The required values and derivatives of the Poiseuille term are discretized with a second order central scheme, the ones of the Couette term by either the first order upwind interpolation (UI) or the third order quadratic upwind interpolation (QUICK) and the unsteady term with the first order Euler implicit scheme [32, Ch. 3.3, 4, 6.3.2]. The discretized expressions of Equations (3.1) and (3.6) are provided in [the] appendix [of the publication by [Hansen et al., 2022]]. The set of discrete dimensionless Reynolds equations $\vec{G}$ can be expressed in matrix-vector notation through the pressure coefficients contributed by the Poiseuille term A_{Po}, the discretized dimensionless reduced pressures $\vec{p^*}$, the cavity fraction coefficients contributed by the Couette and unsteady term B, the discretized cavity fractions $\vec{\theta}$ and the remaining constants from the Couette and unsteady term $\vec{c}$ [94]:

$$\vec{G} = A_{Po}\vec{p^*} + B\vec{\theta} + \vec{c}. \tag{3.7}$$

The set of discrete dimensionless Fischer-Burmeister Equations (3.6) is denoted by $\vec{F}(\vec{p^*}, \vec{\theta})$. The non-dimensional properties μ^* and ρ^* at each discrete point are computed according to the respective Equations (2.55), (2.56) and (3.2).

The gap height h at each discrete point is computed according to Equation (2.5). It is prevented from becoming lower than $1\,\mathrm{nm}$ by using truncation at this instant. Afterwards, the non-dimensional gap height h^* [of Equation (3.5)] is determined through Equation (3.2). If the surfaces are chosen to be elastic, Equation (2.19) is discretized by assuming a constant pressure over the rectangular discretization cell [49, Ch. 3.3], [8, Ch. 3.1], the discretized equation is also provided in [the] appendix [of the publication by [Hansen et al., 2022]]. Since the resulting equation is a linear convolution of a kernel function with the fluid pressure field, it is computed in Fourier space by means of a FFT to speed up the computation. Attention is paid to double the size of the kernel in each direction and to zero pad the fluid pressure field such that a linear instead of a circular convolution is obtained. After the convolution, the deformation and pressure fields are resized to their original size [75, 91, Hansen et al., 2020].

After computing $\vec{G}$ and $\vec{F}$, the Newton-Raphson method is used to determine the updates of non-dimensional reduced pressure $\vec{\delta}_{p^*}$ and cavity fraction $\vec{\delta}_\theta$ [94]:

$$J\vec{\delta} = \begin{bmatrix} J_{F,p^*} & J_{F,\theta} \\ J_{G,p^*} & J_{G,\theta} \end{bmatrix} \begin{bmatrix} \vec{\delta}_{p^*} \\ \vec{\delta}_\theta \end{bmatrix} = - \begin{bmatrix} \vec{F} \\ \vec{G} \end{bmatrix} \tag{3.8}$$

The most important extension of the EHL-FBNS algorithm compared to the original FBNS algorithm is the approximation of the pressure Jacobian J_{G,p^*} of the dimensionless Reynolds equation when elastic deformation is taken into account. The idea is to consider the dependence $h^*(p^*)$ by inserting it into $\vec{c}$, thus creating the matrix A_h. Due to the kernel function, this would result in A_h being a full matrix which is prone to lose its diagonal dominance and therefore being unfeasible to invert and likely to cause unstable behaviour in the iteration process. This is rectified by approximating A_h only by some of its diagonals as already done in the literature for other EHL algorithms: for example Venner and Lubrecht [89, Ch. C.1,C.3.2] who combine it with distributive relaxation and multigrid methods or Wang *et al.* [92] who employ the semi-system method. In case of the EHL-FBNS algorithm, A_h is reduced to the 5 diagonals that correspond to the South, West, Center, East and North cells. Eventually, the Jacobians of $\vec{G}$ read $J_{G,p^*} = A_{Po} + A_h$ and $J_{G,\theta} = B$. The boundary conditions of $\vec{p^*}$ are considered in A_{Po} and $\vec{c}$ and the boundary conditions of $\vec{\theta}$ in $\vec{F}$ and $J_{F,\theta}$. If Neumann boundary conditions are used for $\vec{\theta}$, the Jacobian $J_{F,\theta}$ would contain several diagonals. In this case, it is approximated only by its main diagonal. It is worthwhile to note that this approximation of the Jacobians eventually only affects the updates of non-dimensional reduced pressure $\vec{\delta}_{p^*}$ and cavity fraction $\vec{\delta}_\theta$, but never the computation of $\vec{G}$ and $\vec{F}$. The discrete formulations of the Jacobians $J_{G,p^*} = A_{Po} + A_h$ and $J_{G,\theta} = B$ are provided in [the] appendix [of [Hansen et al., 2022]]. The center entries of the Jacobians of the dimensionless Fischer-Burmeister equation $J_{F,p^*,C}$ and $J_{F,\theta,C}$ for each discrete point are [94]:

$$J_{F,p^*,C} = 1 - \frac{p^*_{C,aux}}{\sqrt{p^{*2}_{C,aux} + \theta^2_{C,aux}}}, \tag{3.9}$$

$$J_{F,\theta,C} = 1 - \frac{\theta_{C,aux}}{\sqrt{p^{*2}_{C,aux} + \theta^2_{C,aux}}} \tag{3.10}$$

Here, $p^*_{C,aux}$ and $\theta^*_{C,aux}$ are the auxiliary dimensionless pressure and cavity fraction which are adjusted such that J_{F,p^*} and $J_{F,\theta}$ do not become singular [94]. To prevent them from having center entries close to zero within the range $(-\varepsilon, \varepsilon)$, they are adjusted as:

$$p^*_{C,aux} = \begin{cases} p^*_C & \text{if } p^*_C \geq \varepsilon \text{ or } p^*_C \leq -\varepsilon, \\ \varepsilon & \text{if } 0 \leq p^*_C < \varepsilon, \\ -\varepsilon & \text{if } -\varepsilon < p^*_C < 0, \end{cases} \tag{3.11}$$

$$\theta_{C,aux} = \begin{cases} \theta_C & \text{if } \theta_C \geq \varepsilon \text{ or } \theta_C \leq -\varepsilon, \\ \varepsilon & \text{if } 0 \leq \theta_C < \varepsilon, \\ -\varepsilon & \text{if } -\varepsilon < \theta_C < 0, \end{cases} \tag{3.12}$$

where machine epsilon is given by $\varepsilon \approx 2.2204 \cdot 10^{-16}$. As already done in the original FBNS algorithm, the corresponding columns of the Jacobian J and rows of the updates $\vec{\delta}$ are swapped if $J_{F,p^*,C} < J_{F,\theta,C}$ to obtain a reordered system [94]:

$$\begin{bmatrix} A_F & B_F \\ A_G & B_G \end{bmatrix} \begin{bmatrix} \vec{\delta}_a \\ \vec{\delta}_b \end{bmatrix} = - \begin{bmatrix} \vec{F} \\ \vec{G} \end{bmatrix}. \tag{3.13}$$

Due to the swapping, A_F is better conditioned than J_{F,p^*} which is exploited when Equation system (3.13) is solved [94]:

$$\vec{\delta}_b = \left(B_G - A_G\left(A_F^{-1}B_F\right)\right)^{-1}\left(-\vec{G} + A_G\left(A_F^{-1}\vec{F}\right)\right), \tag{3.14}$$

$$\vec{\delta}_a = A_F^{-1}\left(-\vec{F} - B_F\vec{\delta}_b\right). \tag{3.15}$$

After obtaining $\vec{\delta}_a$ and $\vec{\delta}_b$, the earlier performed row swapping is reversed to get the updates of non-dimensional pressure $\vec{\delta}^n_{p^*}$ and cavity fraction $\vec{\delta}^n_\theta$ [94]. The new values $\vec{p}^{*,n}$ and $\vec{\theta}^n$ at iteration n are obtained by means of relaxation:

$$\vec{p}^{*,n} = \vec{p}^{*,n-1} + \alpha_{p^*}\vec{\delta}^n_{p^*}, \tag{3.16}$$

$$\vec{\theta}^n = \vec{\theta}^{n-1} + \alpha_\theta\vec{\delta}^n_\theta, \tag{3.17}$$

where α_{p^*}, $\vec{p}^{*,n-1}$, α_θ and $\vec{\theta}^{n-1}$ are the relaxation factors and previous solutions of non-dimensional reduced pressure and cavity fraction. Depending on the simulated case, relaxation coefficients between 0.05 and 1 resulted in good tradeoffs between convergence speed and stability. Preventing $\vec{p}^{*,n}$ from having values below 0 and $\vec{\theta}^n$ from having values below 0 or above 1 through truncation furthermore enhances favourable convergence properties.

If a constant load force is prescribed, the dimensionless rigid body displacement $h^*_d = h_d/h_{ref}$ is adjusted through a PID controller to meet the load balance Equation (2.3) as already done by Wang *et al.* [93]. This is done by first determining the resulting normal force F^n_N through the discretized load balance equation:

$$F^n_N = \sum^{N_{x_2}}\sum^{N_{x_1}}\left(p^n_{fl,C} - p_{amb}\right)\Delta x_1\Delta x_2, \tag{3.18}$$

where N_{x_1}, Δx_1, N_{x_2} and Δx_2 are the amount and spacing of the discretization cells in x_1- and x_2-direction and $p^n_{fl,C}$ is the fluid pressure at the center of each discrete cell. The residual of the load balance equation is defined as:

$$r^n_{F_N} = \frac{F^n_N - F_{N,imp}}{F_{N,ref}}, \tag{3.19}$$

where $F_{N,ref}$ is a reference normal force that is usually just set equal to the imposed normal load $F_{N,imp}$. Note that $r^n_{F_N}$ can be either positive or negative, depending on whether F^n_N is larger or smaller than $F_{N,imp}$. This is required for the PID controller to work properly. Finally, $r^n_{F_N}$ is fed into the PID controller to determine $h^{*,n+1}_d$ of the next iteration step [93]:

$$h^{*,n+1}_d = K_P r^n_{F_N} + K_I\sum_i^{n-1} r^i_{F_N} + K_D\left(r^n_{F_N} - r^{n-1}_{F_N}\right). \tag{3.20}$$

Note that K_I is only multiplied with the sum up until $r^{n-1}_{F_N}$, since $r^n_{F_N}$ is already considered by K_P" [Hansen et al., 2022]. This implementation works well in cases where the initial guess for the dimensionless rigid gap height displacement $h^{*,0}_d$ is close to zero. For other cases however, the following incremental PID controller showed better convergence properties:

$$h^{*,n+1}_d = \Delta h^{*,n}_d + h^{*,n}_d = \left(K_P\left(r^n_{F_N} - r^{n-1}_{F_N}\right) + K_I r^n_{F_N} + K_D\left(r^n_{F_N} - 2r^{n-1}_{F_N} + r^{n-2}_{F_N}\right)\right) + h^{*,n}_d. \tag{3.21}$$

"At last, the following residuals are computed:

$$\begin{aligned} r^n_{max,\delta p^*} &= \max\left(\text{abs}\left(\vec{\delta}^n_{p^*}\right)\right), \\ r^n_{max,\delta\theta} &= \max\left(\text{abs}\left(\vec{\delta}^n_{\theta}\right)\right), \\ r^n_{max,\delta G} &= \max\left(\text{abs}\left(\vec{G}^n - \vec{G}^{n-1}\right)\right), \\ r^n_{max,G} &= \max\left(\text{abs}\left(\vec{G}^n\right)\right), \\ r^n_{max,\delta F} &= \max\left(\text{abs}\left(\vec{F}^n - \vec{F}^{n-1}\right)\right), \\ r^n_{max,F} &= \max\left(\text{abs}\left(\vec{F}^n\right)\right), \end{aligned} \tag{3.22}$$

$$r^n_{EHL-FBNS} = \max\left(r^n_{max,\delta p^*}, r^n_{max,\delta\theta}, r^n_{max,\delta G}, r^n_{max,G}, r^n_{max,\delta F}, r^n_{max,F}\right). \tag{3.23}$$

Note that the residuals $r^n_{max,\delta G}$ and $r^n_{max,\delta F}$ are directly affected by the relaxation factors and $\vec{G}^n$ and $\vec{F}^n$ are computed through the solutions $\vec{p}^{*,n-1}$ and $\vec{\theta}^{n-1}$" [Hansen et al., 2022]. While the above expression for the residual $r^n_{EHL-FBNS}$ is the strictest definition possible, it can be too strict to obtain convergence for grids of low resolution. In order to enable consistent grid convergence studies with a large range of resolutions, the following less strict criterion only considers the convergence of the pressure field and can be employed as an alternative to Equation (3.23):

$$r^n_{EHL-FBNS} = \text{mean}\left(\text{abs}\left(\vec{\delta}^n_{p^*}\right)\right). \tag{3.24}$$

"The EHL-FBNS algorithm is repeated as long as $r^n_{EHL-FBNS}$ and in case of an imposed normal load force abs$(r^n_{F_N})$ are above the tolerance tol. The initial guess is always a zero cavity fraction field and a fluid pressure field at ambient pressure. If an unsteady simulation is performed, the solution at $t = 0$ is obtained through the steady problem caused by the geometry at $t = 0$. Furthermore, the PID controller also takes the residuals of the load balance equation of the previous time steps into account if $t > 0$" [Hansen et al., 2022].

3.2 HMEHL-FBNS Solver

"In order to simulate the conditions within the macroscopic scale of the lubrication flow [for all lubrication regimes of] the Stribeck curve [...], a homogenized mixed elasto-hydrodynamic lubrication Fischer-Burmeister-Newton-Schur (HMEHL-FBNS) solver implementation in MATLAB© is employed" [Hansen et al., 2023]. It extends the EHL-FBNS solver by averaging the effect of roughness on the contact pressure and the Reynolds equation, thus enabling the simulation of mixed and boundary lubrication. This is implemented by splitting the simulation in two consecutive steps. During the preprocessing, averaged quantities are computed for representative roughness geometries. Afterwards, these averaged roughness quantities are employed in a simulation on the macroscopic scale such that a solution over the whole macroscopic geometry is obtained.

3.2.1 Roughness Preprocessing

"Microscopic [roughness] geometries are used to compute the mean contact pressures, mean gap heights and homogenization factors for 100 distinct rigid body displacements on the roughness scale h_0 in an

exponentially spaced range between $h_{0,r,min} = 0.1\,\mu\mathrm{m}$ and $h_{0,r,max} = 1\,\mu\mathrm{m}$. The averaging is performed over the periodic roughness domain lengths $L_{r,1}$ and $L_{r,2}$ and the periodic roughness time length T_r. [The domain is discretized into $N_{r,1} \times N_{r,2}$ points.] For each rigid body displacement, $N_{r,t} = 32$ discrete time steps are used to periodically move the roughness profile of the disk in the x_1-direction once over the roughness profile of the pin. At each time t, the asperity contact pressure p_{asp} and deformed gap height distributions h are computed at each spatial position (x_1,x_2) with a dry contact solver for periodic problems. It is of conjugate gradient-fast Fourier transform (CG-FFT) type and its algorithm is mainly based on the description by Akchurin *et al.* [1]. [As described priorly in Section 2.9.2,] the code computes the equilibrium of elastic deformation and asperity contact pressure for the imposed h_0 while using cyclic convolutions with the kernel function derived from the elastic half-space theory when constant pressure over rectangular discretization cells is assumed [49, Ch. 3.3], [65]. The Young's modulus E and Poisson ratio ν of the upper and lower surfaces are considered in the kernel function. Within the contact region, the asperity contact pressure can take values between zero as a lower limit and the hardness Hrd of the material as a maximum limit [90]. Outside of the contact zone, the pressure is set to zero. The obtained gap height distribution h is truncated below $1\,\mathrm{nm}$ and used to compute solutions [...] of the unsteady local problems" [Hansen et al., 2023]. Differently to Section 2.9.2, the equilibrium of h and p_{asp} is not computed in the theoretic space of the microscopic coordinates $\vec{\xi} = \vec{x}/\epsilon$, but instead directly in the space of the original coordinates $\vec{x}$. Furthermore in Section 2.9.1, the local problems and homogenization factors were also expressed in the microscopic coordinates $\vec{\xi}$ and $\kappa = t/\epsilon$, but they are reformulated such that they can be computed directly for any gap height distribution h that is parameterized with the original coordinates x_1 and x_2. Substituting $\nabla_{\vec{\xi}} = \epsilon\nabla_{\vec{x}}$, $\partial/\partial\kappa = \epsilon\partial/\partial t$ and $\epsilon\chi_i = \chi_{i,\vec{x}}$ into Equations (2.77-2.79) yields the local problems as a function of the coordinates x_1, x_2 and t that are solved for their solutions $\chi_{1,\vec{x}}$, $\chi_{2,\vec{x}}$ and $\chi_{3,\vec{x}}$ [Hansen et al., 2023]:

$$\nabla_{\vec{x}} \cdot \left(h^3 \nabla_{\vec{x}} \chi_{1,\vec{x}}\right) = \frac{\partial h}{\partial x_1} + \frac{1}{u_m}\frac{\partial h}{\partial t}, \tag{3.25}$$

$$\nabla_{\vec{x}} \cdot \left(h^3 \nabla_{\vec{x}} \chi_{2,\vec{x}}\right) = -\frac{\partial h^3}{\partial x_1}, \tag{3.26}$$

$$\nabla_{\vec{x}} \cdot \left(h^3 \nabla_{\vec{x}} \chi_{3,\vec{x}}\right) = -\frac{\partial h^3}{\partial x_2}. \tag{3.27}$$

"For the first time step, the steady problem is solved by neglecting the unsteady term. The local problems are discretized with the FVM. Second-order central schemes are used for the spatial derivatives, while the first-order Euler implicit scheme is used for the temporal derivative. Periodic boundary conditions are employed. One point of the domain is used for the Dirichlet condition $\chi_{1,\vec{x}} = \chi_{2,\vec{x}} = \chi_{3,\vec{x}} = 0$. The value of the Dirichlet condition can be chosen arbitrarily and does not influence the final homogenization factors since they are only a function of the gradients of $\chi_{1,\vec{x}}$, $\chi_{2,\vec{x}}$ and $\chi_{3,\vec{x}}$. Furthermore, the discretized form of Equation (3.25) becomes independent of u_m by setting the time step size to $L_{r,1}/(N_{r,t}u_m)$, thus cancelling out u_m in the final expression. Once all time steps are solved for, their average is computed to obtain the mean contact pressure $\overline{p}_{con}$, mean gap height $\overline{h}$ and the homogenization factors A, $\vec{b}$, C and $\vec{d}$" [Hansen et al., 2023]:

$$\overline{p}_{con}(h_0) = \frac{1}{N_{r,1}N_{r,2}N_{r,t}} \sum^{N_{r,t}} \sum^{N_{r,2}} \sum^{N_{r,1}} p_{asp}, \tag{3.28}$$

$$\overline{h}(h_0) = \frac{1}{N_{r,1}N_{r,2}N_{r,t}} \sum^{N_{r,t}} \sum^{N_{r,2}} \sum^{N_{r,1}} h, \tag{3.29}$$

$$A(h_0) = \frac{1}{N_{r,1}N_{r,2}N_{r,t}} \sum^{N_{r,t}} \sum^{N_{r,2}} \sum^{N_{r,1}} \frac{h^3}{\overline{h}^3} \begin{pmatrix} 1 + \frac{\partial \chi_{2,\vec{x}}}{\partial x_1} & \frac{\partial \chi_{3,\vec{x}}}{\partial x_1} \\ \frac{\partial \chi_{2,\vec{x}}}{\partial x_2} & 1 + \frac{\partial \chi_{3,\vec{x}}}{\partial x_2} \end{pmatrix}, \tag{3.30}$$

$$\vec{b}(h_0) = \frac{1}{N_{r,1}N_{r,2}N_{r,t}} \sum^{N_{r,t}} \sum^{N_{r,2}} \sum^{N_{r,1}} \frac{h}{\overline{h}} \begin{pmatrix} 1 - h^2 \frac{\partial \chi_{1,\vec{x}}}{\partial x_1} \\ -h^2 \frac{\partial \chi_{1,\vec{x}}}{\partial x_2} \end{pmatrix} \tag{3.31}$$

,

$$C(h_0) = \frac{1}{N_{r,1}N_{r,2}N_{r,t}} \sum^{N_{r,t}} \sum^{N_{r,2}} \sum^{N_{r,1}} \frac{h}{\overline{h}} \begin{pmatrix} 1 + \frac{\partial \chi_{2,\vec{x}}}{\partial x_1} & \frac{\partial \chi_{3,\vec{x}}}{\partial x_1} \\ \frac{\partial \chi_{2,\vec{x}}}{\partial x_2} & 1 + \frac{\partial \chi_{3,\vec{x}}}{\partial x_2} \end{pmatrix}, \tag{3.32}$$

$$\vec{d}(h_0) = \frac{1}{N_{r,1}N_{r,2}N_{r,t}} \sum^{N_{r,t}} \sum^{N_{r,2}} \sum^{N_{r,1}} h\overline{h} \begin{pmatrix} \frac{\partial \chi_{1,\vec{x}}}{\partial x_1} \\ \frac{\partial \chi_{1,\vec{x}}}{\partial x_2} \end{pmatrix}. \tag{3.33}$$

3.2.2 Governing Equations of the Macroscopic Scale

"The fundamental equations [employed on the macroscopic scale] are summarized in the following. The difference between the macroscopic fluid pressure $p_{0,fl}$ and cavitation pressure p_{cav} is called macroscopic reduced pressure $p_0 = p_{0,fl} - p_{cav}$. The cavity fraction θ is defined as $\theta = 1 - \frac{\rho}{\rho_l}$, where ρ is the mixture density of the flow and ρ_l is the density of the liquid phase. $p_{0,fl}$ and θ are determined at each position (x_1, x_2) on the macroscopic scale with the steady homogenized Reynolds equation and the complementary cavitation constraint:

$$0 = \nabla \cdot \left(\frac{\rho_l \overline{h}^3}{12\mu_l} A \nabla p_0 - \rho_l \overline{h} u_m \vec{b} (1 - \theta) \right), \tag{3.34}$$

$$p_0 \theta = 0, \quad p_0 \geq 0, \quad \theta \geq 0, \tag{3.35}$$

where the dynamic viscosity of the liquid phase μ_l, mean velocity u_m, mean gap height $\overline{h}$ and homogenization factors A and $\vec{b}$ are incorporated [...]. $\overline{h}$ and the homogenization factors A and $\vec{b}$ are functions of the rigid body displacement on the roughness scale h_0. Their values and the mean contact pressure $\overline{p}_{con}(h_0)$ can be interpolated at each position (x_1, x_2) on the macroscopic scale by realizing that the macroscopic gap height is the same as the rigid body displacement on the roughness scale h_0. On the macroscopic scale, h_0 can be determined as:

$$h_0 = h_{0,d} + h_{0,ri} + h_{0,el}(p_{tot}), \tag{3.36}$$

where $h_{0,d}$ denotes the rigid body displacement between the upper and lower macrogeometries, $h_{0,ri}$ is the gap height variation due to the rigid macrogeometries and $h_{0,el}$ describes the combined elastic deformation of the macrogeometries. [The macroscopic rigid body displacement $h_{0,d}$ is determined by the solver such that the load balance Equation (2.3) is fulfilled by the macroscopic total pressure p_{tot}.] Using the elastic-half space assumption, $h_{0,el}$ is [computed according to Equation (2.19)], where the macroscopic total pressure

$$p_{tot} = p_{0,fl} + \overline{p}_{con} \tag{3.37}$$

is a superposition of the macroscopic fluid pressure $p_{0,fl}$ and the mean contact pressure $\overline{p}_{con}$ within the domain of size $L_1 L_2$ [...]. [Piezoviscosity and compressibility of the liquid phase are incorporated with the Roelands Equation (2.55) and the Dowson–Higginson Equation (2.56) by expressing them as functions of the macroscopic fluid pressure $p_{0,fl} = p_0 + p_{cav}$.] In summary, the consequences of the employed models for the dynamic viscosity and density are as follows: while each simulation for itself is isothermal, the lubricant's dependence upon temperature is still considered by the corresponding value of μ_0 [...]. The density is treated analogously. However, unlike μ_0, the value of ρ_0 can actually be eliminated from the homogenized Reynolds Equation (3.34), because it appears in each single term. Consequently, the temperature dependence of ρ_0 does not need any special consideration in the employed model. Lastly, an estimate of the magnitude of ρ_0 is still necessary for the underlying EHL-FBNS solver [...] to create the non-dimensional system of equations. Nonetheless, piezoviscous and compressible effects are considered by Equations (2.55) and (2.56). They allow for the dynamic viscosity and density to change throughout the simulation domain according to the fluid pressure field" [Hansen et al., 2023].

3.2.3 Algorithm of the Macroscopic Simulation

The previously described governing equations can be easily incorporated into the EHL-FBNS algorithm. Analogously to Section 3.1.2, the homogenized Reynolds equation is firstly put into dimensionless form:

$$\begin{aligned} G = &\frac{\partial}{\partial x_1^*}\left(\frac{\rho^*\overline{h}^{*3}}{\mu^*}\left(A_{11}\frac{\partial p_0^*}{\partial x_1^*} + A_{12}\frac{x_{1,ref}}{x_{2,ref}}\frac{\partial p_0^*}{\partial x_2^*}\right)\right) + \frac{\partial}{\partial x_2^*}\left(\frac{\rho^*\overline{h}^{*3}}{\mu^*}\left(A_{21}\frac{x_{1,ref}}{x_{2,ref}}\frac{\partial p_0^*}{\partial x_1^*} + A_{22}\left(\frac{x_{1,ref}}{x_{2,ref}}\right)^2\frac{\partial p_0^*}{\partial x_2^*}\right)\right) \\ &- \frac{\partial}{\partial x_1^*}\left(12\frac{x_{1,ref}u_{m,ref}\mu_{ref}}{h_{ref}^2 p_{ref}}\rho_l^*\overline{h}^* u_m^* b_1\,(1-\theta)\right) - \frac{\partial}{\partial x_2^*}\left(12\frac{x_{1,ref}^2 u_{m,ref}\mu_{ref}}{x_{2,ref}h_{ref}^2 p_{ref}}\rho_l^*\overline{h}^* u_m^* b_2\,(1-\theta)\right) \\ &- \frac{\partial}{\partial t^*}\left(12\frac{x_{1,ref}^2\mu_{ref}}{t_{ref}h_{ref}^2 p_{ref}}\rho_l^*\overline{h}^*(1-\theta)\right). \end{aligned} \tag{3.38}$$

"[This equation] is discretized with the FVM, where the Poiseuille terms are discretized with a second-order central scheme and the Couette term with a first-order upwind scheme" [Hansen et al., 2023]. Subsequently, almost the same algorithm as described in Section 3.1.2 can be applied to obtain the values of the dimensionless macroscopic reduced pressure $\vec{p}_0^{*,n}$ and cavity fraction $\vec{\theta}^n$ at each iteration n. Contrary to the EHL-FBNS alorithm, the mean gap height $\overline{h}$, the homogenization factors A and $\vec{b}$ and the mean contact pressure $\overline{p}_{con}(h_0)$ are interpolated at each position (x_1, x_2) according to h_0. "If [during the interpolation process], h_0 is larger than the [in Section 3.2.1 described] $h_{0,r,max}$ [...], then $\overline{h}$ is set equal to h_0, the mean contact pressure is set to 0 and the homogenization factors are set to their value at $h_{0,r,max}$, thus being close to either 0 or 1 depending on the factor. [Additionally], the update of the mean contact pressure is computed as:

$$\delta_{\overline{p}_{con}}^n = \overline{p}_{con}(h_0) - \overline{p}_{con}^{n-1}, \tag{3.39}$$

where $\overline{p}_{con}(h_0)$ is the expected mean contact pressure according to $h_0(x_1, x_2)$ and $\overline{p}_{con}^{n-1}$ describes the mean contact pressure of the previous iteration. For stability reasons, this update is applied with an underrelaxation coefficient $\alpha_{\overline{p}_{con}}$ to obtain the mean contact pressure at iteration n:

$$\overline{p}_{con}^n = \overline{p}_{con}^{n-1} + \alpha_{\overline{p}_{con}}\delta_{\overline{p}_{con}}^n \tag{3.40}$$

At the end of each iteration, $\overline{p}^n_{con}$ is used to compute p_{tot} according to Equation (3.37). Furthermore, the residual of $\overline{p}_{con}$ is computed as" [Hansen et al., 2023]:

$$r_{max,\delta\overline{p}^*_{con}} = \max\left(\mathrm{abs}\left(\frac{\delta^n_{\overline{p}_{con}}}{p_{ref}}\right)\right). \tag{3.41}$$

The residual of the HMEHL-FBNS algorithm that has to meet the tolerance tol can be defined either strictly as:

$$r^n_{HMEHL-FBNS} = \max\left(r_{max,\delta\overline{p}^*_{con}}, r^n_{max,\delta p^*}, r^n_{max,\delta\theta}, r^n_{max,\delta G}, r^n_{max,G}, r^n_{max,\delta F}, r^n_{max,F}\right) \tag{3.42}$$

or only as a function of the dimensionless macroscopic reduced and mean contact pressure updates:

$$r^n_{HMEHL-FBNS} = \max\left(r_{max,\delta\overline{p}^*_{con}}, r^n_{max,\delta p^*}\right). \tag{3.43}$$

The normal force is evaluated at each iteration by:

$$F^n_N = \sum^{N_{x_2}}\sum^{N_{x_1}}\left(p^n_{tot,C} - p_{amb}\right)\Delta x_1 \Delta x_2, \tag{3.44}$$

where N_{x_1}, Δx_1, N_{x_2} and Δx_2 are the amount and spacing of the discretization cells in x_1- and x_2-direction and $p^n_{tot,C}$ is the macroscopic total pressure at the center of each discrete cell. The residual of the load balance equation is again defined as:

$$r^n_{F_N} = \frac{F^n_N - F_{N,imp}}{F_{N,ref}}. \tag{3.45}$$

"In the solver, the macroscopic rigid body displacement between the upper and lower macroscopic geometries h_d is adjusted through an incremental PID controller with its coefficients K_P, K_I and K_D:

$$h^{n+1}_d = \Delta h^n_d + h^n_d = \left(K_P\left(r^n_{F_N} - r^{n-1}_{F_N}\right) + K_I r^n_{F_N} + K_D\left(r^n_{F_N} - 2r^{n-1}_{F_N} + r^{n-2}_{F_N}\right)\right)\cdot h_{ref} + h^n_d. \tag{3.46}$$

This is performed at each iteration until a prescribed tolerance is met by the residual [of the load balance Equation $r^n_{F_N}$]. Lastly, the homogenized viscous stresses on the pin surface are computed with the homogenized shear stress equation:

$$\begin{pmatrix}\overline{\tau}_{fl,1}|_{r_\tau=0}\\ \overline{\tau}_{fl,2}|_{r_\tau=0}\end{pmatrix} = -\frac{h_m}{2}C\nabla p_+ \frac{\mu_l}{h_m}\left(-6u_m\vec{d} + u_r\begin{pmatrix}1\\0\end{pmatrix}\right)(1-\theta), \tag{3.47}$$

where C and $\vec{d}$ are homogenization factors and u_r is the relative velocity between the upper and lower surfaces [...]. The tangential contact stress is determined as:

$$\overline{\tau}_{con,1} = \mathrm{sign}(u_r)C_{f,b}\overline{p}_{con}, \tag{3.48}$$

where $C_{f,b}$ is an estimate for the boundary friction coefficient. It is set to $C_{f,b} = 1/(3\sqrt{3})$, which is a value theoretically derived by Bowden and Tabor [14, Ch. V] for the dry friction of metals under pure

shearing [and] serves as an unambiguous and uniquely defined upper limit for the boundary friction coefficient [Hansen et al., 2020]. The total shear stress

$$\tau_{tot} = \overline{\tau}_{fl,1}\big|_{r_\tau=0} + \overline{\tau}_{con,1} \tag{3.49}$$

is computed by superposition and used to determine the resulting friction force F_T:

$$F_T = \sum^{N_{x_2}} \sum^{N_{x_1}} \tau_{tot} \Delta x_1 \Delta x_2. \tag{3.50}$$

Eventually the friction coefficient is evaluated as" [Hansen et al., 2023]:

$$C_f = \frac{F_T}{F_N}. \tag{3.51}$$

4 Single Textures in Full-Film Conditions

This chapter is based on the publication *An EHL Extension of the Unsteady FBNS Algorithm* by [Hansen et al., 2022]. The findings of the cited publication are essential to this thesis because the knowledge gained under full-film conditions is the foundation of the mixed lubrication investigations in the following chapters. "[Within this chapter], the results of the EHL-FBNS algorithm are compared to the analytical solution of a rigid one-dimensional convergent slider with rectangular pocket to show the effect of the discretization order of the Couette term on the accuracy of the simulation results when gap height discontinuities are present. Subsequently, the slider is extended to a two-dimensional geometry and an elastic model is employed to give an example case where both mass-conserving cavitation and elasticity show relevant effects. Afterwards, another experimental-numerical literature case is simulated with the EHL-FBNS algorithm to validate the code for textured ball-on-disk investigations, evaluate the code's stability in unsteady EHL conditions and compare different spatial discretization schemes. For all considered cases, the second order midpoint rule is used for the evaluation of integrals arising from the FVM and the Poiseuille term is always discretized with a second order central scheme. Consequently, the resulting order of the dimensionless Reynolds equation discretized with the FVM in the steady case is first order with the UI and second order with the QUICK scheme. In the unsteady case, only first order is achievable for both UI and QUICK since the first order Euler implicit scheme is employed. All of the EHL-FBNS simulations are performed with MATLAB© R2020a" [Hansen et al., 2022].

4.1 Convergent Slider with Rectangular Pocket

"The [first] test case is a convergent slider with a single rectangular pocket that introduces discontinuities in the gap height. For this set-up, a mass-conserving cavitation model is essential to predict the full-film reformulation properly. The aim of the simulations is to show the effect of the spatial discretization order on the pressure distribution when gap height discontinuities are present. For this steady case, the UI scheme eventually results in first and the QUICK scheme in second order accuracy. The investigation is firstly done for a rigid one-dimensional geometry because it has the analytical solution of Fowell *et al.* [33] for comparison. Next, the two-dimensional set-up of Bertocchi *et al.* [11] is used on the one hand to demonstrate that the algorithm of Bertocchi *et al.* and the EHL-FBNS algorithm give consistent results in the rigid case and on the other hand to show that the additional consideration of elastic deformations even at traditional hydrodynamic operating conditions is of great relevance. A sketch of the one-dimensional configuration is depicted in Figure 4.1 (a) while its extension to the two-dimensional geometry is described in Figure 4.1 (b).

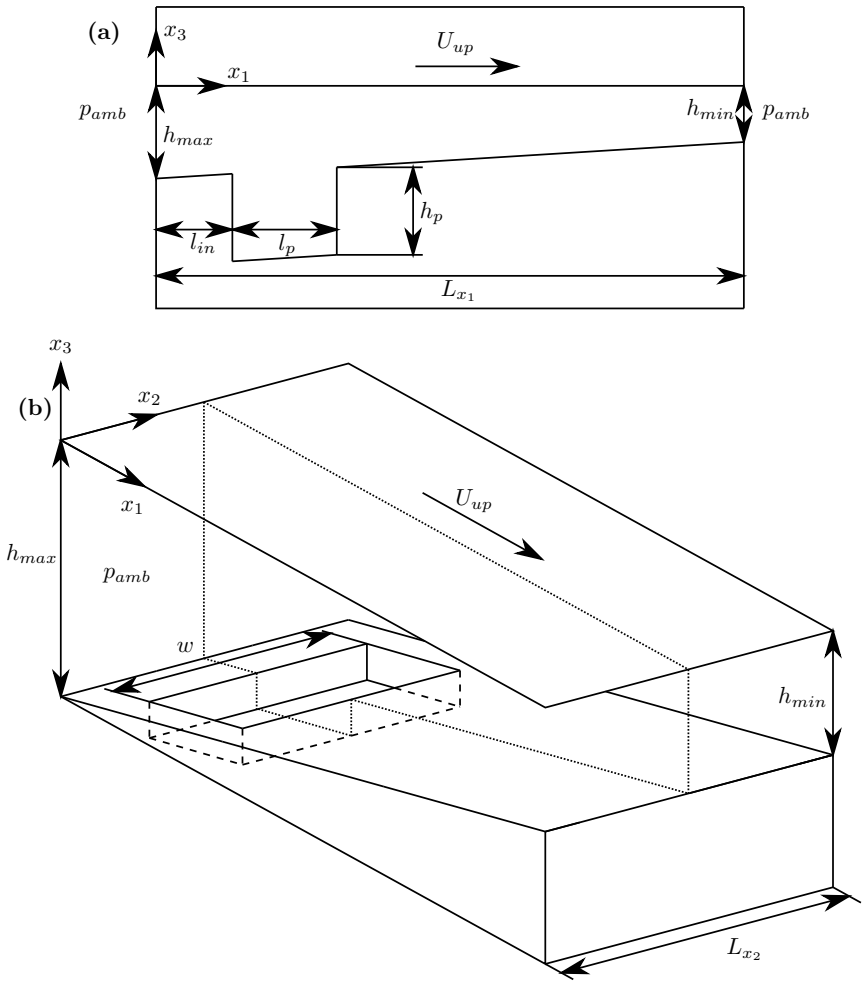

Figure 4.1: "Schematic sketch of the convergent slider with rectangular pocket: (a) one-dimensional configuration, (b) two-dimensional geometry with one-dimensional configuration along center line. Adapted from the publication by Bertocchi *et al.* [11]." The figure including its caption is adapted from the publication by [Hansen et al., 2022].

The analytical solution of a rigid one-dimensional converging slider with rectangular pocket and incompressible isoviscous liquid phase was derived by Fowell *et al.* [33] and was also used for code verification by Giacopini *et al.* [34]. The parameters used in the current study are summarized in Table 4.1. [Considering the fluid, the values correspond to the general magnitude of additive-free base oil as measured by [Hansen et al., 2023].] The one-dimensional geometry was replicated by a pseudo one-dimensional grid with three discretization points in x_2-direction and Neumann boundary conditions for pressure and cavity fraction at the south ($x_2 = 0$) and north ($x_2 = L_{x_2}$) boundary. [The west ($x_1 = 0$) and east ($x_1 = L_{x_1}$) boundaries employ Dirichlet boundary conditions of ambient pressure and zero cavity fraction.]

To investigate the grid convergence properties of the spatial schemes for this kind of set-up, the resulting pressure profiles of the UI and QUICK schemes are shown in Figures 4.2 and 4.3 for different grid resolutions alongside the analytical solution. While both schemes converge towards the same analytical solution, the first order UI scheme converges faster at much lower resolutions than the second order QUICK scheme. It is therefore concluded that for rigid geometries, lower order discretization schemes are preferable when gap height discontinuities are present.

Parameter	Value	Parameter	Value	Parameter	Value
U_{up}	$1\ \mathrm{ms}^{-1}$	μ_0	10^{-2} Pas	N_{x_2}	3
U_{low}	0	α_B	-	L_{x_1}	10^{-2} m
u_m	$0.5\ \mathrm{ms}^{-1}$	α_R	-	L_{x_2}	$(N_{x_2}-1)\Delta x_2$
u_r	$1\ \mathrm{ms}^{-1}$	$p_{0,R}$	-	h_d	0
p_{amb}	10^5 Pa	ρ_0	$850\ \mathrm{kgm}^{-3}$	h_{max}	$1.05 \cdot 10^{-6}$ m
p_{cav}	0	C_1	-	h_{min}	10^{-6} m
$p_{fl,SB}$	Neumann	C_2	-	l_{in}	$2 \cdot 10^{-3}$ m
$p_{fl,WB}$	p_{amb}	E_{up}	-	l_p	$3 \cdot 10^{-3}$ m
$p_{fl,EB}$	p_{amb}	E_{low}	-	Δx_1	$L_{x_1}/(N_{x_1}-1)$
$p_{fl,NB}$	Neumann	ν_{up}	-	Δx_2	Δx_1
θ_{SB}	Neumann	ν_{low}	-	h_p	10^{-6} m
θ_{WB}	0	E'	-	α_{p^*}	0.5
θ_{EB}	0	$F_{N,imp}$	-	α_θ	0.5
θ_{NB}	Neumann	p_{ref}	10^6 Pa	ρ_{ref}	ρ_0
h_{ref}	h_{min}	t_{ref}	-	μ_{ref}	μ_0
$x_{1,ref}$	L_{x_1}	$F_{N,ref}$	-	u_{ref}	u_m
$x_{2,ref}$	L_{x_2}	-	-	-	-

Parameter	Value
N	243, 483, 963, 1923
N_{x_1}	81, 161, 321, 641

Table 4.1: "Summary of the parameters and values used in the EHL-FBNS simulations of the one-dimensional convergent slider with rectangular pocket." The table including its caption is adapted from the publication by [Hansen et al., 2022].

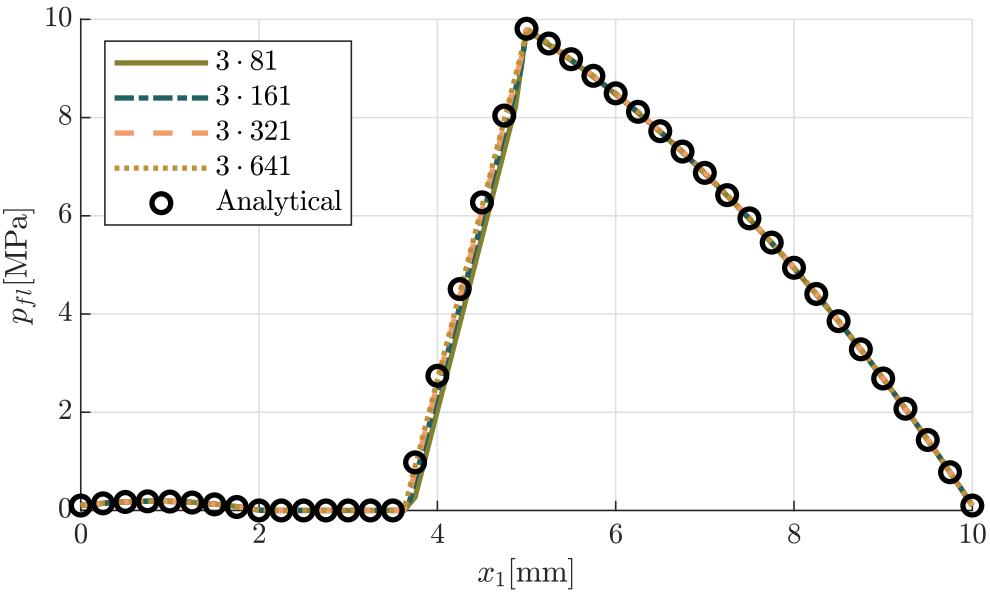

Figure 4.2: "Fluid pressure profile p_{fl} for UI simulations with different resolutions $N_{x_2} \cdot N_{x_1}$ in comparison to the analytical solution derived by Fowell *et al.* [33]." The figure including its caption is adapted from the publication by [Hansen et al., 2022].

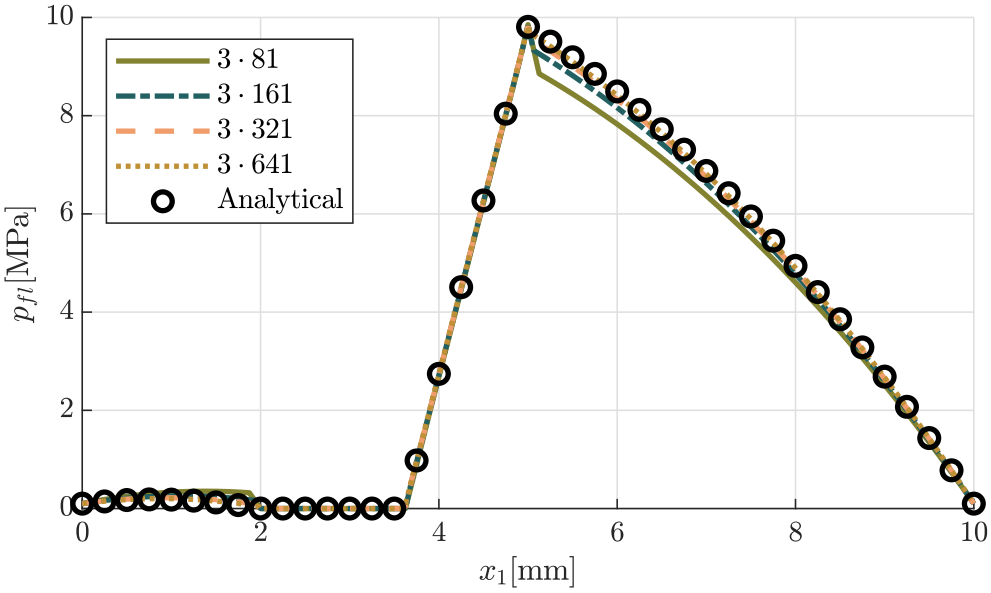

Figure 4.3: "Fluid pressure profile p_{fl} for QUICK simulations with different resolutions $N_{x_2} \cdot N_{x_1}$ in comparison to the analytical solution derived by Fowell *et al.* [33]." The figure including its caption is adapted from the publication by [Hansen et al., 2022].

Next, the two-dimensional set-up of a converging slider with rectangular pocket is considered. It is the same set-up that was used by Bertocchi *et al.* [11] to show the agreement of their code with the formulation of Ausas *et al.* [7] and Giacopini *et al.* [34]. This set-up is simulated to demonstrate the good agreement of the EHL-FBNS algorithm with the aforementioned algorithms in the rigid case and to point out that the resulting pressure distribution is greatly affected when common elastic bodies instead of rigid ones are used. The parameters employed in the EHL-FBNS simulations are summarized in Table 4.2. In the rigid case, Bertocchi *et al.* [11] used a domain width of $L_{x_2} = 10$ mm and pocket width of $w = 7$ mm to compare their results with the formulation of Ausas *et al.* [7] and employed a domain width of $L_{x_2} = 300$ mm and pocket width of $w = 210$ mm to approximate a one-dimensional case along the center line of the computational domain which was compared to the one-dimensional results of Giacopini *et al.* [34]. Differently to the non-equidistant mesh used by Bertocchi *et al.* consisting of 3528 elements, the EHL-FBNS simulations are performed with a mesh of 8320 cells and an equidistant spacing in each of the respective directions. Dirichlet boundary conditions of p_{amb} and zero cavity fraction are employed. Piezoviscosity is modelled with the Barus model and compressibility of the liquid phase with the Dowson-Higginson model. [The employed pressure viscosity coefficient of the Barus model is typical for mineral oils [89, Ch. 1.3.3] while the used constants in the Dowson-Higginson model correspond to weaker compression effects than usually simulated for mineral oils [64].] Differently to Bertocchi *et al.* shear thinning is neglected. As the following comparison of the EHL-FBNS results with the ones of Bertocchi *et al.* shows, shear thinning has a negligible effect for this problem. [The Young's modulus and Poisson ratio correspond to steel [41].] The EHL-FBNS simulations are performed with the UI and QUICK scheme and for rigid and elastic surfaces.

Parameter	Value	Parameter	Value	Parameter	Value
U_{up}	$1\ \mathrm{ms}^{-1}$	μ_0	10^{-2} Pas	N	8320
U_{low}	0	α_B	$1.2 \cdot 10^{-8}\ \mathrm{Pa}^{-1}$	N_{x_1}	128
u_m	$0.5\ \mathrm{ms}^{-1}$	α_R	-	N_{x_2}	65
u_r	$1\ \mathrm{ms}^{-1}$	$p_{0,R}$	-	L_{x_1}	$2 \cdot 10^{-2}$ m
p_{amb}	10^5 Pa	ρ_0	$850\ \mathrm{kgm}^{-3}$	h_d	0
p_{cav}	0	C_1	$2.22 \cdot 10^9$ Pa	h_{max}	$1.1 \cdot 10^{-6}$ m
$p_{fl,SB}$	p_{amb}	C_2	1.66	h_{min}	10^{-6} m
$p_{fl,WB}$	p_{amb}	E_{low}	E_{up}	l_{in}	$4 \cdot 10^{-3}$ m
$p_{fl,EB}$	p_{amb}	ν_{low}	ν_{up}	l_p	$6 \cdot 10^{-3}$ m
$p_{fl,NB}$	p_{amb}	$F_{N,imp}$	-	Δx_1	$L_{x_1}/(N_{x_1}-1)$
θ_{SB}	0	α_{p^*}	0.05	Δx_2	$L_{x_2}/(N_{x_2}-1)$
θ_{WB}	0	α_θ	0.05	h_p	$0.4 \cdot 10^{-6}$ m
θ_{EB}	0	p_{ref}	10^7 Pa	ρ_{ref}	ρ_0
θ_{NB}	0	t_{ref}	-	μ_{ref}	μ_0
h_{ref}	h_{min}	$F_{N,ref}$	-	u_{ref}	u_m
$x_{1,ref}$	L_{x_1}	$x_{2,ref}$	L_{x_2}	-	-

Parameter	Value
E_{up}	- , $210 \cdot 10^9$ Pa
ν_{up}	- , 0.3
E'	- , $231 \cdot 10^9$ Pa
L_{x_2}	10^{-2} m , $30 \cdot 10^{-2}$ m
w	$7 \cdot 10^{-3}$ m , $30 \cdot 7 \cdot 10^{-3}$ m

Table 4.2: "Summary of the parameters and values used in the EHL-FBNS simulations of the two-dimensional convergent slider with rectangular pocket." The table including its caption is adapted from the publication by [Hansen et al., 2022].

Figure 4.4 shows the pressure distribution of the rigid UI EHL-FBNS simulations along the center line for both geometry widths next to the results of Bertocchi *et al.* [11]. The curve of Bertocchi *et al.* was read in with the software Engauge Digitizer and can therefore be subject to minor deviation from the original data. Still, the results of the EHL-FBNS algorithm and Bertocchi *et al.* are similar. Furthermore, Bertocchi *et al.* found their results being in close agreement to Ausas *et al.* [7] and Giacopini *et al.* [34]. This indicates that the EHL-FBNS algorithm is consistent with all the mentioned works.

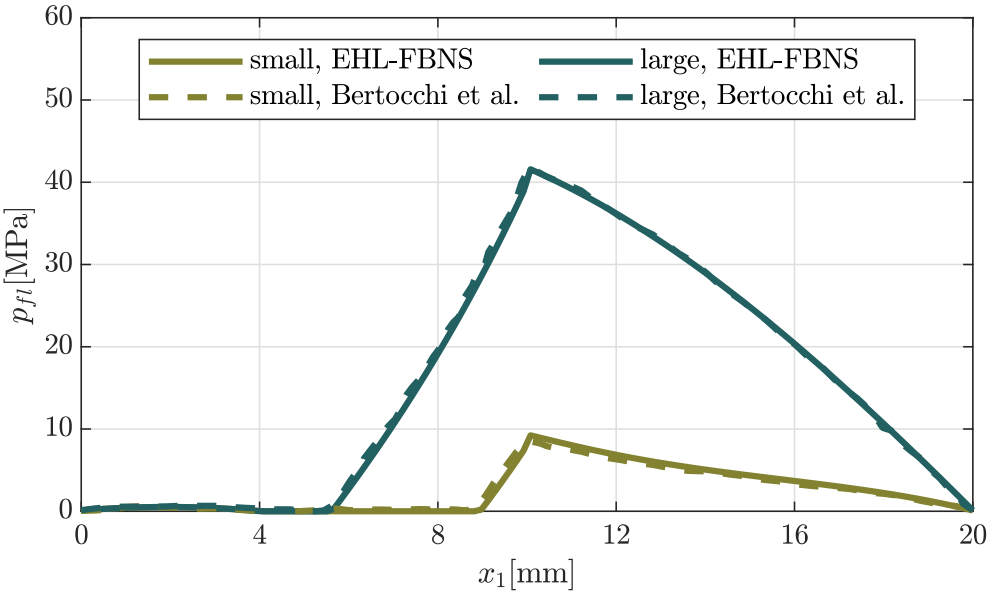

Figure 4.4: "Distribution of fluid pressure p_{fl} along the center line of the inclined slider with pocket against the results obtained by Bertocchi *et al.* [11]. Simulations were performed for the small ($L_{x_2} = 10$ mm, $w = 7$ mm) and large ($L_{x_2} = 30 \cdot 10$ mm, $w = 30 \cdot 7$ mm) geometry." The figure including its caption is adapted from the publication by [Hansen et al., 2022].

In the following, only the small geometry ($L_{x_2} = 10$ mm, $w = 7$ mm) is considered to show that even at traditional hydrodynamic operating conditions with low pressures between 1 and 10 MPa, the employment of common elastic parameters can induce small variations in the gap height which in turn severely alter the resulting fluid pressure and cavity fraction profiles. The resulting pressure profiles of the rigid and elastic simulations are shown in Figure 4.5 for the UI scheme. The boundary of the cavitation region is indicated by an orange line and the center line is marked in green. [The cavitation region is defined as the area where the cavitation pressure p_{cav} is reached by the fluid pressure p_{fl}.] The resulting pressure profiles are severely weakened due to the introduced elastic deformation and the cavitation region has a larger downstream extension.

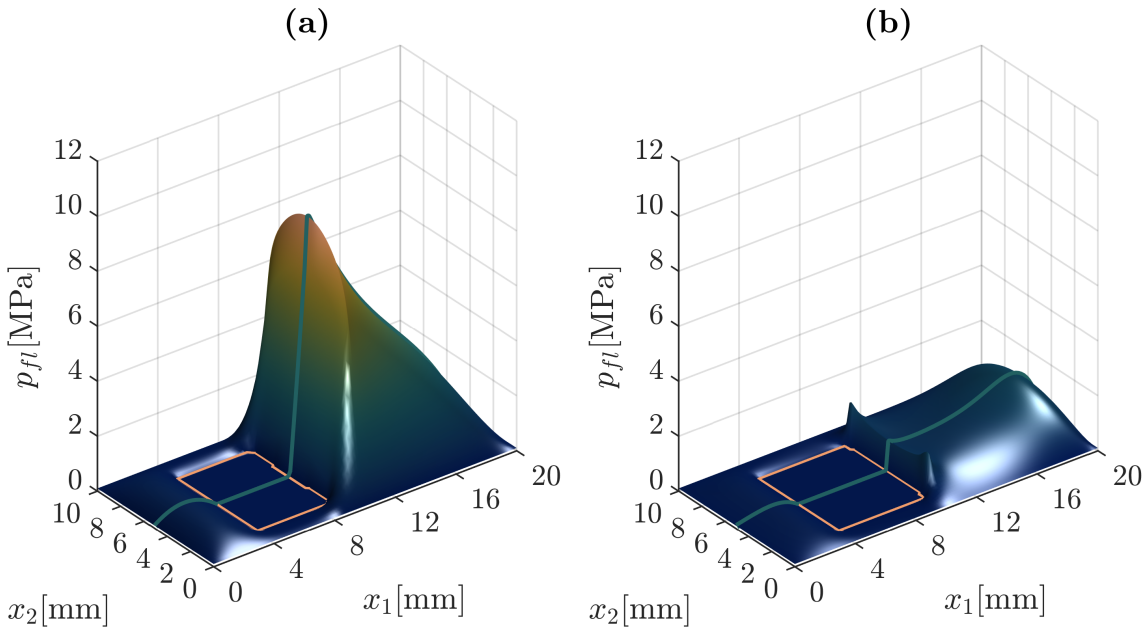

Figure 4.5: "Distribution of fluid pressure p_{fl} in the inclined slider with pocket for UI discretization and rigid **(a)** and elastic **(b)** model." The figure including its caption is adapted from the publication by [Hansen et al., 2022].

The gap height h, fluid pressure p_{fl} and cavity fraction θ along the center line are compared in Figure 4.6 for the rigid, elastic, UI and QUICK simulations. It becomes visible that the differences between rigid and elastically deformed gap height are small compared to the corresponding differences in the fluid pressure. The maximum fluid pressure is not only reduced to about 20%, but also the general shape and peak change drastically. In the elastic case, the cavitation region extends over the whole length of the pocket, thus reducing the area of positive pressure gradient in front of the downstream end of the pocket and eventually causing only a small pressure increase compared to the rigid case. Comparing the UI and QUICK schemes shows a tendency of the higher order scheme to cause oscillations at the downstream end of the cavitation region and minor discrepancies in the pressures profiles at the end of the pocket. [Similar behaviour has been shown for a rigid parabolic slider by Bertocchi *et al.* [11] even when no discontinuity is present in the gap height, but full-film reformulation still occurs. Since the cavity fraction is discontinuous at the full-film reformulation interface, this suggests that first order discretizations of the Couette term should always be employed when full-film reformulation occurs to avoid oscillations in the solution.]

From these results, it is concluded that even at low pressures between 1 and 10 MPa, small elastic deformations can significantly alter the fluid pressure and cavity fraction profiles. Consequently, results of traditional hydrodynamic simulations with mass-conserving cavitation but no elastic deformation model must be handled with care when making statements about the possible increase of the load carrying capacity due to surface textures. Furthermore, the performed simulations show that the EHL-FBNS algorithm is a useful tool to build up on the considered reference investigations since it can take the additionally required elastic deformation effects into account. Moreover, the implementation of the solver allows to switch conveniently between first and second order discretization schemes of the Couette term" [Hansen et al., 2022].

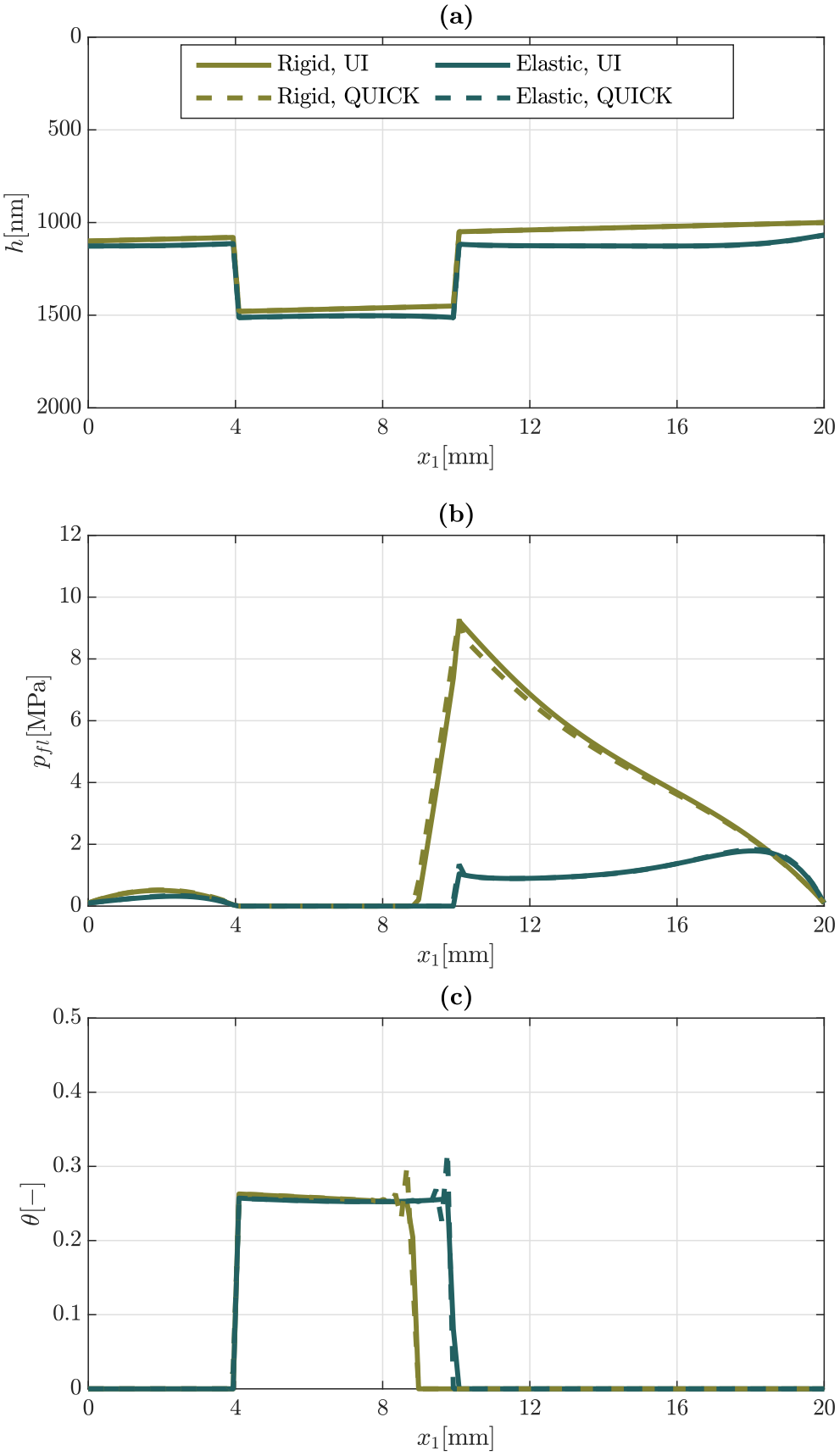

Figure 4.6: "Distribution of gap height h **(a)**, fluid pressure p_{fl} **(b)** and cavity fraction θ **(c)** along the center line of the inclined slider with pocket for rigid, elastic, UI and QUICK simulations." The figure including its caption is adapted from the publication by [Hansen et al., 2022].

4.2 Single Texture in a Ball-on-Disk Tribometer

"[The next] set-up is the ball-on-disk tribometer with a single texture used in the simulations and experiments of Mourier *et al.* [64]. These were performed to investigate the unsteady effect of isolated dimples passing through an EHL contact at pure rolling and rolling-sliding conditions. Mourier *et al.* state that they used shallower dimples in the simulations than in the experiments because the deep dimples compromised convergence. In the following, both geometries are simulated with the EHL-FBNS algorithm to show that the presented algorithm can provide converged results in either case. Firstly, grid convergence studies are performed to identify the preferable discretization scheme. Then, the gap height measurements of Mourier *et al.* are used to validate the EHL-FBNS algorithm for ball-on-disk tribometers. Lastly, differences in the simulated results of Mourier *et al.* and the EHL-FBNS algorithm are discussed and additional deductions about the discretization schemes are drawn.

The rolling-sliding condition of the EHL contact is characterized through the slide-to-roll ratio SSR as provided by Mourier *et al.* [64]:

$$SSR = \frac{U_{low} - U_{up}}{U_{low} + U_{up}}. \tag{4.1}$$

The time dependent variation of the gap height due to the rigid geometry of the surfaces is expressed as [64]:

$$h_{ri}(x_1, x_2, t) = \frac{x_1^2}{2R_{x_1}} + \frac{x_2^2}{2R_{x_1}} + h_{dpl} \cos\left(\frac{\pi}{2} \cdot \frac{D_{dpl}}{1.2 r_{dpl}}\right) \exp\left(-2\left(\frac{D_{dpl}}{1.2 r_{dpl}}\right)^2\right), \tag{4.2}$$

where h_{dpl} is the dimple depth, r_{dpl} is the dimple radius and D_{dpl} is the distance of any position to the moving dimple center [64]:

$$D_{dpl} = \sqrt{(x_1 - x_{1,dpl})^2 + (x_2 - x_{2,dpl})^2}. \tag{4.3}$$

The dimple center has the coordinates $x_{1,dpl}$ and $x_{2,dpl}$ with [64]:

$$x_{1,dpl} = x_{1,0} + t u_{dpl}, \quad x_{2,dpl} = x_{2,0}. \tag{4.4}$$

The initial position of the dimple center is described by $x_{1,0}$ and $x_{2,0}$ at time $t = 0\,\mathrm{s}$. The dimple moves with velocity $u_{dpl} = U_{low}$. The parameters used in the EHL-FBNS simulations are summarized in Table 4.3 [and mimic the contact of a 52 100 steel ball against a silica disk that is lubricated with mineral oil]. All simulations are performed with the same mean velocity u_m, but different SSR and therefore different U_{up}, U_{low} and number of time steps N_t. In the case of $SSR = 0$, $N_t = 257$ time steps and a dimple radius of $r_{dpl} = 15.5\,\mu\mathrm{m}$ are used. To replicate the experiment, a dimple depth of $h_{dpl} = 7\,\mu\mathrm{m}$ is employed, while $h_{dpl} = 0.175\,\mu\mathrm{m}$ is used to be consistent with the numerical set-up of Mourier *et al.* [64]. For $SSR = -0.5$, the dimple radius $r_{dpl} = 21.5\,\mu\mathrm{m}$ is considered. Since the dimple moves more slowly in this case, $N_t = 513$ time steps are required while the time step length Δt stays constant. A dimple depth of $h_{dpl} = 1.3\,\mu\mathrm{m}$ is used for the experiment replication, while $h_{dpl} = 0.16\,\mu\mathrm{m}$ is used to be consistent with the numerical set-up of Mourier *et al.*.

The solution of the first time step at $t = 0\,\mathrm{s}$ is computed with the steady Reynolds equation and the dimple at its starting position to obtain an initial solution for the unsteady Reynolds equation. The cavitation pressure p_{cav} is set to the ambient pressure of $p_{amb} = 0\,\mathrm{Pa}$ and Dirichlet boundary conditions are

used for the fluid pressure. The boundary conditions of θ correspond to zero cavity fraction at the west boundary and zero gradient Neumann condition at all other boundaries. The imposed normal load is $F_{N,imp} = 15$ N and the initial guess of the rigid displacement is set to $h_{d,ini} = -1\,\mu$m. [The rigid body displacement is adjusted in each iteration with the PID controller of Equation (3.20)]. Elastic deformation, Roelands and Dowson-Higginson models are employed to stay consistent with the simulations of Mourier *et al.* [64] who used the FDM multigrid solver of Venner and Lubrecht [89]. As stated by Mourier *et al.*, the accuracy of this solver is of second order in space and time. Due to the Euler implicit discretization of the unsteady term in the EHL-FBNS solver, the achieved accuracy is generally limited to first order for both the UI and the QUICK scheme.

Parameter	Value	Parameter	Value	Parameter	Value
u_m	$0.09\ \mathrm{ms}^{-1}$	μ_0	$2.5 \cdot 10^{-1}$ Pas	N	66049
p_{amb}	0 Pa	α_B	-	N_{x_1}	257
p_{cav}	p_{amb}	α_R	$2.2 \cdot 10^{-8}\ \mathrm{Pa}^{-1}$	N_{x_2}	257
$p_{fl,SB}$	p_{amb}	$p_{0,R}$	$1.96 \cdot 10^8$ Pa	L_{x_1}	$6r_a$
$p_{fl,WB}$	p_{amb}	ρ_0	$850\ \mathrm{kgm}^{-3}$	L_{x_2}	$6r_a$
$p_{fl,EB}$	p_{amb}	C_1	$5.9 \cdot 10^8$ Pa	$h_{d,ini}$	-10^{-6} m
$p_{fl,NB}$	p_{amb}	C_2	1.34	a	$136.5 \cdot 10^{-6}$ m
θ_{SB}	Neumann	E_{up}	-	R_{x_1}	$12.5 \cdot 10^{-3}$ m
θ_{WB}	0	E_{low}	-	Δx_1	$L_{x_1}/(N_{x_1}-1)$
θ_{EB}	Neumann	ν_{up}	-	Δx_2	$L_{x_2}/(N_{x_2}-1)$
θ_{NB}	Neumann	ν_{low}	-	$x_{1,0}$	$-3r_a$
h_{ref}	r_a^2/R_{x_1}	E'	$110 \cdot 10^9$ Pa	$x_{2,0}$	0
$x_{1,ref}$	r_a	$F_{N,imp}$	15 N	u_{dpl}	U_{low}
$x_{2,ref}$	r_a	α_{p^*}	0.05	Δt^*	$\Delta x_1/r_a$
p_{ref}	$385 \cdot 10^6$ Pa	α_θ	0.05	Δt	$\Delta t^* \cdot t_{ref}$
t_{ref}	r_a/u_m	ρ_{ref}	ρ_0	u_{ref}	u_m
$F_{N,ref}$	$F_{N,imp}$	μ_{ref}	μ_0		

Parameter	Value
U_{up}	$0.09\ \mathrm{ms}^{-1}$, $0.135\ \mathrm{ms}^{-1}$
U_{low}	$0.09\ \mathrm{ms}^{-1}$, $0.045\ \mathrm{ms}^{-1}$
SSR	0, -0.5
N_t	257, 513
r_{dpl}	$15.5 \cdot 10^{-6}$ m, $21.5 \cdot 10^{-6}$ m
h_{dpl}	$7000 \cdot 10^{-9}$ m, $175 \cdot 10^{-9}$ m, $1300 \cdot 10^{-9}$ m, $160 \cdot 10^{-9}$ m

Table 4.3: "Summary of the parameters and values used in the EHL-FBNS simulations of the ball-on-disk tribometer with single texture." The table including its caption is adapted from the publication by [Hansen et al., 2022].

In order to perform a grid convergence study, simulations with the UI and QUICK scheme at $SSR = 0$, respectively for the deep and shallow dimple geometries, are employed to assess both schemes with and without gap height discontinuities. For this grid convergence study, the less strict definition $r^n_{EHL-FBNS} = \mathrm{mean}\left(\mathrm{abs}\left(\vec{\delta}^n_{p^*}\right)\right)$ is used instead of Equation (3.23). This is necessary in order to perform the QUICK simulations at low resolutions, otherwise a stall in the convergence of the residual

$r^n_{max,G}$ can occur at some time steps for the used value of the underrelaxation coefficient. Nonetheless, for the highest grid resolution, the stricter residual of Equation (3.23) does not lead to a stall and the maximum deviation in the resulting gap heights along the center line when the dimple is at position $x_{1,dpl} = 0$ is less than 0.1% when compared for both residual definitions. Note also that for any other simulation in this chapter, the stricter definition given by Equation (3.23) (and thus following the suggestion by Woloszynski *et al.* [94]) is employed. The effect of the residual definition on the amount of required iterations for the highest resolution is discussed at the end of this section.

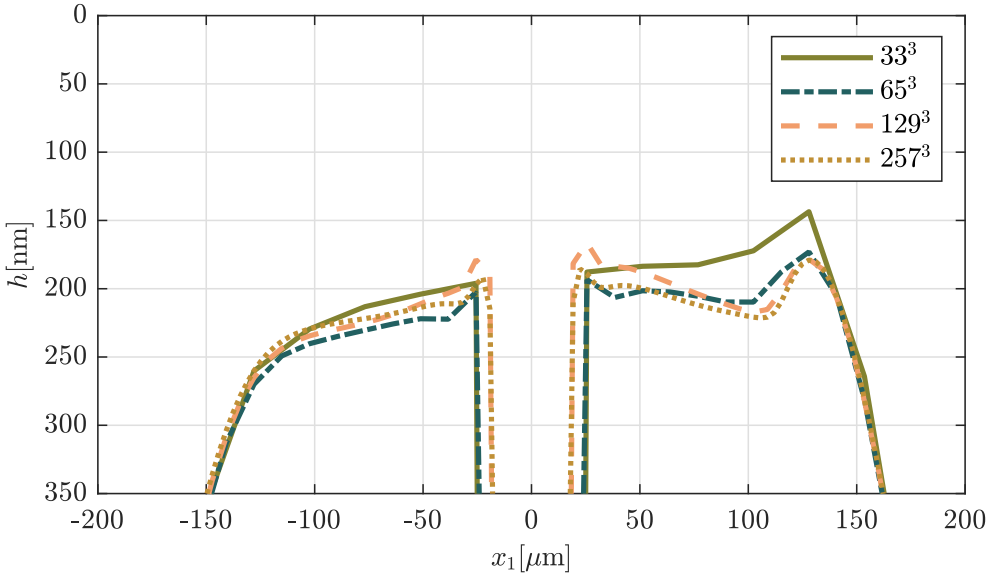

Figure 4.7: "Profiles of gap height h along center line for the deep dimple at position $x_{1,dpl} = 0$, UI discretization scheme and different resolutions of $N_{x_1} \cdot N_{x_2} \cdot N_t$." The figure including its caption was published by [Hansen et al., 2022].

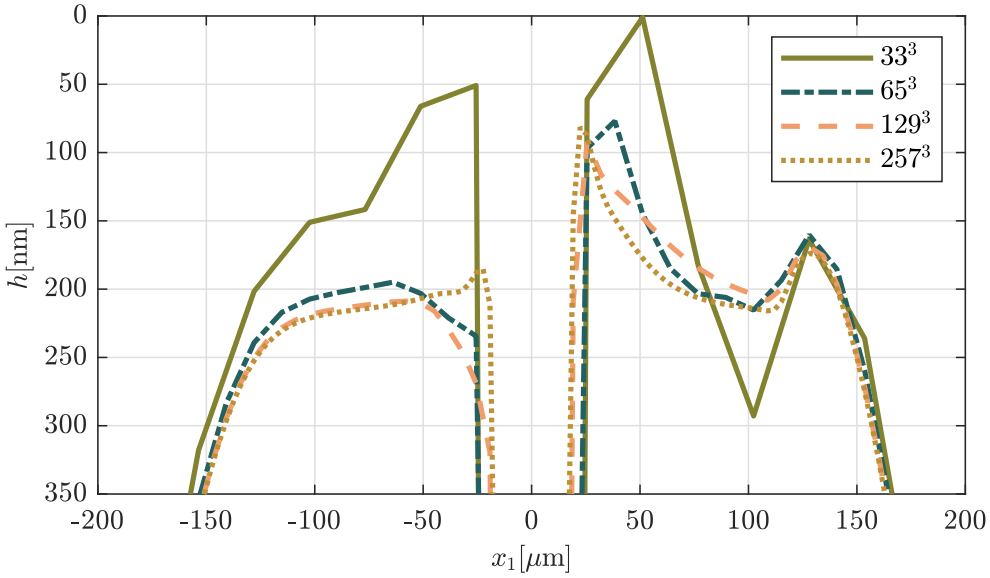

Figure 4.8: "Profiles of gap height h along center line for the deep dimple at position $x_{1,dpl} = 0$, QUICK discretization scheme and different resolutions of $N_{x_1} \cdot N_{x_2} \cdot N_t$." The figure including its caption was published by [Hansen et al., 2022].

For the deep dimple at position $x_{1,dpl} = 0$, the resulting gap height profiles along the center line obtained for different resolutions are displayed in Figure 4.7 for the UI and in Figure 4.8 for the QUICK

scheme. The comparison of both figures shows that the QUICK scheme has a worse convergence behaviour around the dimple than the UI scheme and even converges towards a different solution at the downstream end of the dimple. It is therefore concluded that in this case, the UI scheme with the first order discretization of the Couette term is preferable over the QUICK scheme.

For the shallow dimple at position $x_{1,dpl} = 0$, the resulting gap height profiles along the center line obtained for different resolutions are displayed in Figure 4.9 for the UI and in Figure 4.10 for the QUICK scheme. For this geometry with no discontinuity, both schemes converge towards the same solution, but the second order discretization of the Couette term with the QUICK scheme delivers the better convergence properties and is therefore preferable.

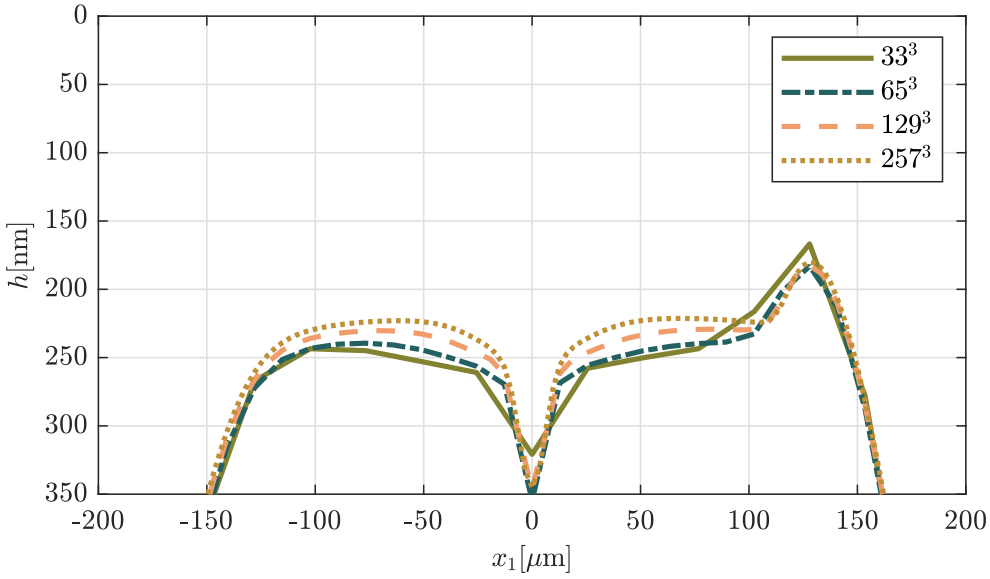

Figure 4.9: "Profiles of gap height h along center line for the shallow dimple at position $x_{1,dpl} = 0$, UI discretization scheme and different resolutions of $N_{x_1} \cdot N_{x_2} \cdot N_t$." The figure including its caption was published by [Hansen et al., 2022].

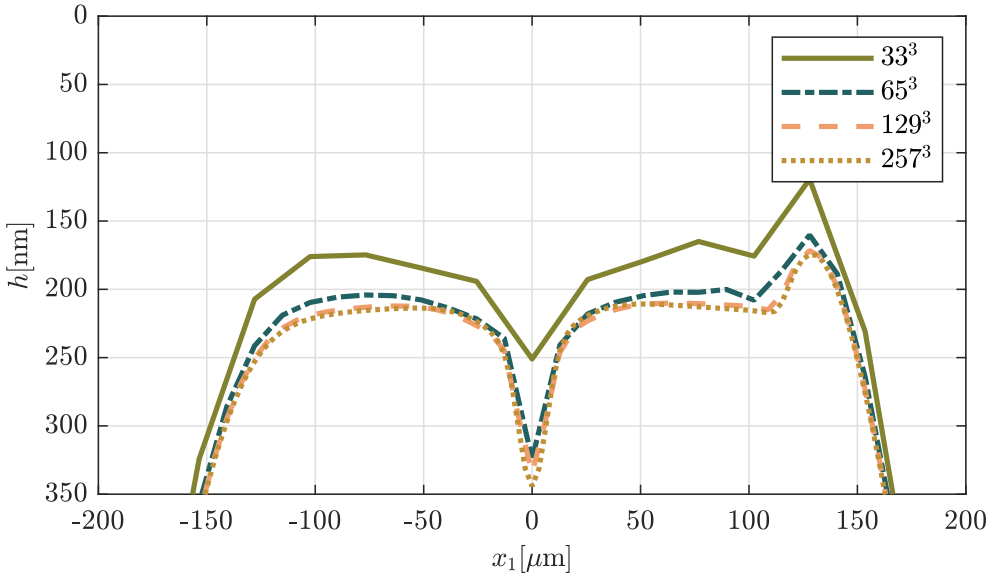

Figure 4.10: "Profiles of gap height h along center line for the shallow dimple at position $x_{1,dpl} = 0$, QUICK discretization scheme and different resolutions of $N_{x_1} \cdot N_{x_2} \cdot N_t$." The figure including its caption was published by [Hansen et al., 2022].

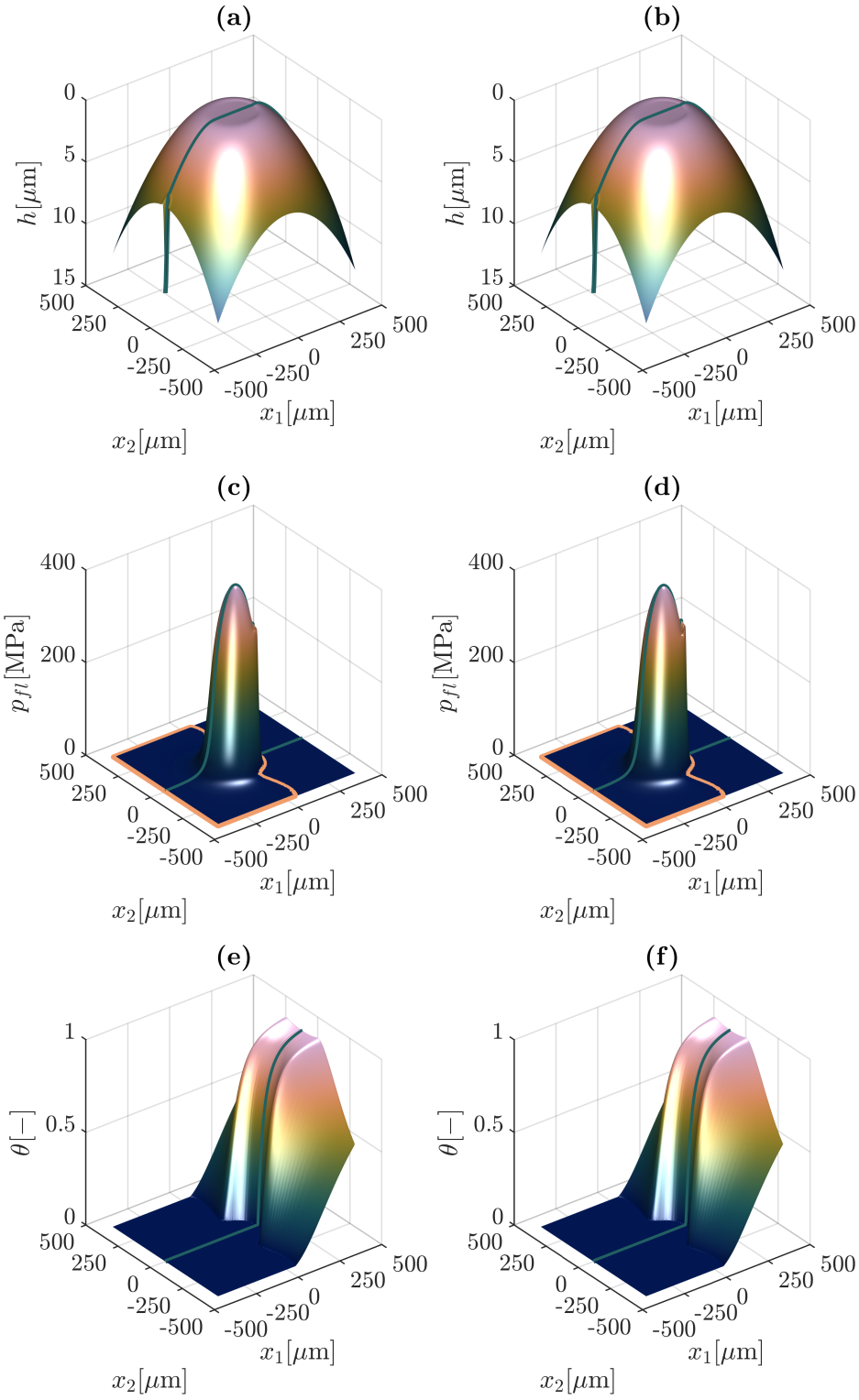

Figure 4.11: "Distribution of gap height h **(a,b)**, fluid pressure p_{fl} **(c,d)** and cavity fraction θ **(e,f)** in the ball-on-disc tribometer with single texture at $t = 0$ s for UI (left) and QUICK (right) discretization." The figure including its caption is adapted from the publication by [Hansen et al., 2022].

The following simulations are performed at the highest resolution level and with the residual definition of Equation (3.23) to further support the previously identified arguments about the preferable discretization scheme of the Couette term [...]. Exemplary results of gap height h, fluid pressure p_{fl} and cavity fraction θ at $t = 0\,\mathrm{s}$, $SSR = 0$ and $h_{dpl} = 7\,\mu\mathrm{m}$ are shown for UI and QUICK simulations in Figure 4.11. The contour line of $p_{fl} = p_{cav}$ is marked in orange while the center line is displayed in green. Apart from more pronounced spikes in the fluid pressure at the downstream end of the EHL contact zone with the more accurate QUICK scheme, both simulations produce almost the same results at first glance.

In the following, the EHL-FBNS results are compared to the experimental and simulated counterparts of Mourier *et al.* [64]. The data of Mourier *et al.* was read in with the software Engauge Digitizer and can therefore be subject to minor deviation from the original data. The data of Mourier *et al.* consists of gap height measurements in the experimental case and of gap height and pressure distributions in the simulated case at five distinctive dimple center positions.

Figure 4.12 **(a)** shows the UI and QUICK results of the EHL-FBNS algorithm along with the experimental results of Mourier *et al.* in case of the deep dimple with $SSR = 0$. Due to the large depth of the dimple in comparison to the remaining gap height within the EHL contact, the gap height distribution shows a strong discontinuity at the rim of the deep dimple. At the first and last dimple position, the dimple is just entering or leaving the visualized domain. Most of the domain is still unaffected by the dimple and basically corresponds to the steady solution without a dimple. Small differences in the gap height h between UI and QUICK can be observed while the more accurate QUICK scheme closely fits the experimental results in the center of the domain. The systematic difference in the gap height between UI and QUICK is mostly due to a different value of the rigid body displacement h_d which is set such that the load balance equation is eventually met. For the dimple positions 2-4, the QUICK scheme produces large deviations in the gap height compared to the experimental results at the discontinuity at the downstream rim of the dimple. There, the UI scheme manages to fit the experimentally measured gap height better. These results are consistent with the finding of LeVeque [57, Ch. 11] that for discontinuous problems, first order methods give smoother results while second order methods cause oscillations. Both schemes deviate from the experimental results at the downstream rim of the dimple when it is leaving the EHL contact at position 5. At all five positions, the fluid pressure distributions of UI and QUICK are mostly in close agreement, but the UI scheme produces higher pressure spikes at the downstream rim of the dimple which in turn cause larger elastic deformations. This explains why the UI scheme shows better agreement in the gap height since this more diffusive scheme eventually tends to smooth the discontinuity at the rim of the dimple by adjusting the fluid pressure accordingly. Consequently, the lower order UI scheme is recommendable close to discontinuities in the gap height while the QUICK scheme is more advantageous at smoother parts of the geometry.

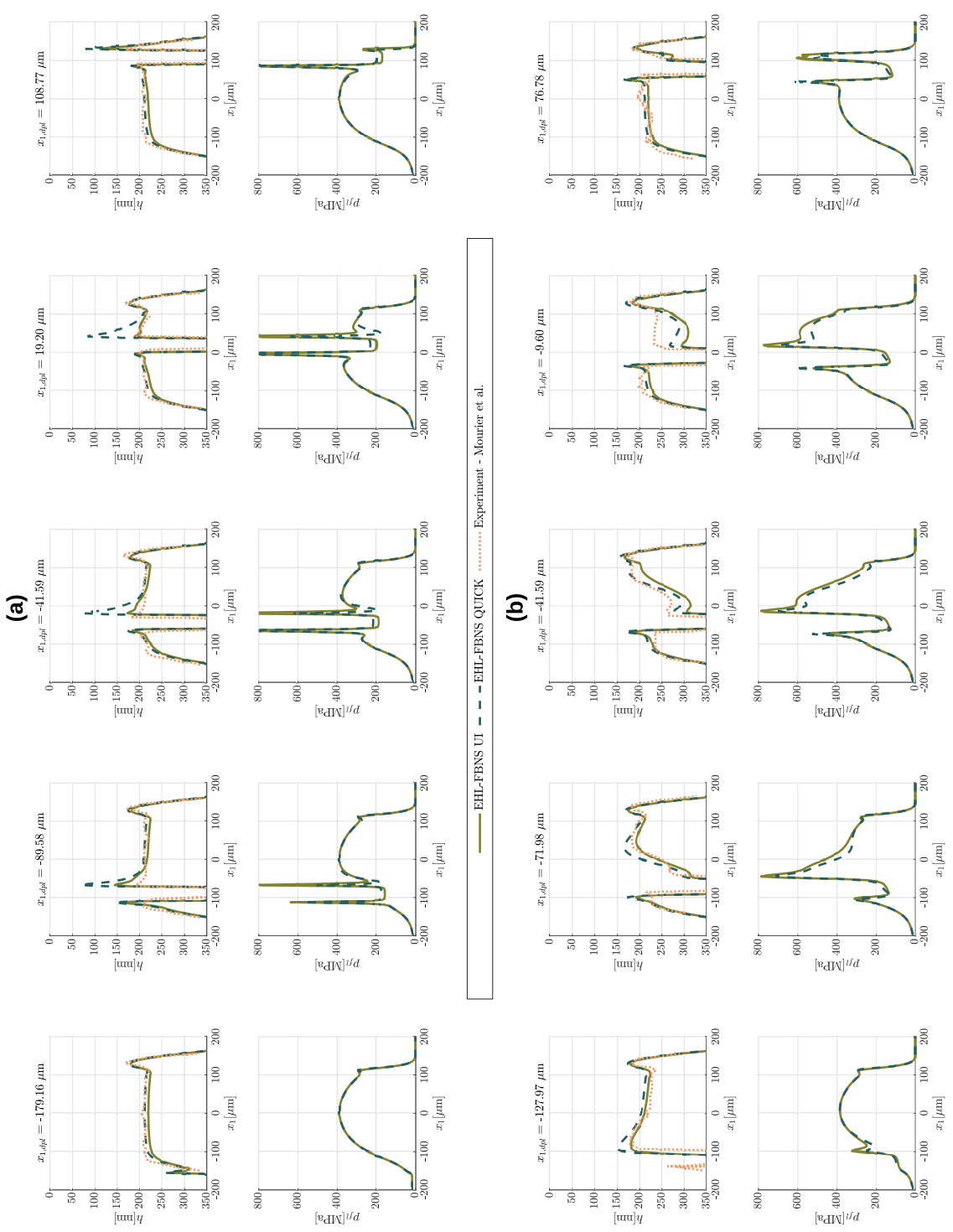

Figure 4.12: "At $SSR = 0$ **(a)** and $SSR = -0.5$ **(b)**: distribution of gap height h (top) and fluid pressure p_{fl} (bottom) along the center line of the ball-on-disc tribometer with single texture for UI and QUICK discretization against the experimental results of Mourier *et al.* [64]." The figure including its caption is adapted from the publication by [Hansen et al., 2022].

The UI and QUICK results along with experimental values of Mourier *et al.* in case of the deep dimple with $SSR = -0.5$ are depicted in Figure 4.12 **(b)**. In this case, the downstream area of the dimple also gets deformed because the dimple moves at a lower speed than the mean velocity u_m. This means that some of the fluid that is initially within the dimple leaves the texture behind which causes a deformation since more volume is occupied outside of the dimple. This behaviour is principally also replicated by the EHL-FBNS results but in a more pronounced way than in the experiments. The higher order QUICK scheme matches the experimental results closer than the UI scheme in the vicinity of this effect as depicted at dimple position 3. The UI scheme causes higher fluid pressures downstream of the dimple which this time cause a larger overestimation of the occurring deformation than done by the QUICK scheme. However, the stronger this effects becomes, the larger the deviation between experiment and simulation becomes as shown at dimple position 4. Still, experimental and EHL-FBNS results generally show a good agreement in the gap height distribution. The EHL-FBNS algorithm is thereby validated for simulations of discontinuous textures in ball-on-disc tribometers under EHL operating conditions.

Next, the EHL-FBNS results are compared to the simulated results of Mourier *et al.* [64]. Figure 4.13 **(a)** shows the UI and QUICK results of the EHL-FBNS algorithm along with the simulated results of Mourier *et al.* in case of the shallow dimple with $SSR = 0$. Unlike the deep dimple, the rim of the shallow dimple is only weakly discontinuous. At the first dimple position, the simulated results of Mourier *et al.* agree well with the gap height and fluid pressure produced by the QUICK scheme. This is expected because both eventually correspond to second order spatial discretizations of an almost steady case since the shallow dimple does not affect the displayed domain yet. Similar to the deep dimple case, the first order UI scheme results in practically the same fluid pressure distribution as the QUICK scheme but a slightly different systematic offset in the gap height distribution. When the shallow dimple introduces unsteady effects at positions 2-5, the gap height distributions of QUICK stay closer to the results of Mourier *et al.* than in the case of UI discretization. Nonetheless, all three methods deliver different gap heights close to the dimple. While the fluid pressure distributions of UI and QUICK show similar oscillations around the dimple, it stays almost undisturbed in the simulations of Mourier *et al.*. Since differently to the deep dimple, the results of UI and QUICK are still reasonably close to each other at the rim of the shallow dimple, errors or oscillations caused by the discretization scheme of the Couette term are not believed to be of dominant role. Instead, the differences in the results of EHL-FBNS algorithm and Mourier *et al.* during the introduction of unsteady phenomena are likely caused by the first order Euler implicit discretization of the EHL-FBNS algorithm while Mourier *et al.* use a second order discretization in time.

These findings are complemented by the results in case of the shallow dimple at $SSR = -0.5$ as depicted in Figure 4.13 **(b)** along with the outcome of the simulations of Mourier *et al.*. Gap height and fluid pressure of QUICK and Mourier *et al.* are in close agreement while the lower order UI results slightly differ at some points. The reason for the closer agreement of the EHL-FBNS results with Mourier *et al.* is expected to be due the dimple moving at a lower speed, thus introducing slower unsteady effects. Since the discrete time steps are of the same length as in the case of $SSR = 0$, the time resolution is relatively higher for $SSR = -0.5$, thus enabling all schemes to deliver almost the same results.

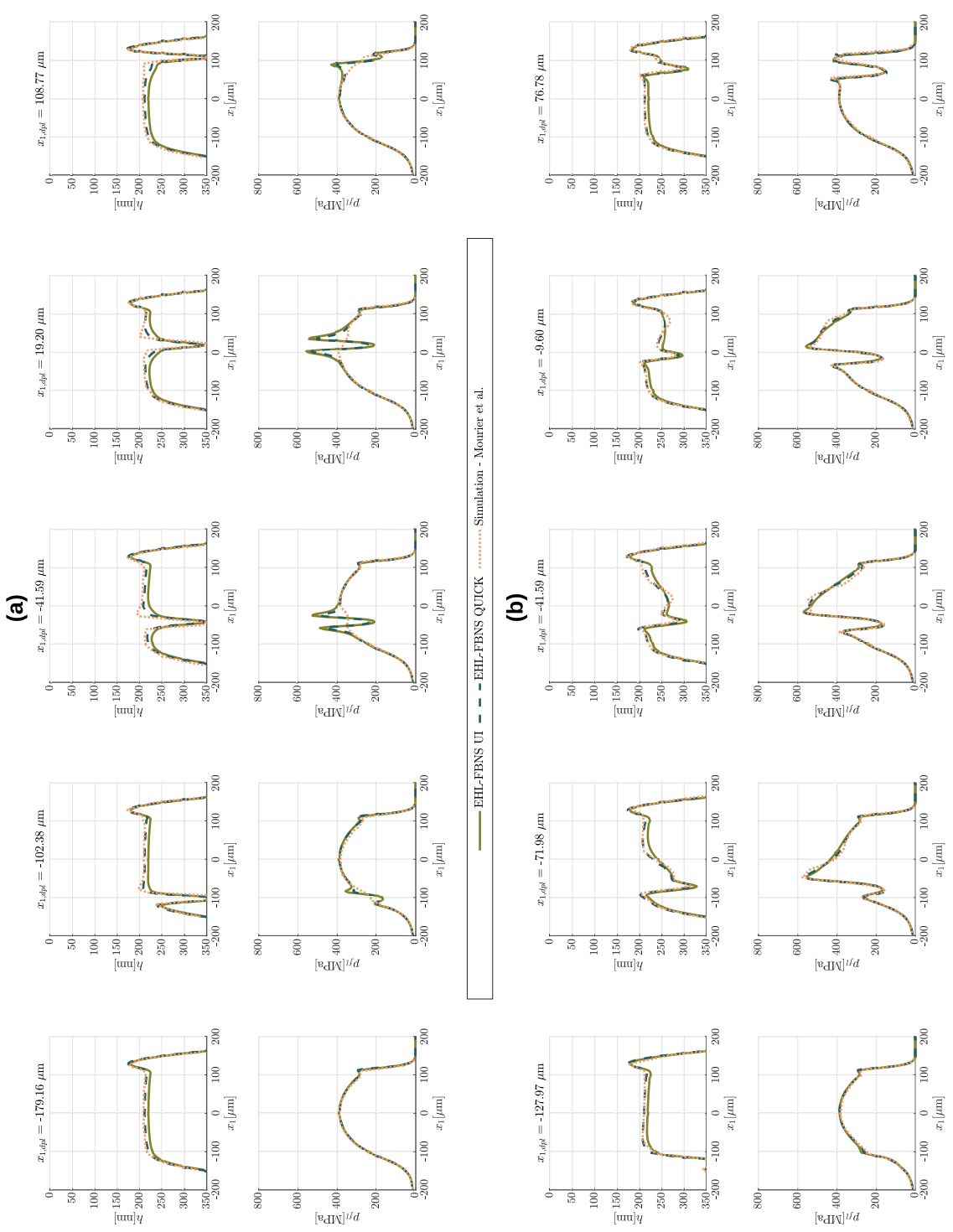

Figure 4.13: "At $SSR = 0$ **(a)** and $SSR = -0.5$ **(b)**: distribution of gap height h (top) and fluid pressure p_{fl} (bottom) along the center line of the ball-on-disc tribometer with single texture for UI and QUICK discretization against the simulated results of Mourier *et al.* [64]." The figure including its caption is adapted from the publication by [Hansen et al., 2022].

Summarizing, the EHL-FBNS algorithm manages to deliver converged results even in unsteady EHL operating conditions with deep dimples with strong discontinuities at their rim. Moreover, the first order UI scheme gives closer agreement to the experimental results of Mourier *et al.* [64] in the vicinity of deep dimples than the higher order QUICK scheme. Therefore, lower order spatial discretization schemes are recommended close to strong gap height discontinuities while higher order schemes are recommended at smoother parts of the geometry due to their higher accuracy in these areas. Moreover, the extreme pressure spikes at the rim of the deep dimples raise the question whether the elastic half-space assumption is still valid in this area. Nonetheless, the good agreement of the gap height distribution with the experimental data of Mourier *et al.* validates the EHL-FBNS algorithm for simulations of textures in ball-on-disc tribometers under unsteady EHL operating conditions." [Hansen et al., 2022].

4.3 Conclusion

"The EHL-FBNS algorithm was presented in this [...chapter]. It allows the simulation of the unsteady fluid pressure build up under consideration of mass-conserving cavitation with the JFO model within lubrication gaps. Furthermore, its versatile implementation enables the simulation of various combinations of isoviscous or piezoviscous flows, incompressible or compressible liquid phases, rigid or elastic surfaces, first or second order spatial discretizations of the Couette term, imposed rigid body displacements or normal forces and Dirichlet or Neumann boundary conditions [...]. The EHL-FBNS algorithm results were compared to analytical, simulated and experimental literature data of [...] Fowell *et al.* [33], Bertocchi *et al.* [11] and Mourier *et al.* [64]. The key findings are [...]:

- the EHL-FBNS code can deliver converged results even when extreme gap height discontinuities are present.
- Higher order spatial discretizations of the Couette term can cause large errors in the gap height distributions when gap height discontinuities are present in the EHL contact. Therefore, lower order spatial discretization schemes are recommended close to strong gap height discontinuities while higher order schemes are recommended at smoother parts of the geometry due to their higher accuracy in these regions [...].
- [Even in the case of smooth geometries, first order discretizations of the Couette term seem to be advisable when full-film reformulation occurs to avoid oscillations in the cavity fraction.]
- The EHL-FBNS algorithm is validated for the investigation of deep dimples with discontinuous rims in ball-on-disc tribometers under EHL operating conditions.
- Even at traditional purely hydrodynamic operating conditions with low fluid pressures between 1 and $10\ \mathrm{MPa}$, the employment of elastic models is recommended because the resulting pressure profiles are strongly influenced by slight elastic deformations" [Hansen et al., 2022].

5 Pin-on-Disk Tribometer

This chapter is based on the publication *Establishment and Calibration of a Digital Twin to Replicate the Friction Behaviour of a Pin-on-Disk Tribometer* by [Hansen et al., 2023]. It is furthermore emphasized that the associated Stribeck curves of the real-life experiments were acquired by the co-author Gerda Vaitkunaite at IAM-ZM. Thus, their acquisition is not part of this thesis and is only briefly described in this dissertation. The findings of the cited publication are essential to the present thesis because the developed digital twin will be used to study textured surfaces in the following chapter.

"The design [of the associated textures] usually needs to be tailored to the specific conditions within the tribological contact to exploit their full potential [61, 36]. These conditions can be most clearly defined and controlled in tribometers, where different kinds of tribometers represent specific tribological contacts that occur in certain applications. Ball-on-disk tribometers are, for example, used to represent the non-conformal contacts of ball bearings while pin-on-disk tribometers are used to mimic the conformal contacts of journal bearings. The similarity of the tribological contact eventually allows to transfer the fundamental insights obtained in tribometers to applications.

Due to the highly controlled operating conditions and reduction to the tribological contact, tribometers are easier to simulate with a numerical model than their corresponding applications. Nonetheless, even under these simplified circumstances, the modelling of the tribological contact is not straightforward and consistent results from simulations and experiments are challenging to obtain [Hansen et al., 2020]. Despite these difficulties, the potential of a joint experimental and numerical research strategy is significant because it allows to obtain complementary in- and ex-situ data. Furthermore, the simulations can be used to perform cheap and quick a priori investigations to identify the relevant parameter ranges for the experiment. The obtained simulation results can then be confirmed by selectively chosen experiments [19]. [Lastly, ...] the experiment results give validation and new impulses for the adjustment of the simulation model and parameters [...].

The above described interaction between the experiment and simulation generally corresponds to the concept of a digital twin [35]. While some works strictly require a digital twin to have bi-directional real-time communication between the physical and virtual entity [80], other works already consider a one-directional physical-to-virtual connection as sufficient to be labelled as a digital twin [50]. The latter case also applies to this work, in which a digital twin of a pin-on-disk tribometer is established and calibrated in several steps. First, the physical entity of the pin-on-disk tribometer is described along with the associated [...] testing procedure and topography measurements. Subsequently, the macro- and microscopic reconstruction of the virtual geometry from the real-life post-test topographies is presented [...]. Afterwards, [...] virtual calibration steps are performed to obtain a representative virtual geometry for an arbitrary specimen pairing. At the same time, the calibration results are used to identify the macro- and microscopic sensitivities of the digital twin. Moreover, the Hersey number is derived for a pin-on-disk tribometer to allow for the validation of the digital twin with the Stribeck curves of its real-life counterpart and the generalization to operating conditions at different dynamic viscosities" [Hansen et al., 2023].

5.1 Real-life Experiment

The real-life pin-on-disk experiment procedure consists of two steps that are visualized in Figure 5.1 [Hansen et al., 2023]. The experiments employ disks with a diameter of $80\,\mathrm{mm}$ and pins with a diameter of $D = 8\,\mathrm{mm}$ as specimen. The pins are attached to a holder such that they protrude out of the holder with a pin height of $1\,\mathrm{mm}$. Both being made out of 100Cr6 bearing steel, the disk's hardness is 800 HV and pin's hardness is 713 HV.

As a first step, the pin is levelled against the non-rotating disk at an imposed normal load of $F_{N,imp} = 50\,\mathrm{N}$ [Hansen et al., 2023]. This is done by lifting the pin holder with $5\,\mathrm{mL}$ of pressurized oil that is supplied through the channel underneath in the base plate. This causes the holder with the attached pin to align against the disk according to the contact pressure distribution within the tribological contact. When the pressurized oil flow eventually subsides, the pin holder settles again in the base plate and the obtained alignment is considered to be fixed.

Subsequently, the normal load is raised to $F_{N,imp} = 150\,\mathrm{N}$ and a constant oil flow of $5\,\mathrm{mL\,min^{-1}}$ is supplied through the channel in front of the pin [Hansen et al., 2023]. The upper disk is put into rotation which draws the lubricant into the tribological contact. The friction coefficient is measured as described in Section 2.1 for five ramps consisting of distinctive sliding velocities U between 0.04 and $2\,\mathrm{m\,s^{-1}}$. Each velocity is kept constant for $5\,\mathrm{min}$ to acquire the friction data. In order to avoid influences of running-in, only the last three of the five ramps are averaged to determine the final Stribeck curve of each test.

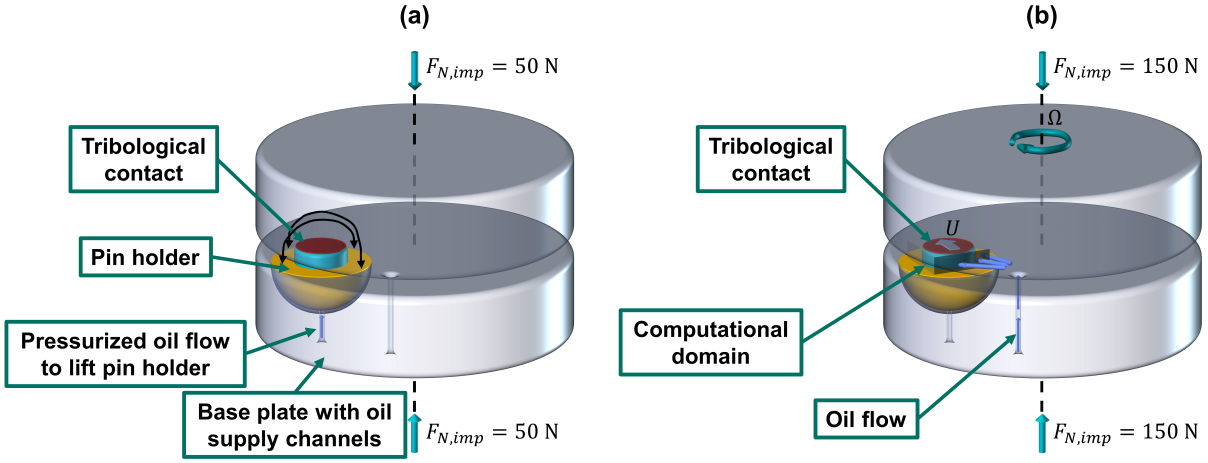

Figure 5.1: "Schematic depiction of (a) pin levelling process and (b) Stribeck curve acquisition in the pin-on-disk tribometer." The figure including its caption was published by [Hansen et al., 2023].

Every test is performed with an additive-free mineral base oil [Hansen et al., 2023]. For each of the two investigated oil temperatures, three tests are repeated and consolidated into one set. Each of the respective tests is performed with new pin-on-disk specimen pairings and fresh oil. The selected oil temperatures are 24 and $50\,^{\circ}\mathrm{C}$ and result in dynamic viscosities μ_0 of 0.066 and $0.024\,\mathrm{Pa\,s}$. The design of experiments is summarized in Table 5.1.

Set	Test	Temperature (°C)	Dynamic viscosity μ_0 [Pas]
1	1.1	24	0.066
	1.2		
	1.3		
2	2.1	50	0.024
	2.2		
	2.3		

Table 5.1: "Design of experiments." The table including its caption was published by [Hansen et al., 2023].

"In order to quantify the deviation of the Stribeck curves from a reference Stribeck curve $C_{f,ref}$ in relation to the overall magnitude of the [theoretical] boundary friction coefficient $C_{f,b} = 1/(3\sqrt{3})$, the deviation of the friction coefficient is defined as:

$$C_{f,dev} = \frac{C_f - C_{f,ref}}{C_{f,b}}. \tag{5.1}$$

The Stribeck curves of the three tests in set 1 at $24\,^{\circ}\mathrm{C}$ along with their set average are depicted in Figure 5.2a. The area enclosed by the maximum and minimum friction coefficients at each relative velocity is shaded in grey to visualise the set scatter. The corresponding deviation of the friction coefficient is shown in Figure 5.2b, where the averaged Stribeck curve of the set is used as reference $C_{f,ref}$. The analogous results of set 2 at $50\,^{\circ}\mathrm{C}$ are represented in Figure 5.3 and demonstrate that the largest deviation in the friction coefficient in the experiments is approximately $C_{f,dev,exp} \approx \pm 10\%$ and occurs in the mixed lubrication regime" [Hansen et al., 2023].

Once the experiments are conducted, the specimens are cleaned with isopropanol in an ultrasonic bath [Hansen et al., 2023]. Afterwards, the macroscopic topographies of the pin and a patch within the contact line on the disk are measured with the confocal microscope FRT. The resulting topographies cover an area of $8\,\mathrm{mm} \times 8\,\mathrm{mm}$ at a resolution of 500×500 pixel. Additionally, microscopic topographies of roughness patches on the pin and the disk are measured with the white light interferometry profiler Sensofar. They have a size of $84.9\,\mu\mathrm{m} \times 63.7\,\mu\mathrm{m}$ at a resolution of 768×576 pixel.

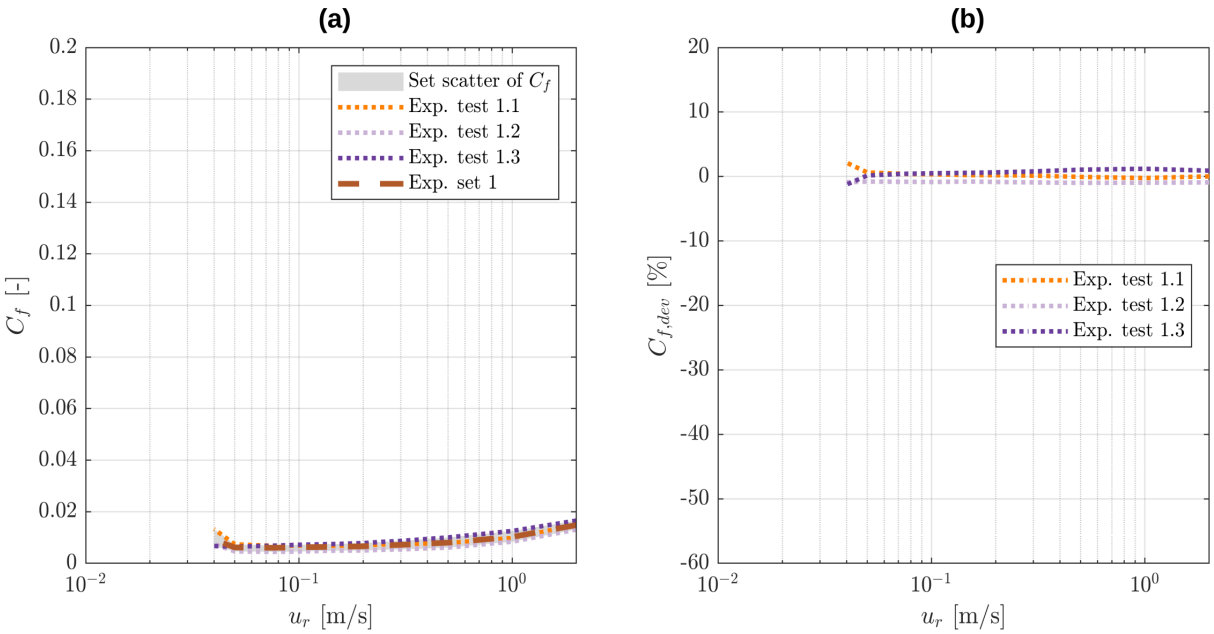

Figure 5.2: "Experimental results of the tests in set 1 and their set average. (a) Friction coefficient C_f as a function of relative velocity u_r. (b) Deviation of the friction coefficient $C_{f,dev}$ as a function of relative velocity u_r." The figure including its caption was published by [Hansen et al., 2023].

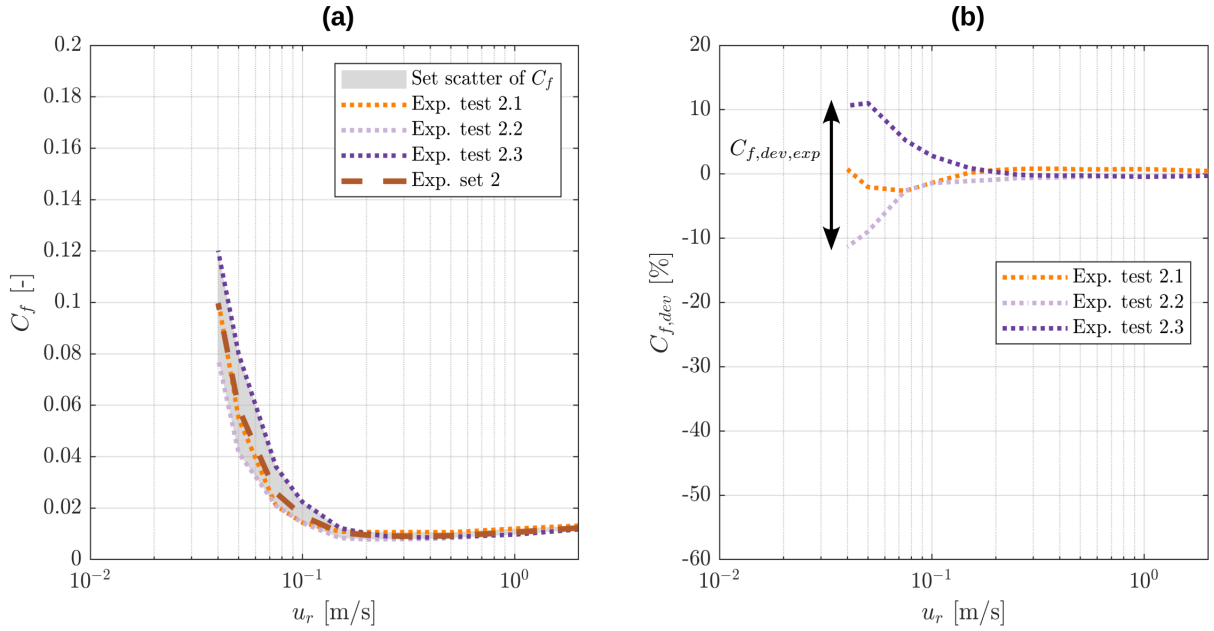

Figure 5.3: "Experimental results of the tests in set 2 and their set average. (a) Friction coefficient C_f as a function of relative velocity u_r. (b) Deviation of the friction coefficient $C_{f,dev}$ as a function of relative velocity u_r." The figure including its caption was published by [Hansen et al., 2023].

5.2 Virtual Geometry Reconstruction

"The macro- and microscopic post-test topographies are first processed with the software Gwyddion© to correct the measurement defects through interpolation with the Laplace equation, rotate the topography towards its mean plane as an initial levelling guess, set the zero-height mark to the mean plane and limit the height range to $20\,\mu\mathrm{m}$. In case of the macroscopic pin topography, the points belonging to the area surrounding the pin are excluded in the computation of the mean plane. Furthermore, a Gaussian filter is applied to both the macroscopic pin and disk topographies to remove roughness information and measurement noise by smoothing the profiles. The size of the Gaussian filter is parameterized by its full width at half maximum of the Gaussian distribution. The microscopic roughness topographies, on the other hand, do not require any filtering since their measured profiles are sufficiently smooth due to the higher resolution. The remaining processing is performed with MATLAB©. On both the macro- and microscopic scale, the disk topography is flipped above the pin and the topographies are aligned such that the x_1-axis points in the same direction as the velocity of the disk U. In the case of the macroscopic topographies, the origin of the coordinate system is also aligned with the center of the pin. For the macroscopic pin, the pin height of $1\,\mathrm{mm}$ is set relative to its zero-height mark. Since any profile variations in the disk and the pin holder are assumed to be negligible in comparison to the overall pin height, the profiles of the disk and the pin holder around the pin are set to be perfectly smooth. Lastly, the resolution of the macroscopic profiles is adjusted by interpolation. For the roughness topographies, a subdomain of 256×256 pixel is extracted without interpolation from the original topography. The effect of the filtering on the resulting macroscopic virtual geometry of test 2.1 is depicted in Figure 5.4 for an exemplary rigid body displacement of $10\,\mu\mathrm{m}$ and resolutions of 500×500 pixel, where unfiltered topographies are used in (a) and a 9 pixel Gaussian filter is used in (b).

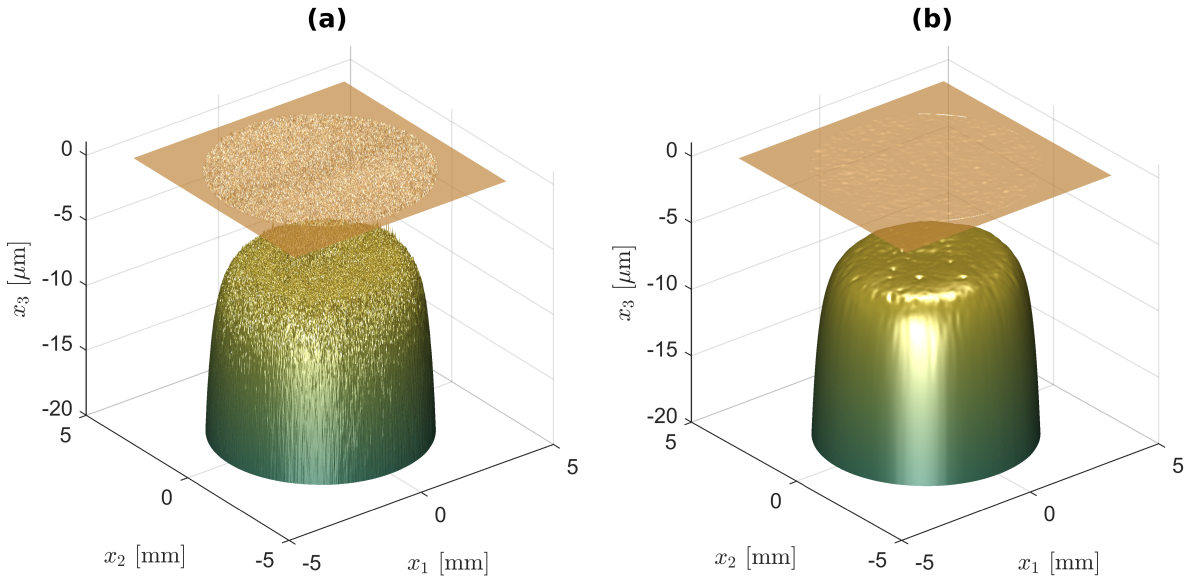

Figure 5.4: "Exemplary virtual macroscopic geometry of test 2.1, where the disk is represented by the top surface and the pin by the bottom surface. Note the different scale of the vertical and the horizontal axes. Below the shown x_3 range, the pin holder profile is modelled as a flat surface at $x_3 = -1\,\mathrm{mm}$: (a) without filtering; and (b) after applying a 9 pixel Gaussian filter." The figure including its caption was published by [Hansen et al., 2023].

In order to simulate the alignment of the pin against the disk at an imposed normal load of $F_{N,imp} = 50\,\mathrm{N}$ [...], a dry contact solver for non-periodic problems is coupled with the torque balance equation. The dry contact solver is based on the CG-FFT algorithm described by Polonsky and Keer [71] and Sainsot and Lubrecht [75]. During inner iterations, the code computes the equilibrium of elastic deformation and dry contact pressure for an imposed normal load while using linear convolutions with the kernel function derived from the elastic half-space theory when constant pressure over rectangular discretisation cells is assumed [49, Ch. 3.3], [65]. Young's modulus E and the Poisson ratio ν of the upper and lower surfaces are considered in the kernel function. Within the contact region, the dry contact pressure can take values between zero as a lower limit and the hardness Hrd of the material as a maximum limit [90]. Outside of the contact zone, the pressure is set to zero. Once the dry contact solver delivers a converged dry contact pressure field $p_{con,dry}(x_1, x_2)$, this field is used in outer iterations to evaluate the resulting torques Trq_{x_1} and Trq_{x_2} around the x_1- and x_2-axes by summing up over all of the $N_{x_1} N_{x_2}$ grid points of size $\Delta x_1 \Delta x_2$:

$$Trq_{x_1} = \sum_{N_{x_1}} \sum_{N_{x_2}} -x_2 p_{con,dry} \Delta x_1 \Delta x_2, \tag{5.2}$$

$$Trq_{x_2} = \sum_{N_{x_1}} \sum_{N_{x_2}} x_1 p_{con,dry} \Delta x_1 \Delta x_2. \tag{5.3}$$

The dimensionless residuals of the torque balances are computed at each outer iteration n as:

$$r^n_{x_1} = \frac{Trq^n_{x_1}}{\sum\limits_{N_{x_1}} \sum\limits_{N_{x_2}} \mathrm{abs}\left((-x_2) p^n_{con,dry} \Delta x_1 \Delta x_2\right)}, \tag{5.4}$$

$$r^n_{x_2} = \frac{Trq^n_{x_2}}{\sum\limits_{N_{x_1}} \sum\limits_{N_{x_2}} \mathrm{abs}\left(x_1 p^n_{con,dry} \Delta x_1 \Delta x_2\right)}. \tag{5.5}$$

As long as these residuals are larger than a prescribed tolerance of 10^{-6}, the angles α_{x_1} and α_{x_2} are adjusted by a PID controller with its coefficients K_P, K_I and K_D:

$$\alpha_{x_1} = \left(K_P r^n_{x_1} + K_I \sum_i^n r^i_{x_1} + K_D \left(r^n_{x_1} - r^{n-1}_{x_1} \right) \right) \cdot 360^\circ, \tag{5.6}$$

$$\alpha_{x_2} = \left(K_P r^n_{x_2} + K_I \sum_i^n r^i_{x_2} + K_D \left(r^n_{x_2} - r^{n-1}_{x_2} \right) \right) \cdot 360^\circ. \tag{5.7}$$

Afterwards, the new pin profile $x_{3,low}$ is computed by altering the unlevelled pin profile $x_{3,low,0}$ and the loop is repeated:

$$x_{3,low} = x_{3,low,0} + x_2 \tan(\alpha_{x_1}) - x_1 \tan(\alpha_{x_2}). \tag{5.8}$$

Note, however, that $x_{3,low} = -1\,\mathrm{mm}$ is enforced for the area around the pin because there, the levelling is assumed to be negligible in comparison to the pin height. The described levelling process is performed for each of the virtual macroscopic gap geometries. The employed values of the solver parameters are summarised in Table 5.2.

Parameter	Value
$F_{N,imp}$	50 N
ν_{up}	0.3
ν_{low}	0.3
E_{up}	$210 \cdot 10^9$ Pa
E_{low}	$210 \cdot 10^9$ Pa
Hrd	$6.99 \cdot 10^9$ Pa
K_P	$3 \cdot 10^{-6}$
K_I	$6 \cdot 10^{-6}$
K_D	$3.75 \cdot 10^{-7}$

Table 5.2: "Employed parameter values of the pin levelling solvers." The table including its caption was published by [Hansen et al., 2023].

Before the profiles are averaged, the mean plane of each levelled pin profile within a radius of $3\,\mathrm{mm}$ from its center is used to define its new zero-height mark. This is important to reduce the effect of the pin rim on the mean plane which could otherwise distort the following averaging by over-weighting certain pin topographies. For the disks, the zero-height mark remains unchanged. Once this is done for all of the tests within a set, the geometries are interpolated on a new grid on which the set average is determined for pin and disk. Below a truncation height of $-20\,\mu\mathrm{m}$, the pin height of $-1\,\mathrm{mm}$ is enforced again. Finally, the obtained averaged geometry is levelled again. The centre lines of the resulting virtual macroscopic pin topographies of set 2 in the exemplary case of perfectly smooth macroscopic disk topographies as counter bodies are displayed in Figure 5.5 [...].

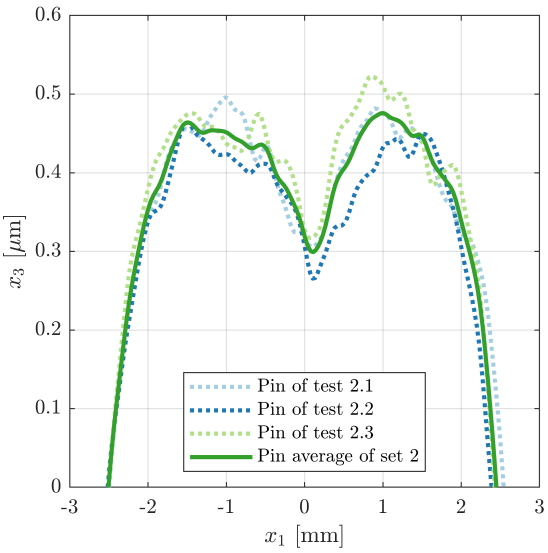

Figure 5.5: "Center line plot of the virtual macroscopic pin topographies of tests 2.1, 2.2, 2.3 and the average of set 2. Note the different scale of the vertical axis. The topographies are previously filtered with a 9 pixel Gaussian filter and the resolution is adjusted to 256×256. The levelling is performed for perfectly smooth macroscopic disk counter bodies." The figure including its caption was published by [Hansen et al., 2023].

The microscopic geometries are used to compute the mean contact pressures, mean gap heights and homogenization factors [according to Section 3.2.1 ...]. Once these factors are computed for several different roughness patches of a single post-test pin and disk specimen combination, the test average is computed. The results of six different pin and disk patches of test 2.1 and their average are displayed for the mean gap height $\overline{h}$ in Figure 5.6a, the mean contact pressure $\overline{p}_{con}$ in Figure 5.6b and the homogenization factor A_{11} in Figure 5.7a. The averages of the homogenization factors A and $\vec{b}$ over the six patches are depicted in Figure 5.7b. The root-mean-square values of the roughness topography of each patch are provided in Table 5.3. [Averaging them results in a root-mean-square of the roughness of $S_q = 145.7\,\mathrm{nm}$.] The reconstructed microscopic virtual geometry of patch 4 of test 2.1 is exemplary shown in Figure 5.8 for a rigid body displacement of $1\,\mu\mathrm{m}$" [Hansen et al., 2023].

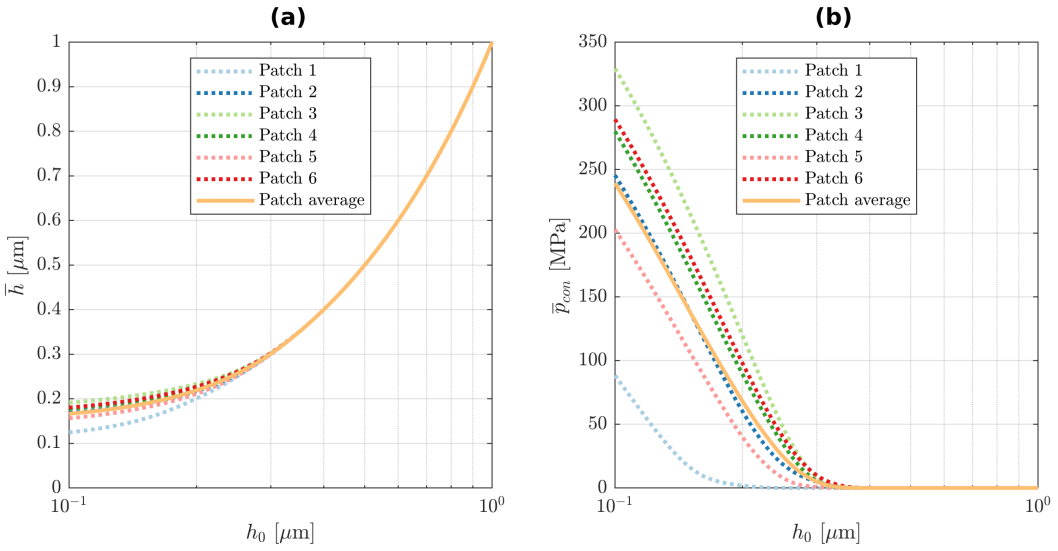

Figure 5.6: "(a) Mean gap height $\overline{h}$ and (b) mean contact pressure $\overline{p}_{con}$ as a function of rigid body displacement h_0 for different roughness patches and their average." The figure including its caption is adapted from the publication by [Hansen et al., 2023].

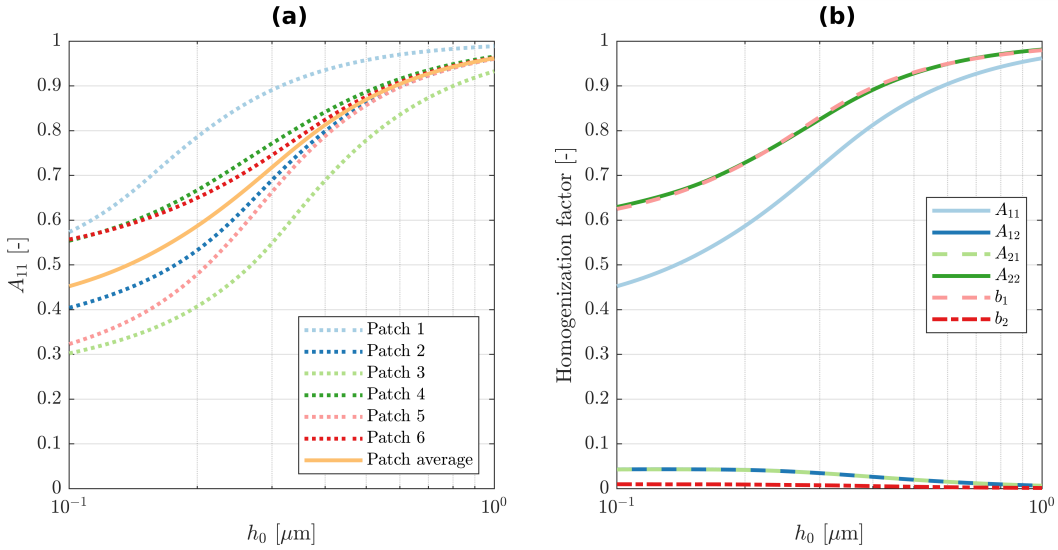

Figure 5.7: "(a) Homogenization factor A_{11} as a function of rigid body displacement h_0 for different roughness patches of test 2.1 and their average. (b) Averages of the homogenization factors A and $\vec{b}$ over test 2.1 as a function of rigid body displacement h_0." The figure including its caption was published by [Hansen et al., 2023].

Patch	$S_{q,up}$	$S_{q,low}$	$S_q = \sqrt{S_{q,up}^2 + S_{q,low}^2}$
1	84.5 nm	41.5 nm	94.1 nm
2	84.6 nm	116.5 nm	144.0 nm
3	118.3 nm	132.3 nm	177.5 nm
4	119.9 nm	101.4 nm	157.0 nm
5	96.3 nm	96.7 nm	136.4 nm
6	100.1 nm	131.2 nm	165.0 nm

Table 5.3: "Root-mean-square values S_q of the roughness patches of test 2.1, where the zero-height mark of each surface is at its respective mean plane." The table including its caption was published by [Hansen et al., 2023].

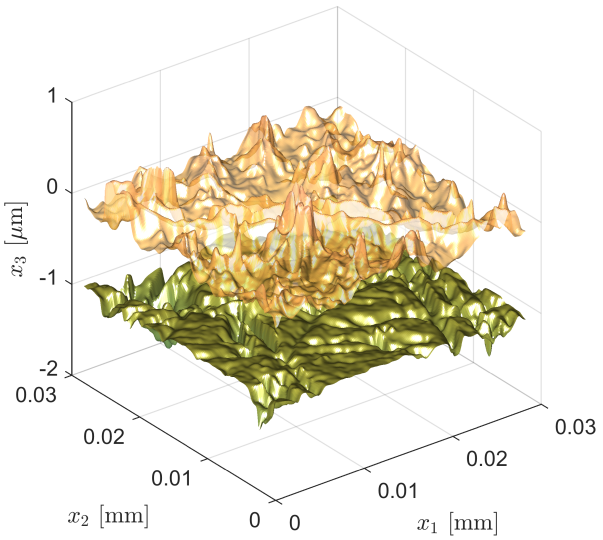

Figure 5.8: "Exemplary virtual microscopic geometry of patch 4 of test 2.1, where the disk is represented by the top surface and the pin by the bottom surface. Note the different scale of the vertical and the horizontal axes." The figure including its caption was published by [Hansen et al., 2023].

5.3 Calibration

"The parameter values used in the simulations are summarized in Table 5.4. The dynamic viscosity of the liquid phase μ_0 at ambient pressure is set according to Table 5.1. The Dirichlet boundary conditions of ambient pressure p_{amb} are employed for the fluid pressure p_{fl} at the domain boundaries. Furthermore, the Dirichlet boundary condition of $\theta = 0$ is used at the domain inlet, whereas Neumann conditions are used for the cavity fraction at the remaining boundaries. A tolerance of 10^{-6} is used as a threshold for the residuals [...].

First, the size of the Gaussian filter for the smoothing of the macroscopic topographies is evaluated. The filter size should be large enough to smooth out all roughness effects but small enough to prevent the filtering of macroscopic geometry features. The size of the Gaussian filter is parametrized by its full width at half maximum of the Gaussian distribution. The used macroscopic pin and disk topographies have a resolution of 500 $\times$ 500 points. The roughness properties of patch 4 of test 2.1 are used in this

Parameter	Value	Parameter	Value	Parameter	Value
$F_{N,imp}$	150 N	$p_{0,R}$	$1.96 \cdot 10^8$ Pa	K_P	$1.2 \cdot 10^{-2}$
U	$0.01 \ldots 2$ m/s	ν_{up}	0.3	K_I	$2.4 \cdot 10^{-2}$
p_{amb}	10^5 Pa	ν_{low}	0.3	K_D	$1.5 \cdot 10^{-3}$
p_{cav}	$8 \cdot 10^4$ Pa	E_{up}	$210 \cdot 10^9$ Pa	$C_{f,b}$	$1/(3\sqrt{3})$
ρ_0	850 kg/m^3	E_{low}	$210 \cdot 10^9$ Pa	$x_{1,ref}$	$8 \cdot 10^{-3}$ m
C_1	$5.9 \cdot 10^8$ Pa	$\alpha_{\overline{p}_{con}}$	0.05	$x_{2,ref}$	$8 \cdot 10^{-3}$ m
C_2	1.34	α_{p^*}	0.05	h_{ref}	10^{-6} m
α_R	$22 \cdot 10^{-9}$ /Pa	α_θ	0.05	μ_{ref}	μ_0
ρ_{ref}	ρ_0	p_{ref}	$100 \cdot 10^6$ Pa	u_{ref}	u_m

Table 5.4: "Employed parameter values of the HMEHL-FBNS solver. The parameters with indices $_{ref}$ are used to transform the steady homogenized Reynolds Equation into a dimensionless form [...]." The table including its caption was published by [Hansen et al., 2023].

case. The simulated Stribeck curves for the unfiltered profile and filter sizes of 3, 5, 7, 9 and 11 pixel are displayed in Figure 5.9a. This demonstrates that the smoothing of the geometry on the macroscopic scale causes the Stribeck curve to be shifted to lower relative velocities u_r.

In order to quantify the resulting deviations in the Stribeck curve, the 11 pixel filter size simulation is chosen as the reference $C_{f,ref}$ [to represent a measure for a smooth macroscopic geometry. As shown next, the Stribeck curves converge quickly for increasing filter sizes which suggests that even larger filters are unnecessary]. The results of $C_{f,dev}$ are displayed in Figure 5.9b. The deviations are the largest in the mixed lubrication regime. It is shown that the unfiltered profile can cause a deviation in the Stribeck curve of 45%. This is because the unfiltered macroscopic profile still contains roughness information which is already considered by the microscopic roughness scale. This wrongly creates a double implementation of roughness and causes a large shift in the Stribeck curve to higher relative velocities u_r. With increasing filter sizes, the Stribeck curves converge towards the reference solution. For a filter size of 9 pixel, the deviation becomes less than 0.5% which is chosen as the filter size for the following simulations [because it is deduced that this filter size is sufficient to remove undesired roughness artifacts from the macroscopic geometry].

The calibration of the macroscopic resolution is performed next by interpolating new geometries with the resolutions 128×128, 256×256, 999×999 and 1997×1997 from the one with a resolution of 500×500. The higher resolutions of 999×999 and 1997×1997 are chosen such that they exhibit all of the original 500×500 points with additional points in between. In order to save computational resources, the simulations for those resolutions are only conducted for relative velocities of 0.02, 0.04, 0.06, 0.08 and 0.1 m/s. The resulting Stribeck curves are shown in Figure 5.10a while the deviations of the friction coefficient $C_{f,dev}$ are depicted in Figure 5.10b. The Stribeck curve with the original resolution of 500×500 is chosen as $C_{f,ref}$. For the highest resolution, the maximum deviation is at 1.2%, while for a resolution of 256×256, its maximum absolute value is less than 1.8%. Comparing the resolution of 256×256 to 1997×1997 thus yields an estimate of a deviation of less than 3%, which is considerably less than the $\pm 10\%$ of the experiments. Therefore, a resolution of 256×256 is considered sufficient and is used for the following simulations.

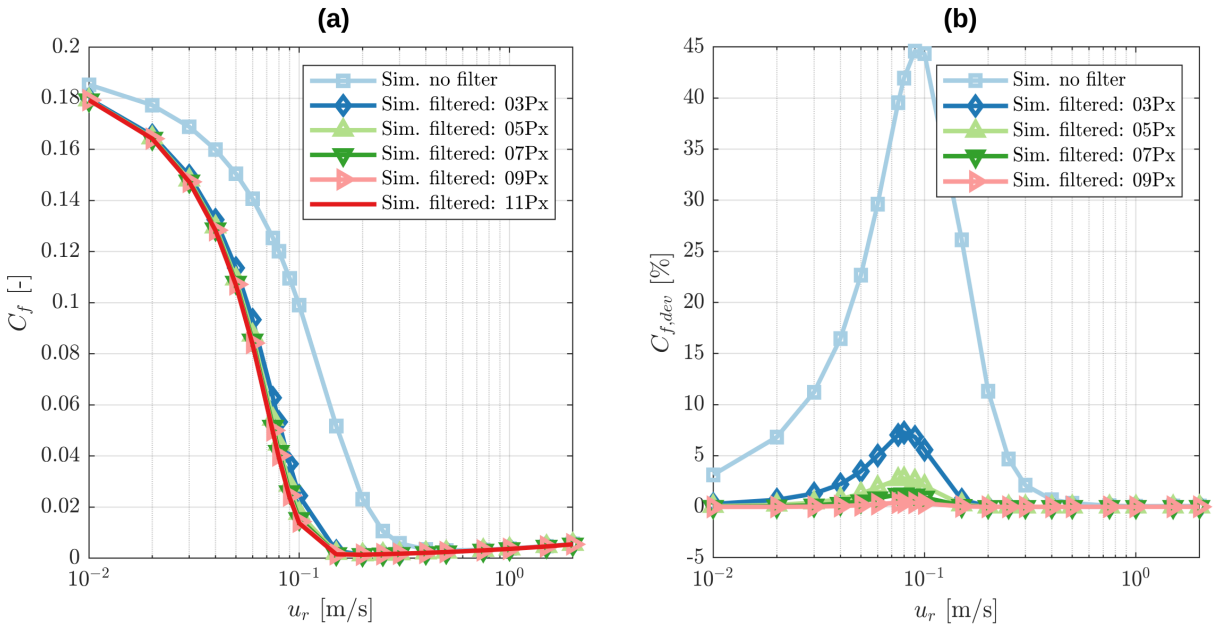

Figure 5.9: "Simulation results for different filter sizes: (a) Friction coefficient C_f as a function of relative velocity u_r; and (b) Deviation of the friction coefficient $C_{f,dev}$ as a function of relative velocity u_r." The figure including its caption was published by [Hansen et al., 2023].

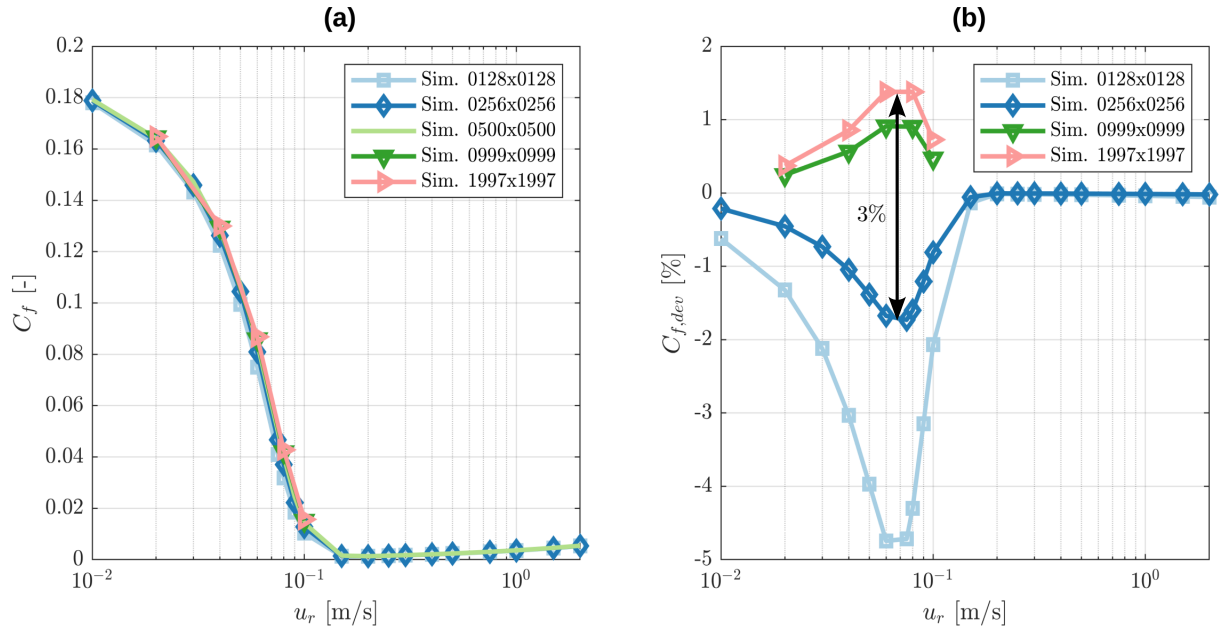

Figure 5.10: "Simulation results for different resolutions. (a) Friction coefficient C_f as a function of relative velocity u_r. (b) Deviation of the friction coefficient $C_{f,dev}$ as a function of relative velocity u_r." The figure including its caption was published by [Hansen et al., 2023].

Moreover, it is evaluated whether the macroscopic wear track on the disk influences the friction behaviour. Figure 5.11a shows the simulation results obtained when both the macroscopic pin and disk topographies are used to reconstruct the virtual geometry against the idealized case where the disk is assumed to be perfectly flat on the macroscopic scale. Figure 5.11b shows that this only causes a maximum absolute deviation in the friction coefficient of less than 4%, where the case with non-flat disk is chosen as $C_{f,ref}$. Assuming that the disk is flat is therefore legit in comparison to the deviation in

the experiments and performed for the following simulations. Furthermore, being able to neglect the macroscopic disc topography bears the significant advantage of a generally much simpler virtual geometry reconstruction workflow.

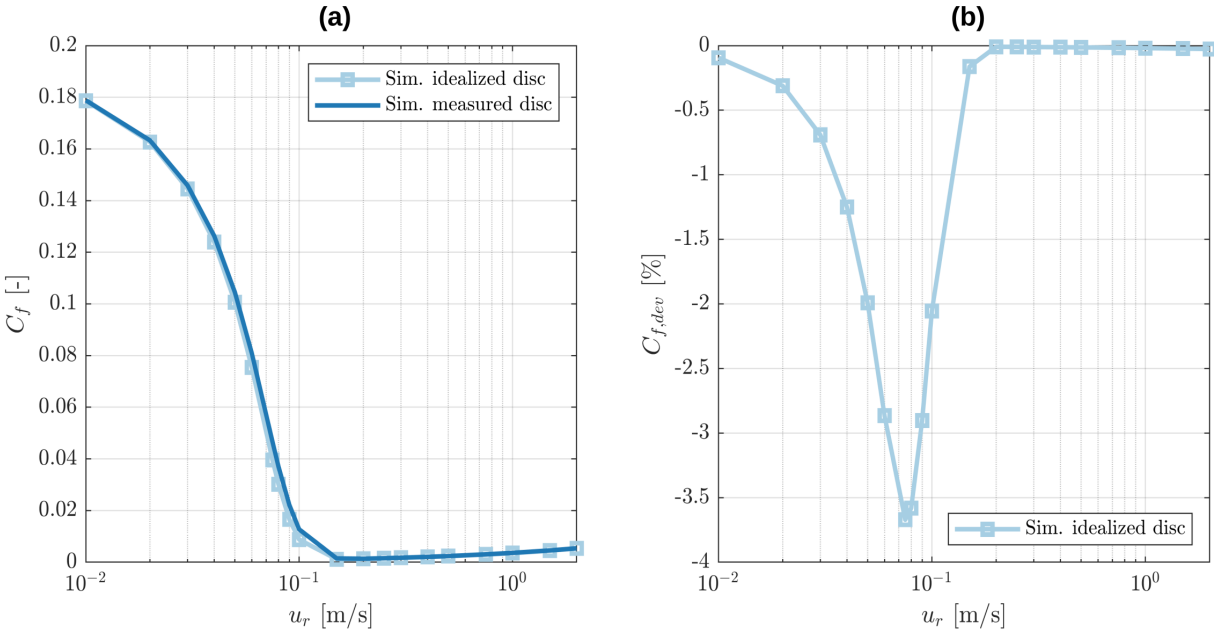

Figure 5.11: "Simulation results with idealised and measured macroscopic disk topography. (a) Friction coefficient C_f as a function of relative velocity u_r. (b) Deviation of the friction coefficient $C_{f,dev}$ as a function of relative velocity u_r." The figure including its caption was published by [Hansen et al., 2023].

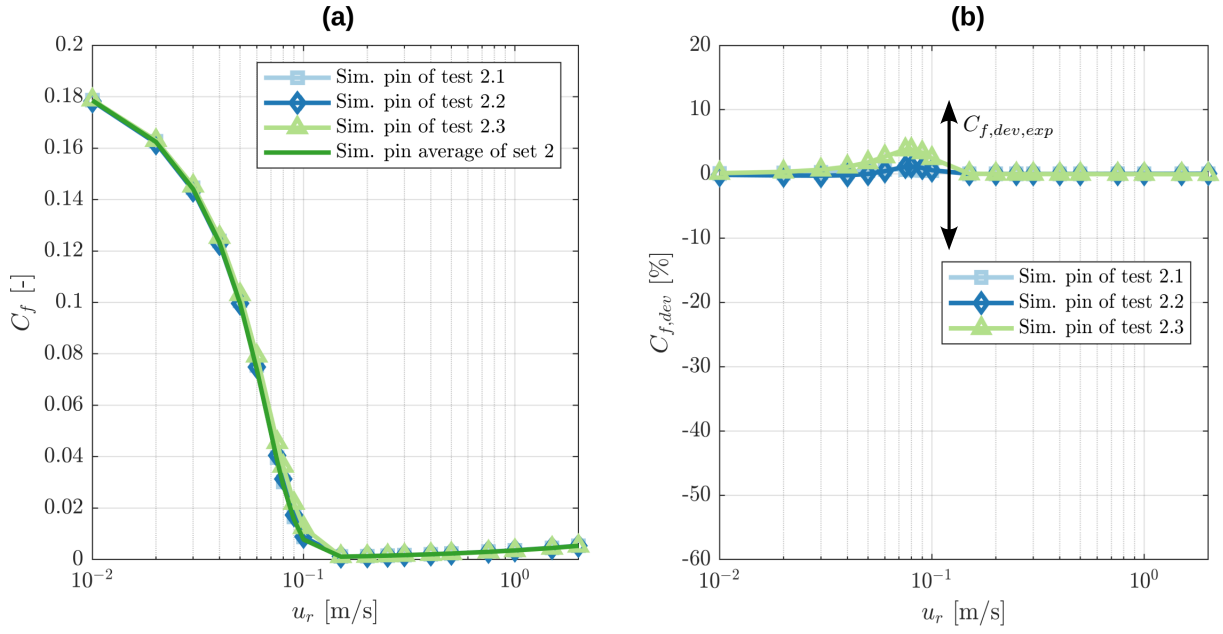

Figure 5.12: "Simulation results for different measured macroscopic pin topographies and their set average. (a) Friction coefficient C_f as a function of relative velocity u_r. (b) Deviation of the friction coefficient $C_{f,dev}$ as a function of relative velocity u_r." The figure including its caption was published by [Hansen et al., 2023].

The last step of calibrating the macroscopic geometry consists of averaging the macroscopic pin geometries of set 2, as shown previously in Figure 5.5. The Stribeck curves for the different topographies of tests 2.1, 2.2 and 2.3 and the average pin geometry of set 2 are depicted in Figure 5.12a. When the average pin geometry of set 2 is used as $C_{f,ref}$, the absolute deviations in the friction coefficient shown in Figure 5.12b are less than 4%. This low value first allows the very important deduction that the digital twin is robust with respect to the macroscopic measurement of the pin and that the macroscopic geometry obtained by averaging over the pins of set 2 is suitable for the following simulations. Second, the comparison to the deviations of $\pm 10\%$ in the experiments suggests that the deviations in the real-life measurements are unlikely to be caused by variations in the macroscopic geometry.

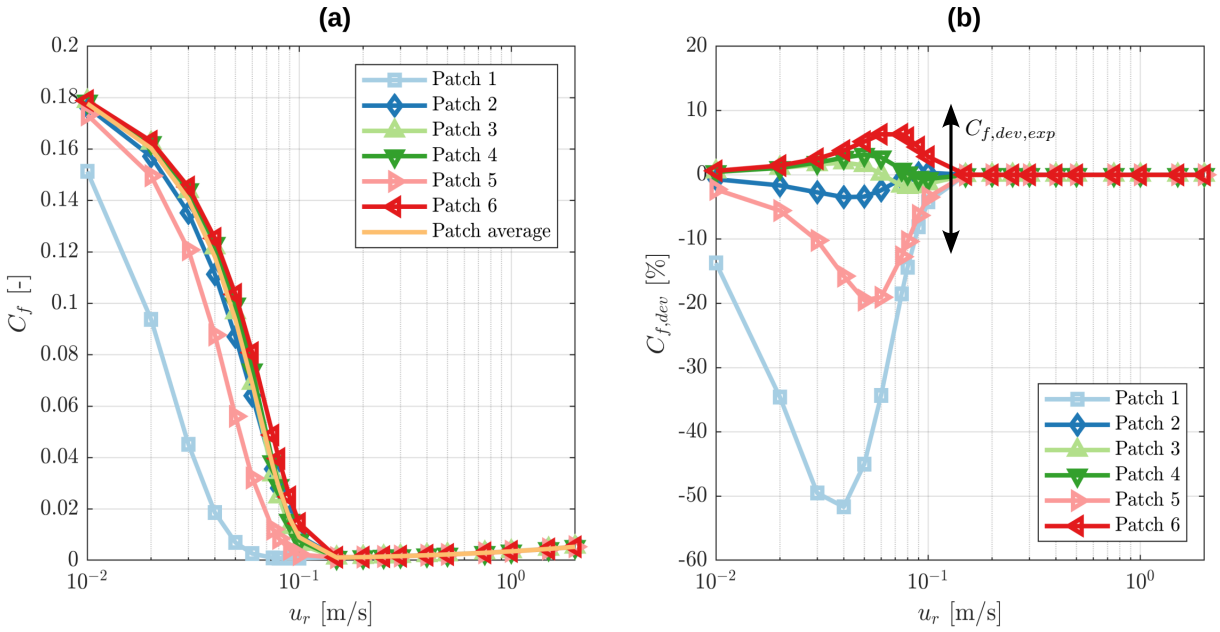

Figure 5.13: "Simulation results for different measured microscopic patches and their average. (a) Friction coefficient C_f as a function of relative velocity u_r. (b) Deviation of the friction coefficient $C_{f,dev}$ as a function of relative velocity u_r." The figure including its caption was published by [Hansen et al., 2023].

Finally, the microscopic calibration of the digital twin is performed. The Stribeck curves are simulated for the six different roughness patches obtained from test 2.1 and for the average of their roughness factors. The used roughness factors were shown earlier in Figures 5.6 and 5.7. The results are shown in Figure 5.13a. The deviations in the Stribeck curves are shown in Figure 5.13b, where the Stribeck curve based on the averaged roughness factors is used as $C_{f,ref}$. It becomes obvious that the digital twin is highly sensitive to the chosen roughness patch. While some patches deliver results closely the reference, other patches show deviations of up to 52%. In the mixed lubrication regime, the deviation of most roughness patches is of similar magnitude as the deviations within the experiment tests. This in turn suggests that the deviations in the experiments might be caused by differences in the roughnesses between the tests. At the same time, the variations in the roughnesses within test 2.1 also indicate that an actual tracing of exactly which roughness patch at which position on the pin surface dominates the behaviour of the Stribeck curve is extremely difficult and beyond the scope of this work. Instead, in the following, this work aims to investigate how suitable the average of the roughness factors of test 2.1 is for representing the microscopic geometry of the digital twin" [Hansen et al., 2023].

5.4 Validation

"As a useful tool for the validation of the calibrated virtual geometry, the Hersey number [41, Ch. 1.3.6], [43] for the considered pin-on-disk tribometer is derived to allow a certain degree of generalization of the obtained results. Starting point is the steady two-dimensional Reynolds equation, for simplicity without homogenization factors:

$$\nabla \cdot \left(\frac{\rho_l h^3}{12 \mu_l} \nabla p \right) - \frac{\partial}{\partial x_1} \left(\rho_l h u_m \left(1 - \theta \right) \right) \right) = 0. \tag{5.9}$$

An order of magnitude analysis can be performed when each dimensional variable and parameter is decomposed into its dimensionless value denoted by * and its reference value denoted by $_{ref}$:

$$h = h^* h_{ref}; \quad p = p^* p_{ref}; \quad \rho_l = \rho^* \rho_{ref}; \quad \mu_l = \mu^* \mu_{ref}; \quad x_1 = x_1^* x_{1,ref}; \quad x_2 = x_2^* x_{2,ref}; \quad u_m = u_m^* u_{m,ref}. \tag{5.10}$$

The magnitudes of the dimensional values are roughly estimated as follows:

$$\begin{aligned} p_{ref} = F_{N,imp}/D^2; \quad \rho_{ref} = \rho_0; \quad \mu_{ref} = \mu_0; \\ x_{1,ref} = D; \quad x_{2,ref} = D; \quad u_{m,ref} = U/2, \end{aligned} \tag{5.11}$$

where D is the diameter of the pin. Since h is adjusted by h_d in order to fulfil the load balance equation, its magnitude h_{ref} is unknown and cannot be directly estimated. To rectify this, the Reynolds equation is put into non-dimensional form using both the estimated and the unknown magnitudes:

$$\nabla^* \cdot \left(\frac{\rho^* h^{*3}}{\mu^*} \nabla p^* \right) - 6 \mathcal{S} \frac{\partial}{\partial x_1^*} \left(\rho^* h^* u_m^* \left(1 - \theta \right) \right) = 0, \tag{5.12}$$

which firstly allows to define the Sommerfeld number [41, Ch. 11.2], [81] of the pin-on-disk tribometer:

$$\mathcal{S} = \frac{\mu_0 U D^3}{h_{ref}^2 F_{N,imp}}. \tag{5.13}$$

The idea of the non-dimensionalization is that all dimensionless variables and parameters are approximately of magnitude 1 if the magnitudes of their dimensional counterparts are properly estimated. This, in turn, allows to approximately deduce the magnitude of the gap height h from the dimensionless Reynolds Equation (5.12) as:

$$h_{ref} \approx \sqrt{\frac{\mu_0 U D^3}{F_{N,imp}}}. \tag{5.14}$$

Next, the viscous stress is considered:

$$\tau_{fl,1} = -\frac{h}{2} \frac{\partial p}{\partial x_1} + \frac{\mu_l u_r}{h} (1 - \theta). \tag{5.15}$$

Using $u_r = u_r^* u_{r,ref}$ with $u_{r,ref} = U$ and reformulating the right side of the above equation yields:

$$\tau_{fl,1} = \sqrt{\frac{\mu_0 U F_{N,imp}}{D^3}} \left(-\frac{h^*}{2} \frac{\partial p^*}{\partial x_1^*} + \frac{\mu^* u_r^*}{h^*} (1 - \theta) \right), \tag{5.16}$$

which allows one to deduce the magnitude of the viscous stress as:

$$\tau_{fl,1,ref} = \sqrt{\frac{\mu_0 U F_{N,imp}}{D^3}}. \tag{5.17}$$

Lastly, the scaling behaviour of the friction coefficient in the hydrodynamic regime can be found by estimating its magnitude using $F_{T,fl,ref} = \tau_{fl,1,ref} D^2$:

$$C_{f,hd,ref} = \frac{F_{T,fl,ref}}{F_{N,imp}} = \sqrt{\mathcal{H}}, \tag{5.18}$$

where

$$\mathcal{H} = \frac{\mu_0 U D}{F_{N,imp}}, \tag{5.19}$$

is the Hersey number [41, Ch. 1.3.6] of the pin-on-disk tribometer. An equivalent expression of $\mathcal{H}$ for horizontal journal bearings under steady and fully lubricated conditions was first derived by Hersey [43] in 1914 using the Buckingham Π theorem. The derived Hersey number in Equation (5.19) provides a basis for a very particular theoretical understanding of the hydrodynamics of the lubricant flow: the imposed normal load and thus the hydrodynamic load carrying capacity are directly proportional to the dynamic viscosity of the lubricant [and the sliding velocity U].

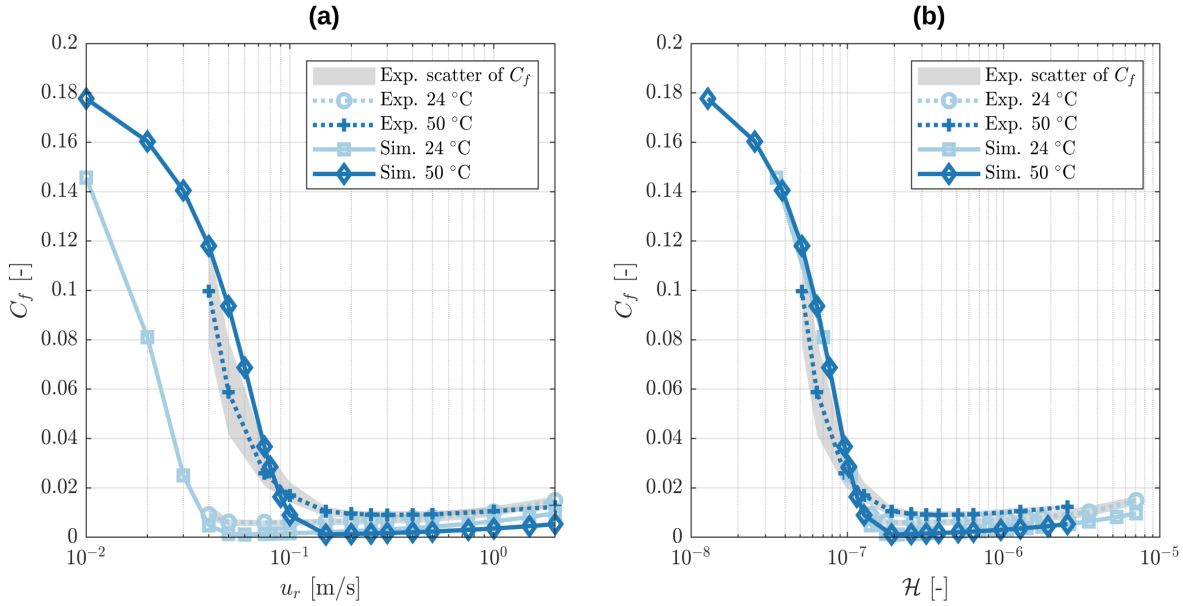

Figure 5.14: "Stribeck curves for different temperatures. Full lines: simulation results. Dashed lines: experiment results of set averages. (a) Friction coefficient C_f as a function of relative velocity u_r. (b) Friction coefficient C_f as a function of Hersey number $\mathcal{H}$." The figure including its caption was published by [Hansen et al., 2023].

For validation, the defined reference geometry obtained with a 9 pixel filter, 256×256 resolution, smooth macroscopic disk, macroscopic pin average of set 2 and roughness factor average over patches 1 to 6 of test 2.1 is employed for simulations with the oil's respective dynamic viscosities at 24 and 50 °C. The simulation results are plotted in comparison to the experiment Stribeck curves of sets 1 and 2 in Figure 5.14a as a function of the relative velocity u_r and in Figure 5.14b as a function of the Hersey number $\mathcal{H}$. When the Hersey number is used, all results collapse on one curve, which first shows that the dynamic viscosity proportionality is applicable to both the simulation and the experiment. Second,

this demonstrates that the model is capable of predicting the transition from the hydrodynamic to the mixed lubrication regime. While the curve collapsing of the simulation results is a consequence of the underlying equations and thus only a verification of a correct implementation, the agreement of the collapsed simulation with the experiment Stribeck curves validates the digital twin as a tool to predict the friction behaviour of a pin-on-disk tribometer in the mixed lubrication regime.

Furthermore, the following line of argumentation can be drawn for the mixed lubrication regime. According to the employed model, the friction coefficient in the mixed lubrication regime is dominantly determined by the surface contact pressure, which in turn is determined by the load carrying capacity of the lubricant. The reason for this is that the lubricant pressure build up separates the surfaces as much as it can while the remaining load is carried by the contact pressure which then causes the large contact shear stress.

In essence, this means that the friction coefficient in the mixed lubrication regime is strongly influenced by the load carrying capacity of the lubricant flow. Keeping in mind that the mixed lubrication regime can consistently be represented by a collapsed curve for the experiments and the simulations, this leads to the confirmation that the hydrodynamic load carrying capacity is indeed proportional to the dynamic viscosity of the lubricant, as predicted earlier by Equation (5.19). Finally, this allows to conclude that the presented digital twin can properly predict the load carrying capacity of the real-life lubricant flow and is a valid tool to gain valuable insights into tribological systems" [Hansen et al., 2023].

In order to wrap up the validation, the crucial parameters and identified essential steps to obtain the calibrated digital twin are summarized in the following. First, the sliding speed U, the imposed normal load $F_{N,imp}$ and dynamic viscosity of the lubricant μ_0 need to be known while the coefficients of the Roelands and Dowson-Higginson model are not essential to perform a simulation but remain useful additional parameters. Furthermore, the cavitation pressure p_{cav} is required. Since it is difficult to determine, it is usually approximated by a value between $0\,\mathrm{Pa}$ and the ambient pressure p_{amb}. Moreover, the material properties of the solid surfaces, namely the Young's modulus E, the Poisson ratio ν and the hardness Hrd need to be known in order to model the elastic behaviour on the macroscopic scale and the elastic-plastic behaviour on the roughness scale. As the last important parameter, the boundary friction coefficient $C_{f,b}$ directly influences the value of the friction in the mixed and boundary lubrication regime. While it is approximated in the current work by a value that was theoretically derived by Bowden and Tabor [14, Ch. V] for the dry friction of metals under pure shearing, it can also be determined by experiments with a clearly defined boundary lubrication region. Considering the virtual geometries, a smooth macroscopic profile and highly resolved roughness profiles showed to be essential. Since the Stribeck curve is highly sensitive with respect to different roughness profiles, the employment of several roughness profiles is recommended such that the homogenization factors, mean gap heights and contact pressures can be averaged.

As a final remark: additional follow-up simulations that were not presented in this manuscript because they were not prepared up to publication level indicated that the modelling of piezoviscosity can slightly increase the load carrying capacity of the fluid since it results in a higher viscosity within the contact. At the same time, the induced changes in the Stribeck curves are smaller than the presented effects due to different roughness profiles while compressibility effects seemed to be negligible. A comparison of rigid and elastic modelling on the macroscopic scale furthermore suggested that rigid profiles have a higher load carrying capacity than elastic profiles. At the same time, the elasticity smooths out peaks on the macroscale where surface contact initially occurs. Thus, the surface contact occurs at lower velocities in the elastic case than in the rigid one. The corresponding shift in the Stribeck curve appeared to be of similar magnitude as the effect of the different roughness profiles. Additional investigations showed

that the effect of the roughness on the hydrodynamic load carrying capacity by means of homogenization factors is notable in the Stribeck curve but less pronounced than the roughness effects on the mean contact pressure. It seems that it is most important to properly catch the roughness height itself because it defines the macroscopic gap height below which the mean contact pressure is introduced and thus when surface contact is initiated on the macroscopic scale of the simulation. As shown in a preliminary work by [Hansen et al., 2020], there are also certain roughness profiles where the effect on the contact pressure completely dominates over the effect on the fluid pressure.

5.5 Conclusion

"In this investigation, a procedure for the establishment and subsequent calibration of a digital twin of a pin-on-disk tribometer was presented. Particularly noteworthy is the fact that its virtual geometry is not approximated by parameterized shapes, but instead, it is completely deduced from real-life topography measurements. The advantage of this approach is that the described procedure can be applied to any geometry, even one that is too complex to be parameterized, as long as its topographies can be measured. The presented work includes a description of the real-life experiment procedure, the topography measurements of the specimens [and] the reconstruction of the virtual geometry [...]. Furthermore, the Hersey number was derived to generalize findings about the hydrodynamic load carrying capacity and friction behaviour of the pin-on-disk tribometer and to allow the verification and validation of the digital twin with experiment results. During the conducted evaluation of the experiment and simulation of the Stribeck curves, the following key statements were drawn:

- Filtering of the macroscopic topographies is an essential step for multi-scale solvers to prevent a double consideration of roughness. After filtering, the digital twin is very robust with regard to variations in the macroscopic geometry of different specimens. The macroscopic geometry of the disk is even negligible.
- The digital twin is highly sensitive to the employed roughness patch. Averaging over the computed influence factors of several roughness patches was shown to deliver good agreement with the experiment results. The deviations of simulations for different roughness patches are of similar magnitude as the deviations of the experiments within one set, thus suggesting that the deviations in the experiment are caused by variations in the roughness.
- The hydrodynamic load carrying capacity scales proportionally with the dynamic viscosity of the lubricant. This leads to a collapse of Stribeck curves in the mixed lubrication regime when the friction coefficient is plotted as a function of the Hersey number" [Hansen et al., 2023].

6 Textured Surfaces

Within this chapter, surface textures are investigated with the digital twin of a pin-on-disk tribometer that was presented in the previous chapter. First, a review of the literature knowledge on mechanisms associated with surface textures is presented to motivate and guide the investigation. Second, the parameters to describe the surface textures and the texturing pattern are introduced. Subsequently, a tuning of simulation parameters is performed to find a reasonable trade-off between accuracy and computational costs since the simulations of textured surfaces have to be executed at significantly higher grid resolutions. Afterwards, different surface texture configurations are numerically investigated with regard to friction reduction in the mixed lubrication regime. The numerical results are briefly compared with reference data of real-life experiments. Lastly, the results are discussed in the context of the literature, including the publication *Sensitivity of the Stribeck Curve to the Pin Geometry of a Pin-on-Disc Tribometer* by [Hansen et al., 2020], to evaluate the applicability of the isothermal Reynolds equation to replicate mechanisms introduced by surface textures.

6.1 Literature Understanding of Surface Texture Mechanisms

Within the last thirty years, the optimum dimple design of surface textures to obtain maximum friction reduction in lubricated contacts has been studied extensively in the literature [27, 36, 59, 2, 61]. For example, it has been shown that surface textures can increase the performance and durability of seals or reduce the friction when applied to piston rings [27]. Surface texturing is even considered as a promising technique to tailor hip implants to patient specific requirements [2]. In the case of slider [23], thrust [42] or journal bearings [52], it is commonly agreed upon that their performance can be significantly increased in the hydrodynamic lubrication regime by texturing certain parts of the tribological contact while full texturing of the whole contact causes only a limited increase or even a performance decrease [36]. Furthermore, performance increases due to partial texturing are found to be the largest for parallel contacts and become less with increasing gap inclinations [23, 36]. Exemplary partial texturing of a parallel and an inclined slider contact with dimples of depth h_{dpl} are depicted in Figure 6.1.

In the literature, suggestions for the underlying mechanisms that cause the friction reduction are the entrapment of wear debris within the surface textures [36], less adhesion because of a smaller contact area in the case of boundary lubrication [36, 2], dimples acting as lubricant reservoirs to prevent starvation [36] or an increased hydrodynamic lift due to a more advantageous gap geometry [40, 36]. Especially the last mechanism has been studied extensively with simulations because it can be demonstrated by solving the Reynolds equation [36]. It is shown in the literature that based on the Reynolds equation, the maximum hydrodynamic lift is achieved by approximating a Rayleigh step through partial front texturing as shown in Figure 6.2 [23, 36]. This Rayleigh step can even be described by an analytical solution which results in an optimum step length of $l_{h,opt} = 0.7182L$ and the optimum shoulder height $s_{h,opt} = 1.155h_{min}$ being a function of the minimum gap height h_{min} [41, Ch. 8.6]. In more realistic three-dimensional problems, the Rayleigh step needs to be additionally bounded at the sides to prevent side leakage [20].

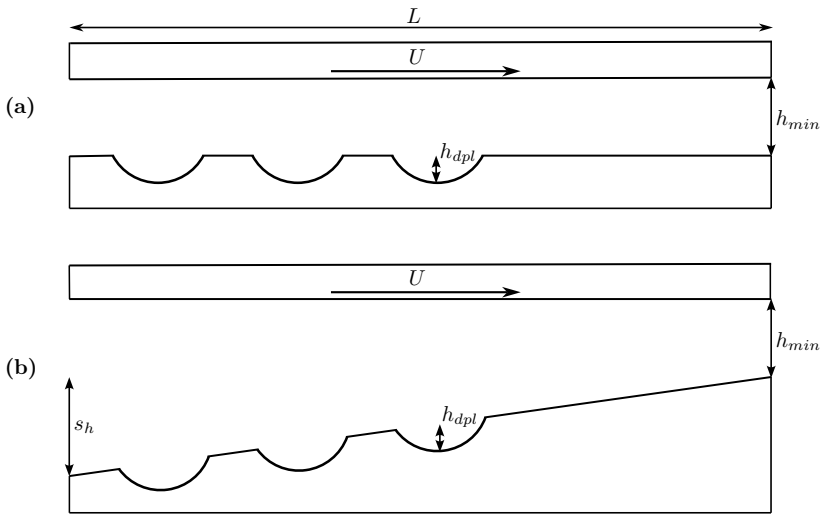

Figure 6.1: Schematic depiction of partial texturing in **(a)** a parallel and **(b)** an inclined slider contact with shoulder length s_h. The upper surface moves over the domain of length L with the velocity U. The minimum gap height is described by h_{min}. The figure is adapted from the publication by Gropper *et al.* [36].

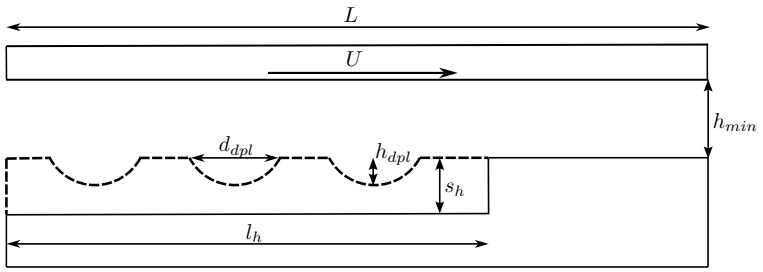

Figure 6.2: Schematic depiction of the approximation of a Rayleigh step with shoulder length s_h and step length l_h by partially texturing of a slider contact. The upper surface moves over the domain of length L with the velocity U. The minimum gap height is described by h_{min}. The figure is adapted from the publication by Gropper *et al.* [36].

Numerical studies that investigate the optimum dimple parameters to maximize the efficiency of surface textures are mainly performed in the hydrodynamic lubrication regime under conditions where the dimple depth h_{dpl} is of a similar magnitude as the minimum gap height h_{min} [36]. In such cases, it was shown that the Reynolds equation is applicable for certain Reynolds numbers and dimple aspect ratios $\lambda_{dpl} = d_{dpl}/h_{dpl} \geq 10$, where d_{dpl} is the dimple diameter [25]. For smaller dimple aspect ratios, friction terms that are neglected in the Reynolds equation become relevant and the Stokes equations are required. For $\lambda_{dpl} \geq 10$, a critical Reynolds number exists below which the Reynolds equation delivers accurate results. The corresponding critical Reynolds number is a function of the dimple aspect ratio [25]. For higher Reynolds numbers, inertia effects become relevant and thus require either a correction of the Reynolds equation [6] or the full NSE. Up to a certain dimple depth, inertia effects can provide a positive contribution to the load carrying capacity [22]. Further increasing the dimple depth results in detrimental inertia effects, but still causes a growing load carrying capacity until another threshold is reached. Passing this threshold, which is in the magnitude of the minimum gap height, will eventually cause recirculation zones to appear within the dimples and the load carrying capacity starts to decrease. Furthermore, special attention has to be paid to the cavitation model in cases where cavitation with a subsequent downstream full-film reformulation occurs [7]. This is a common phenomenon in textured

surfaces and the employment of a non-mass-conserving cavitation model will then lead to a large overestimation of the pressure build up. Thus, a mass-conserving cavitation model is essential to evaluate improvements in the load carrying capacity due to surface textures.

Considering real-life experiments in contrast to idealized simulations, partial texturing of the stator in a thrust pad bearing is experimentally confirmed to result in larger clearances and reduced friction in the hydrodynamic regime when compared to the untextured case [29]. Furthermore, experiments with fully textured rotors in a pin-on-disk tribometer show that full texturing is able to significantly reduce the friction in the mixed lubrication regime by extending the hydrodynamic lubrication regime towards lower Hersey numbers [53]. This effect becomes most pronounced for an optimum texturing density [54]. Moreover, the pin-on-disk experiments by Braun *et al.* [16] suggest a temperature dependent optimum dimple diameter when the dimple aspect ratio is kept constant during the texturing of the static pin. In a subsequent work, Schneider *et al.* [79] found an optimum texturing density of $\rho_{txt} = 10\%$, an optimum dimple aspect ratio of $\lambda_{dpl} = 10\%$ and a hexagonal pattern as a preferable dimple arrangement. Significant friction reduction in the mixed lubrication regime due to texturing of the complete tribological contact is not only found for the conformal contacts of pin-on-disk tribometers, but also for the highly loaded non-conformal contacts in ball-on-disk tribometers [73]. Some of the textures are even able to reduce friction in the full-film regime.

With respect to complementary experimental and numerical investigations of surface textures in pin-on-disk tribometers, a drop of the friction coefficient in the hydrodynamic regime is observed in experiments with fully textured pins by Scaraggi *et al.* [77, 76] and corresponding purely hydrodynamic simulations suggest it being caused by a shear stress reduction. At the same time, a friction reduction in the mixed lubrication regime of the experiments cannot be explained by the simulation results which showed a decrease in the pressure distribution [77]. Another systematic study to identify the optimum dimple shape in the contact of a pin-on-disk tribometer is published by Codrignani *et al.* [19]. With a purely hydrodynamic simulation model, partial front texturing with a dimple depth proportional to the minimum gap height is found to be the most efficient configuration, while the dimple diameter and pattern seem to be of negligible relevance. The authors use their numerical results obtained at gap heights well in the hydrodynamic regime as an explanation for the friction reduction observed in the mixed lubrication regime of the complementary experiments [19]. This deduction however has to be handled cautiously because according to the found proportionality, the optimum dimple depth in mixed lubrication should have been in the magnitude of the roughness height since this is the gap height at which surface contact occurs. The complementary experiments [19] however were conducted at much larger dimple depths.

The described inconsistencies in the literature between experiments and numerical simulations question the suitability of simulations to investigate surface textures in mixed lubrication because the numerical model might miss the relevant friction reducing mechanism. This currently unresolved knowledge gap is summarized in the research question that is addressed in this chapter: can simulations based on the Reynolds equation be employed to investigate the experimentally observed friction reduction due to surface texturing in the mixed lubrication regime? In order to tackle this question, the literature knowledge about the optimum dimple and texture configurations to create the maximum load carrying capacity will be directly tested within the mixed lubrication regime using the HMEHL-FBNS algorithm and complementary experiments.

6.2 Surface Texturing Parameters

In order to perform simulations of textured surfaces, spherical dimples are added on top of the levelled reference geometry that was determined in the previous chapter. This is schematically visualized in Figure 6.3. The spherical dimple shape is obtained by partially submerging a sphere into a plane, such that the texture is of dimple depth h_{dpl} and dimple diameter d_{dpl}. In some cases the dimple aspect ratio $\lambda_{dpl} = d_{dpl}/h_{dpl}$ is also used for its characterization. Identical dimples are arranged in unit triangles of height $l_{H,tri}$ and base length $l_{B,tri}$ along with its angles α_{tri}, β_{tri} and γ_{tri}. The texturing density is defined as half of the projected dimple area A_{dpl} divided by the area A_{tri} of the unit triangle:

$$\rho_{txt} = \frac{A_{dpl}}{2}/A_{tri} = \frac{\pi}{4}\frac{d_{dpl}^2}{l_{H,txt}l_{B,txt}}. \tag{6.1}$$

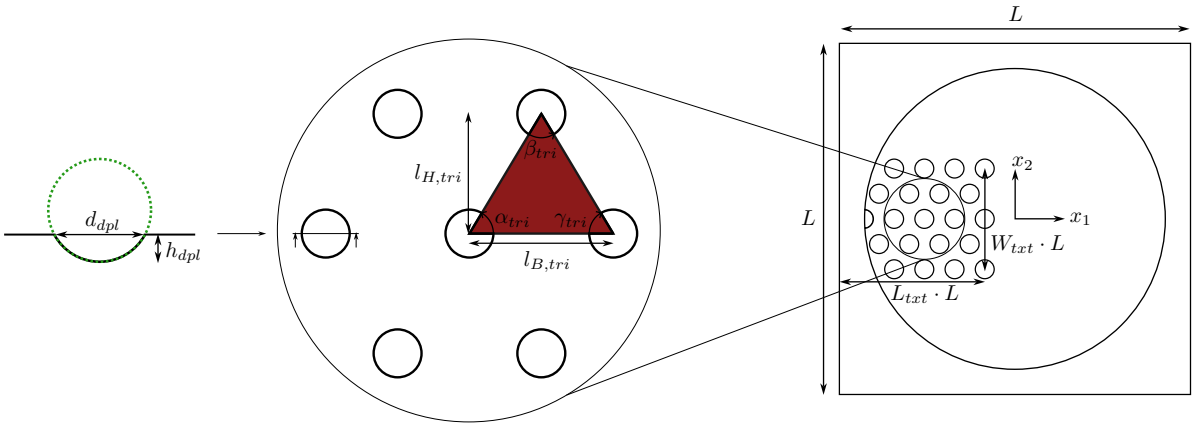

Figure 6.3: Schematic depiction of how spherical dimples are arranged into unit triangles to create texture patterns on parts of the pin's surface.

For an imposed texturing density ρ_{txt}, the unit triangle's height and width can be expressed as:

$$l_{B,tri} = \sqrt{\frac{\pi d_{dpl}^2}{4\rho_{txt}}\left(\frac{1}{\tan(\alpha_{tri})} + \frac{1}{\tan(\gamma_{tri})}\right)}, \tag{6.2}$$

$$l_{H,tri} = \frac{l_{B,tri}}{\frac{1}{\tan(\alpha_{tri})} + \frac{1}{\tan(\gamma_{tri})}}, \tag{6.3}$$

where the angles α_{tri}, β_{tri} and γ_{tri} are set according to the desired pattern. For the hexagonal dimple arrangement that will be investigated in this chapter, they are set to $\alpha_{tri} = \beta_{tri} = \gamma_{tri} = 60°$. The pin is placed in the center of the computational domain whose coordinates range from $-L/2$ to $L/2$, where the coordiante range length is $L = 8\,\mu\text{m}$. The textures are applied on top of the pin if their centers are in the range of $[-L/2, -L/2 + L_{txt} \cdot L]$ for the x_1- and $[-W_{txt} \cdot L/2, W_{txt} \cdot L/2]$ for the x_2-direction. The textured fractions of L are denoted by the texturing length L_{txt} and texturing width W_{txt}, where both L_{txt} and W_{txt} are dimensionless quantities.

6.3 Tuning of Simulation Parameters

The simulation parameters employed within this chapter are summarized in Table 6.1. Dirichlet boundary conditions of ambient pressure p_{amb} are used for the fluid pressure p_{fl}, while for the cavity fraction Dirichlet boundary conditions of $\theta = 0$ are used at the domain inlet, whereas Neumann conditions are implemented at the remaining boundaries.

Parameter	Value	Parameter	Value	Parameter	Value
$F_{N,imp}$	150 N	$p_{0,R}$	$1.96 \cdot 10^8$ Pa	K_P	0
U	$0.01 \ldots 2$ m/s	ν_{up}	0.3	K_I	0.1
p_{amb}	10^5 Pa	ν_{low}	0.3	K_D	0
p_{cav}	$8 \cdot 10^4$ Pa	E_{up}	$210 \cdot 10^9$ Pa	$C_{f,b}$	$1/(3\sqrt{3})$
ρ_0	850 kg/m^3	E_{low}	$210 \cdot 10^9$ Pa	$x_{1,ref}$	$8 \cdot 10^{-3}$ m
C_1	$5.9 \cdot 10^8$ Pa	$\alpha_{\overline{p}_{con}}$	0.05	$x_{2,ref}$	$8 \cdot 10^{-3}$ m
C_2	1.34	α_{p^*}	0.05	h_{ref}	10^{-6} m
α_R	$22 \cdot 10^{-9}$ /Pa	α_θ	0.05	μ_{ref}	μ_0
ρ_{ref}	ρ_0	p_{ref}	$100 \cdot 10^6$ Pa	u_{ref}	u_m
μ_0	0.024 Pas				

Table 6.1: Employed parameter values of the HMEHL-FBNS solver.

Due to the small diameter of the dimples, a large amount of computational cells is required to provide a sufficient resolution for each dimple. This in turn significantly increases the computational costs of the simulations and limits most of the surface texture investigations to specific points of the Stribeck curve. To some extend, this can be rectified by adjusting the tolerance of the algorithm such that the resulting accuracy is not higher than necessary. This is investigated in this section for a case without surface textures and a grid resolution of 256×256 cells. The purpose of this preliminary study is that the subsequent simulations of textured surfaces in the following section can be directly performed with the proper setting at higher resolutions. Figure 6.4a shows Stribeck curves that are obtained with the maximum pressure residual definition of $r^n_{HMEHL-FBNS} = \max\left(\text{abs}\left(\vec{\delta}^n_{p^*}\right), \text{abs}\left(\vec{\delta}^n_{\overline{p}^*_{con}}\right)\right)$ for different tolerances against the strict definition provided by Equation (3.42) with a tolerance of 10^{-6}. Differently to the simulation with the strict definition, the HMEHL-FBNS algorithm is additionally slightly adjusted for the simulations with the maximum pressure residual such that the matrix A_h is tridiagonal. It consequently contains only the diagonals corresponding to the West, Center and East cells because this showed to further improve the efficiency of the solver. The friction coefficients of the strict case are denoted by $C_{f,strct}$ such that the deviations of the obtained friction coefficients in relation to $C_{f,strct}$ can be defined as:

$$Dev\left(C_f\right) = \frac{C_f - C_{f,strct}}{C_{f,strct}}. \tag{6.4}$$

Figure 6.4b shows that the maximum pressure residual definition with a tolerance of 10^{-4} is sufficient to produce deviations in the Stribeck curve of less than 0.76%. At the same time, Figure 6.4c shows that the amount of iterations N_{it} and thus the computational cost is approximately halved in comparison to the strict residual definition and its tolerance. These savings are considerable, but computing the solution at one point of the Stribeck curve still requires several hours for resolutions of 1997×1997 cells. Extending this to complete Stribeck curves would require several days. While this can still be a reasonable time

frame for optimization studies which aim at tailoring surface textures to specific operating conditions along the Stribeck curve, the computation of the whole Stribeck curve is not necessary for the present study about the general suitability of the employed model in mixed lubrication. Instead, a single point on the Stribeck curve just at the onset of the mixed lubrication regime is selected to perform targeted parameter studies in the next section. According to Figure 6.4a, such a point is provided by a relative velocity of $u_r = 0.1\,\mathrm{m\,s^{-1}}$.

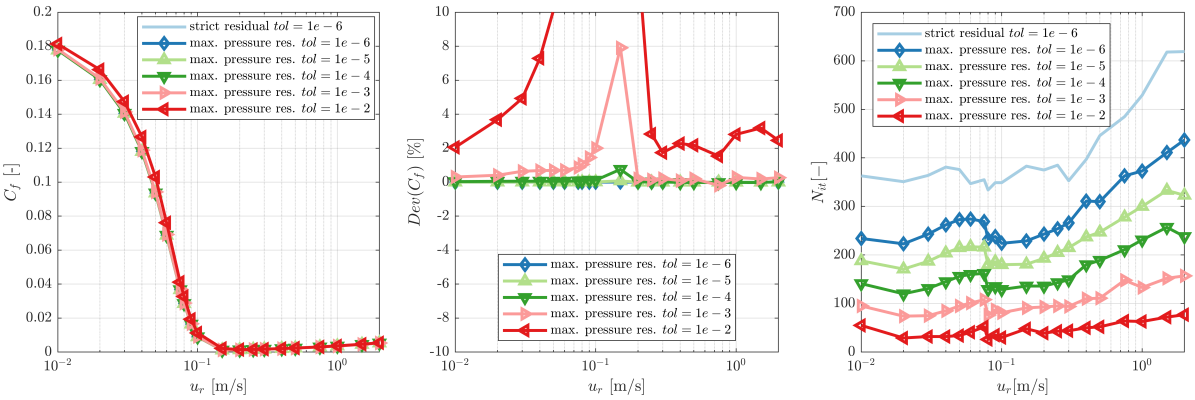

(a) Friction coefficient C_f as a function of the relative velocity u_r.

(b) Deviations of the friction coefficient $Dev\,(C_f)$ as a function of the relative velocity u_r.

(c) Amount of required iterations N_{it} as a function of the relative velocity u_r.

Figure 6.4: Impact of different tolerances on the Stribeck curve and simulation performance.

6.4 Surface Textures in Mixed Lubrication

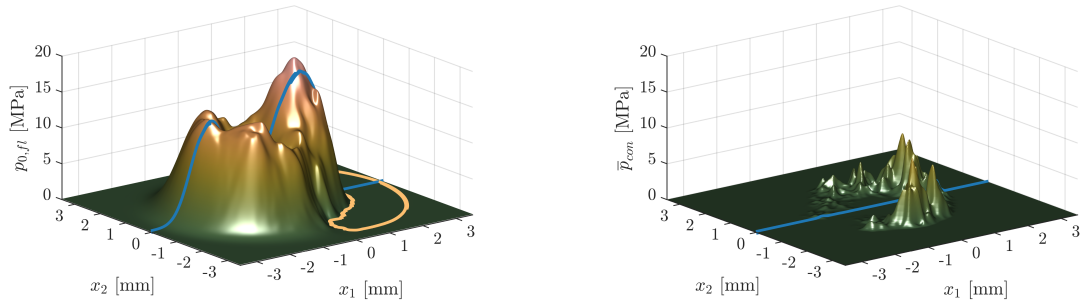

(a) Macroscopic fluid pressure profile $p_{0,fl}$ with boundary of the cavitation region marked in orange and center line marked in blue.

(b) Mean contact pressure profile $\overline{p}_{con}$ with center line marked in blue.

Figure 6.5: Load sustaining pressure contributions of the untextured contact at a relative velocity of $u_r = 0.1\,\mathrm{m\,s^{-1}}$ 1997x1997

In order to confirm that the conditions within the gap at $u_r = 0.1\,\mathrm{m\,s^{-1}}$ indeed correspond to mixed lubrication, the fluid and contact pressures above an untextured pin at a resolution of 1997×1997 cells are displayed in Figures 6.5a and 6.5b. They show that this operating condition is dominated by the macroscopic fluid pressure while mean contact pressures of the same magnitude sustain the remaining parts of the applied load, thus exactly representing the onset of the mixed lubrication regime. In order to quantify the friction reduction due to surface texturing, the texture efficiency is defined as [16]:

$$\eta_{txt} = \frac{C_{f,untxt} - C_{f,txt}}{C_{f,untxt}}. \tag{6.5}$$

Before starting the parametric study, it is useful to estimate the accuracy of the simulation results as it is limited by the employed grid resolution. Therefore, a grid convergence study is performed for two surface texture configurations. Both configurations contain the smallest dimple diameter of $d_{dpl} = 40\,\mu\text{m}$ and are consequently expected to represent worst case scenarios with the least amount of grid points per dimple. Furthermore, the two configurations are selected such that one is of poor and the other one is of good texture efficiency. As will be shown by the subsequent parameter study later in this section, the first case is a configuration with texturing length of $L_{txt} = 50\%$ and a texturing width of $W_{txt} = 100\%$, while the better performing configuration has a texturing length of $L_{txt} = 40\%$ and texturing width of only $W_{txt} = 40\%$. Both configurations have texturing densities of $\rho_{txt} = 20\%$ and dimple depths of $h_{dpl} = S_q$, where the root-mean-square of the roughness is $S_q = 145.7\,\text{nm}$. At the previously determined relative velocity of $u_r = 0.1\,\text{m}\,\text{s}^{-1}$, the texture efficiencies are displayed in Figure 6.6 for grid resolutions N of 500×500, 999×999 and 1997×1997 cells. The first configuration shows in Figure 6.6a that a grid of 1997×1997 cells produces a texture efficiency of approximately $\eta_{txt} = 0.42\%$. The difference in the texture efficiencies between the resolutions of 999×999 and 1997×1997 cells can be used to estimate the scatter of further refined grids to be $\Delta\eta_{txt} = -0.069\%$. In this sense, a resolution of 3993×3993 cells is expected to result in a texture efficiency η_{txt} within the range between 0.42% and $0.42\% - 0.069\% = 0.4131\%$. Even higher resolved grids are estimated not to result in texture efficienies below the lower threshold of $\eta_{txt} = 0.4131\%$, because the scatter $\Delta\eta_{txt}$ between two adjacent resolutions quickly decreases for increasing gap resolutions. This can be seen in the evolution of η_{txt} from the resolutions of 500×500 to 1997×1997 cells in Figure 6.6a. The evolution of the second configuration is shown in Figure 6.6 which demonstrates that this configuration can deliver a texture efficiency of $\eta_{txt} = 12.2\%$ at a resolution of 1997×1997 cells with a scatter of $\Delta\eta_{txt} = -0.43\%$. The results show that the scatter is growing with an increasing texture efficiency, but stays in reasonable limits to compare different configurations at grid resolutions of 1997×1997 cells. Since this resolution is also of feasible computational costs, it is employed in the following.

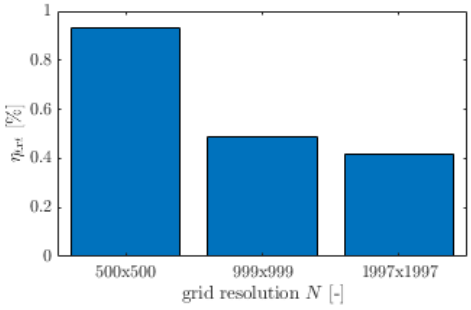

(a) Texture efficiency η_{txt} for different grid resolutions N at a texturing length of $L_{txt} = 50\%$ and texturing width of $W_{txt} = 100\%$.

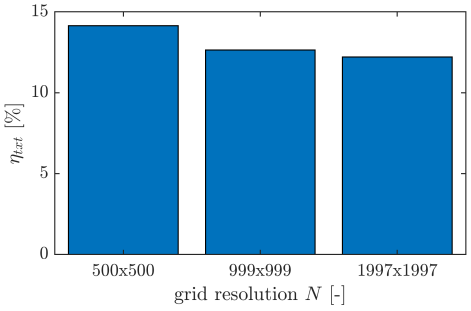

(b) Texture efficiency η_{txt} for different grid resolutions N at a texturing length of $L_{txt} = 40\%$ and texturing width of $W_{txt} = 40\%$.

Figure 6.6: Grid convergence studies for a texturing density of $\rho_{txt} = 20\%$, dimple diameter of $d_{dpl} = 40\,\mu\text{m}$ and dimple depth of $h_{dpl} = S_q$ at a relative velocity of $u_r = 0.1\,\text{m}\,\text{s}^{-1}$.

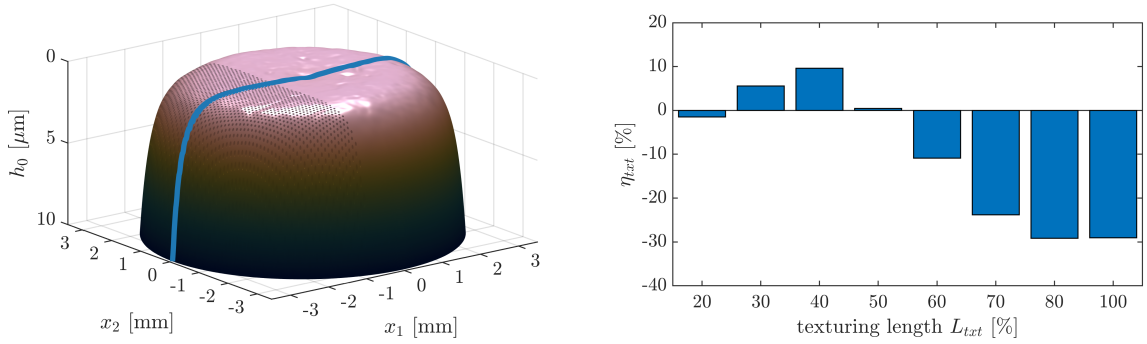

(a) Distribution of the macroscopic gap height h_0 in the case of a texturing length of $L_{txt} = 40\%$. The center line of the pin is marked in blue.

(b) Texture efficiency η_{txt} for different texturing lengths L_{txt}.

Figure 6.7: Effect of the texturing length L_{txt} for a texturing width of $W_{txt} = 100\%$, texturing density of $\rho_{txt} = 20\%$, dimple diameter of $d_{dpl} = 40\,\mu\text{m}$ and dimple depth of $h_{dpl} = S_q$ at a relative velocity of $u_r = 0.1\,\text{m}\,\text{s}^{-1}$.

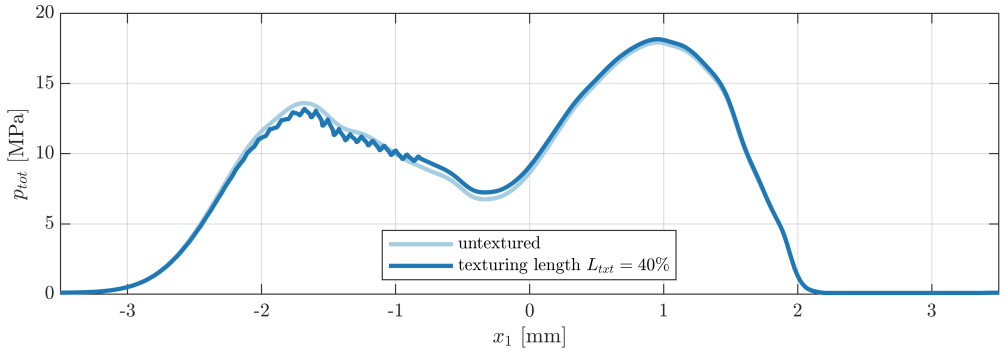

(a)

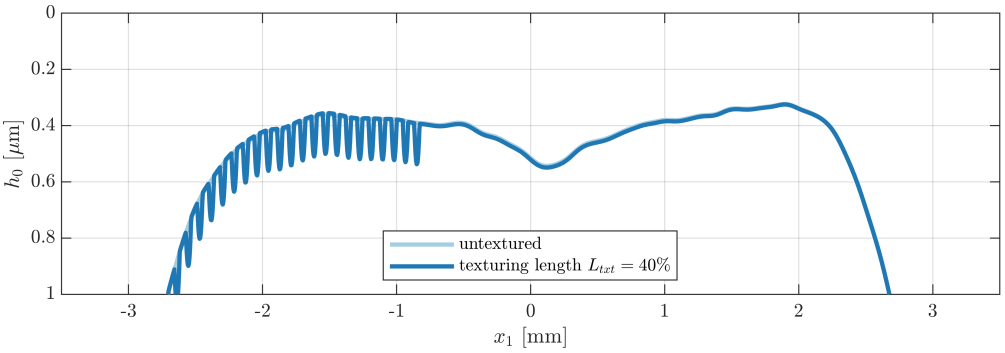

(b)

Figure 6.8: (a) Total pressure p_{tot} and (b) macroscopic gap height h_0 along the center line for an untextured pin and a textured one with a texturing length of $L_{txt} = 40\%$, texturing width of $W_{txt} = 100\%$, texturing density of $\rho_{txt} = 20\%$, dimple diameter of $d_{dpl} = 40\,\mu\text{m}$ and dimple depth of $h_{dpl} = S_q$ at a relative velocity of $u_r = 0.1\,\text{m}\,\text{s}^{-1}$.

The first step of the actual parametric study is to determine the texturing length L_{txt} which produces the highest texture efficiency. Figure 6.7a exemplary shows the distribution of the macroscopic gap height h_0 in the case of a texturing length of $L_{txt} = 40\%$ and a texturing width of $W_{txt} = 100\%$. Figure 6.7b shows the texture efficiencies when L_{txt} is varied from 20% to 100%. The results show that friction reduction can only be achieved for a texturing length between 30 and 50%. All of the other configurations produce negative texture efficiencies which is equivalent to a friction increase due to the surface

textures. The highest texture efficiency is obtained at $L_{txt} = 40\%$. The total pressure distributions and macroscopic gap height along the center line of the pin are displayed in Figure 6.8 for the cases of an untextured pin and $L_{txt} = 40\%$. It shows that the friction reduction comes along with a pressure reduction in the dimpled area and a slight pressure increase in the following downstream region. It is furthermore notable that the optimum texturing length stops just before the diverging part of the gap which is introduced by the dent at the center of the pin.

As a second step, the texturing width W_{txt} is as varied for a fixed texturing length of $L_{txt} = 40\%$. The macroscopic gap height distribution h_0 is visualized in Figure 6.9a for the exemplary case of a texturing width of $W_{txt} = 40\%$. The texture efficiencies η_{txt} are displayed in Figure 6.9b for texturing widths in the range of 20 to 100%. The highest efficiency is found for a texturing width of $W_{txt} = 40\%$. The almost constant texture efficiency for higher texturing widths suggests that surface textures outside of a width of $W_{txt} = 60\%$ are irrelevant to the friction behaviour. This is reasonable because the associated additional textures are on the very rim of the pin and outside of the tribological contact.

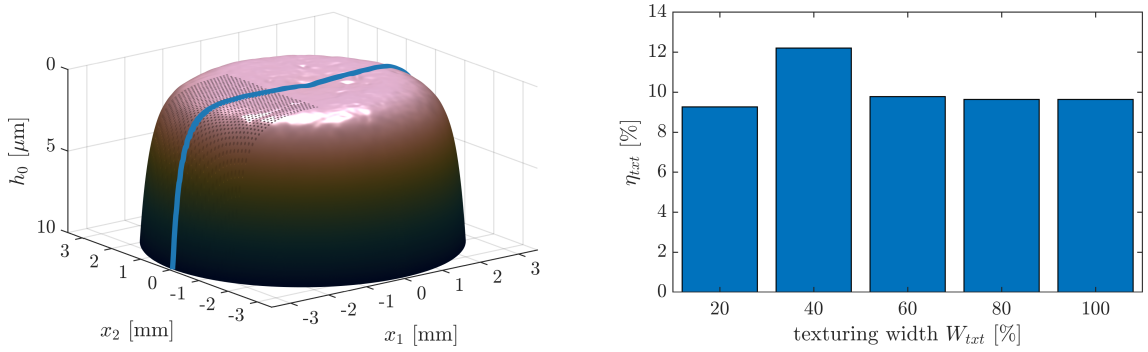

(a) Distribution of the macroscopic gap height h_0 in the case of a texturing width of $W_{txt} = 40\%$. The center line of the pin is marked in blue.

(b) Texture efficiency η_{txt} for different texturing widths W_{txt}.

Figure 6.9: Effect of the texturing width W_{txt} for a texturing length of $L_{txt} = 40\%$, texturing density of $\rho_{txt} = 20\%$, dimple diameter of $d_{dpl} = 40\,\mu\text{m}$ and dimple depth of $h_{dpl} = S_q$ at a relative velocity of $u_r = 0.1\,\text{m}\,\text{s}^{-1}$.

Next, the texturing density ρ_{txt} is varied while the texturing length and width are kept at $L_{txt} = 40\%$ and $W_{txt} = 40\%$. Figure 6.10a exemplary shows the distribution of the macroscopic gap height h_0 in the case of a texturing density of $\rho_{txt} = 40\%$ while Figure 6.10 shows the texture efficiency for different texturing densities in a range from 5 to 50%. The results show that the texture efficiency increases with the texturing density. The reason is that the geometry of the textured pin is approaching a step-like shape which is known to be the shape that produces the maximum pressure build-up [23, 36]. This explanation is supported by the total pressure profiles and macroscopic gap heights displayed in Figure 6.11. With an increasing texturing density, the pressure in the textured region is decreased while the subsequent downstream pressure rises, thus shifting the pressure profile towards the profile that can be obtained by a Rayleigh step [41, Ch. 8.6]. This behaviour is observed in a similar manner in the work of Codrignani *et al.*, where the adjoint method is employed to find the pin shape that maximizes the hydrodynamic lift [20]. At the same time, Figure 6.11b shows that the gap height is slightly increased downstream of the textured areas. The reason is that due to the load balance equation, the integral of the pressure profile is required to be the same for all of the considered profiles. Consequently, a more potent pressure profile does not lead to a higher average of the total pressure, but instead to a slightly larger macroscopic rigid body displacement $h_{0,d}$. This causes an increase of the macroscopic rigid body displacement of approximately $4\,\text{nm}$ for $\rho_{txt} = 40\%$ compared to the untextured case.

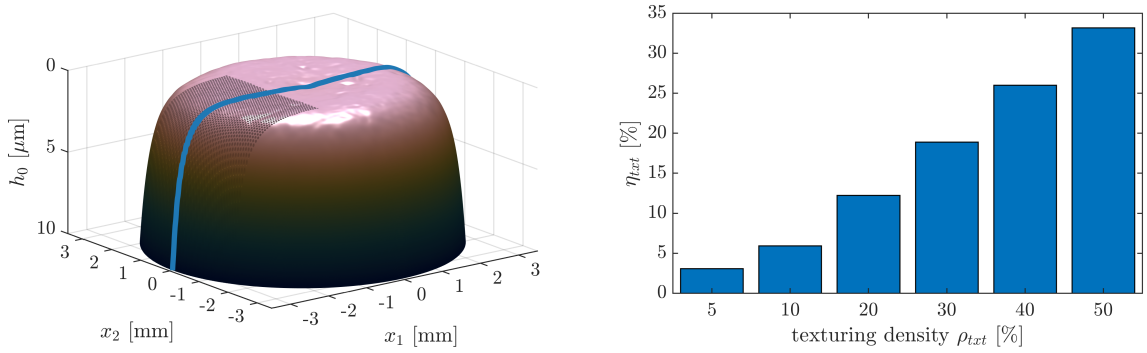

(a) Distribution of the macroscopic gap height h_0 in the case of a texturing density of $\rho_{txt} = 40\%$. The center line of the pin is marked in blue.

(b) Texture efficiency η_{txt} for different texturing densities ρ_{txt}.

Figure 6.10: Effect of the texturing density ρ_{txt} for a texturing length of $L_{txt} = 40\%$, texturing width of $W_{txt} = 40\%$, dimple diameter of $d_{dpl} = 40\,\mu\text{m}$ and dimple depth of $h_{dpl} = S_q$ at a relative velocity of $u_r = 0.1\,\text{m}\,\text{s}^{-1}$.

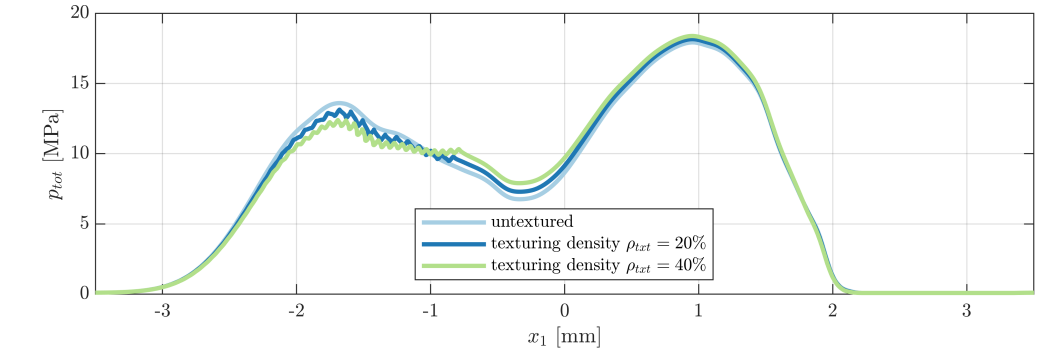

(a)

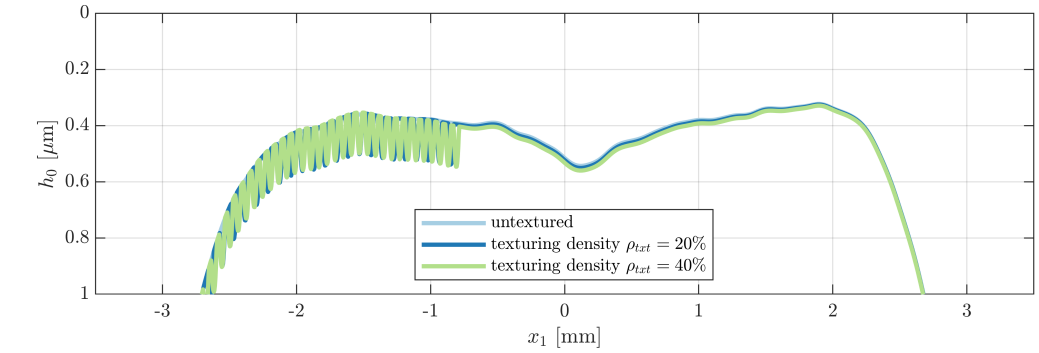

(b)

Figure 6.11: (a) Total pressure p_{tot} and (b) macroscopic gap height h_0 along the center line for an untextured pin and a textured one with a texturing length of $L_{txt} = 40\%$, texturing width of $W_{txt} = 40\%$, texturing densities of $\rho_{txt} = 20\%$ and $\rho_{txt} = 40\%$, dimple diameter of $d_{dpl} = 40\,\mu\text{m}$ and dimple depth of $h_{dpl} = S_q$ at a relative velocity of $u_r = 0.1\,\text{m}\,\text{s}^{-1}$.

As a next step, the dimple diameter d_{dpl} is varied at a constant dimple depth of $h_{dpl} = S_q$, texturing length of $L_{txt} = 40\%$, texturing width of $W_{txt} = 40\%$ and texturing density of $\rho_{txt} = 20\%$. In the exemplary case of $d_{dpl} = 160\,\mu\text{m}$, the resulting macroscopic gap height profile is displayed in Figure 6.12a. The texture efficiency is visualized in Figure 6.12 for dimple diameters between 40 and $400\,\mu\text{m}$ and slightly increases towards $\eta_{txt} = 12.21\%$ for a decreasing dimple diameter. Exemplary total pressure profiles are provided in Figure 6.13. They show that for a decreasing dimple diameter, the pressure pro-

files converge towards a solution that is not identical to the total pressure profile of the untextured pin. Such a behaviour of the Reynolds equation is also observed in the literature for wavy surfaces whose wavelength is decreased while the amplitude is kept constant [9]. Moreover, this can even be exploited to model roughness over the complete computational domain with the homogenization theory because this approach can provide the converged pressure profile [5]. In case of the textured pin, it is thus concluded that the limit of the texture efficiency is reasonably represented by a dimple diameter of $40\,\mu\mathrm{m}$.

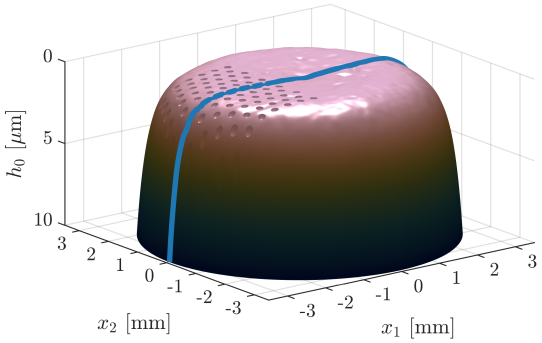

(a) Distribution of the macroscopic gap height h_0 in the case of a dimple diameter of $d_{dpl} = 160\,\mu\mathrm{m}$. The center line of the pin is marked in blue.

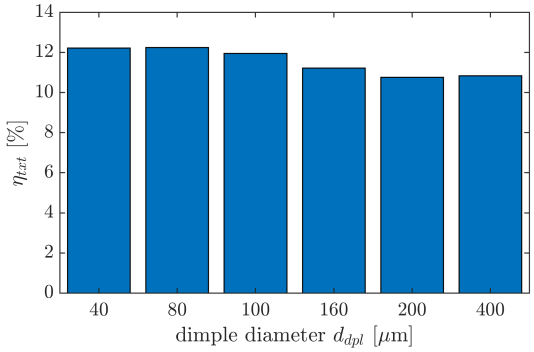

(b) Texture efficiency η_{txt} for different dimple diameters d_{dpl}.

Figure 6.12: Effect of the dimple diameter d_{dpl} for a texturing length of $L_{txt} = 40\%$, texturing width of $W_{txt} = 40\%$, texturing density of $\rho_{txt} = 20\%$ and dimple depth of $h_{dpl} = S_q$ at a relative velocity of $u_r = 0.1\,\mathrm{m\,s^{-1}}$.

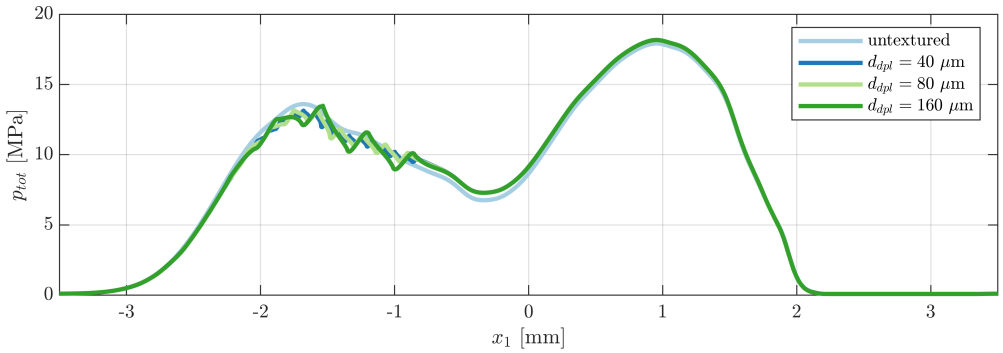

Figure 6.13: Total pressure p_{tot} along the center line for an untextured pin and a textured one with a texturing length of $L_{txt} = 40\%$, texturing width of $W_{txt} = 40\%$, texturing density of $\rho_{txt} = 20\%$, dimple diameters of $d_{dpl} = 40\,\mu\mathrm{m}$, $d_{dpl} = 80\,\mu\mathrm{m}$ and $d_{dpl} = 160\,\mu\mathrm{m}$ and dimple depth of $h_{dpl} = S_q$ at a relative velocity of $u_r = 0.1\,\mathrm{m\,s^{-1}}$.

As the last parameter, the dimple depth h_{dpl} is varied at a constant texturing length of $L_{txt} = 40\%$, texturing width of $W_{txt} = 40\%$, texturing density of $\rho_{txt} = 20\%$ and dimple diameter of $d_{dpl} = 40\,\mu\mathrm{m}$. The resulting texture efficiencies are shown in Figure 6.14, where the dimple depth h_{dpl} is expressed in multiples of the roughness root-mean-square S_q. The results indicate that the highest texture efficiency is obtained in the vicinity of $h_{dpl} = 1.5S_q$. As shown earlier in Figure 6.11b, the minimum macroscopic gap height is also in the magnitude of $S_q = 145.7\,\mathrm{nm}$. This finally demonstrates that according to the underlying Reynolds equation, the optimum dimple depth to obtain the maximum hydrodynamic load carrying capacity in the mixed lubrication regime is of the same magnitude as the minimum gap height. This is consistent with an extrapolation of numerical literature results collected in the hydrody-

namic regime [19] and reasonable because the employed mixed lubrication solver also uses the Reynolds equation to determine the hydrodynamic load carrying capacity.

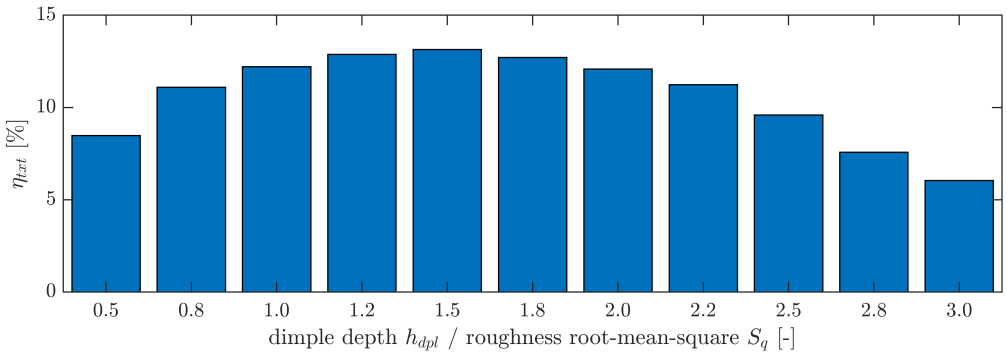

Figure 6.14: Texture efficiency η_{txt} for different dimple depths h_{dpl} at a texturing length of $L_{txt} = 40\%$, texturing width of $W_{txt} = 40\%$, texturing density of $\rho_{txt} = 20\%$, dimple diameter of $d_{dpl} = 40\,\mu\text{m}$ and a relative velocity of $u_r = 0.1\,\text{m}\,\text{s}^{-1}$.

The point of the Stribeck curve with the highest texture efficiency can be obtained by comparing the simulated Stribeck curves of an untextured pin and one with a texturing length of $L_{txt} = 40\%$, texturing width of $W_{txt} = 40\%$, texturing density of $\rho_{txt} = 20\%$, dimple diameter of $d_{dpl} = 40\,\mu\text{m}$ and dimple depth of $h_{dpl} = 1.5S_q$ in Figure 6.15a. The corresponding texture efficiency is displayed in Figure 6.15b and shows that the highest friction reduction is achieved at the onset of the mixed lubrication regime. From there, the texture efficiency decreases both for a progression into the hydrodynamic or towards the boundary lubrication regime.

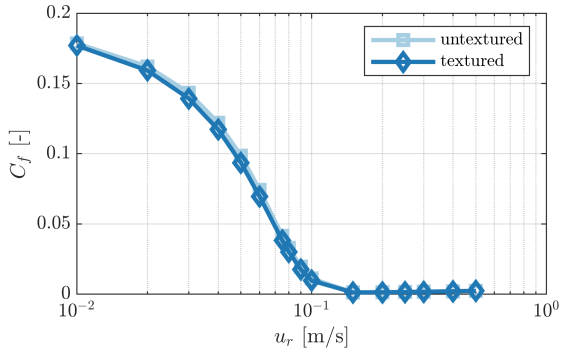

(a) Stribeck curve represented by the friction coefficient C_f as a function of relative velocity u_r.

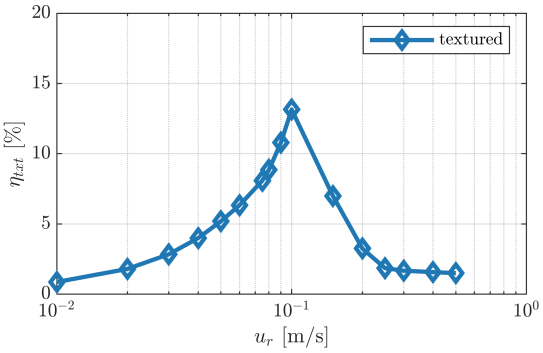

(b) Texture efficiency η_{txt} as a function of relative velocity u_r.

Figure 6.15: Comparison of an untextured pin and a textured one with a texturing length of $L_{txt} = 40\%$, texturing width of $W_{txt} = 40\%$, texturing density of $\rho_{txt} = 20\%$, dimple diameter of $d_{dpl} = 40\,\mu\text{m}$ and dimple depth of $h_{dpl} = 1.5S_q$.

Lastly, a dimple depth of $h_{dpl} = 4\,\mu\text{m}$ is simulated at a texturing width of $W_{txt} = 100\%$, texturing density of $\rho_{txt} = 10\%$, dimple diameter of $d_{dpl} = 40\,\mu\text{m}$ because this is a configuration that is also investigated in real-life experiments for fully textured pins [16, 79]. Figure 6.16 shows the texture efficiencies produced by simulations for different texturing lengths at a relative velocity of $u_r = 0.1\,\text{m}\,\text{s}^{-1}$. Converged results could only be obtained for texturing lengths up until $L_{txt} = 50\%$. This is because for larger texturing lengths, dimples are placed also in the cavitation region at the back of the pin's surface. Due to the dimple depth being much larger than the minimum macroscopic gap height, the cavity fraction changes drastically in this region and the solver is not able to deliver converged results anymore. Nonetheless

for the configurations with $L_{txt} \leq 50\%$, the obtained texture efficiency is always negative and steadily decreases with an increasing texturing length. The corresponding total pressure and macroscopic gap height profiles are visualized in Figure 6.17 for exemplary texturing lengths. They show that the surface textures mostly decrease the total pressure over the back half of the pin's surface. The resulting total pressure profile is less potent and can only sustain the applied normal load when the minimum gap height is decreased in comparison to the untextured surface, thus causing the friction increase in the mixed lubrication regime. The negative texture efficiency for the employed dimple depth is consistent with the trend observed for shallow dimples in Figure 6.14.

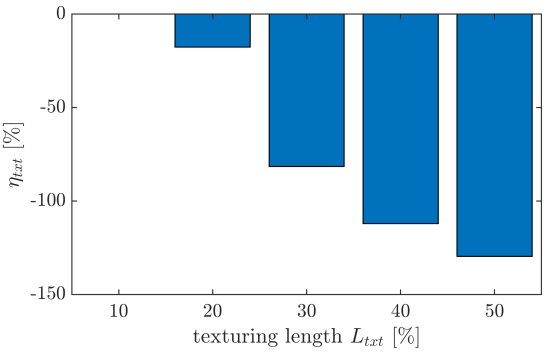

Figure 6.16: Texture efficiency η_{txt} for different texturing lengths L_{txt} at a texturing width of $W_{txt} = 100\%$, texturing density of $\rho_{txt} = 10\%$, dimple diameter of $d_{dpl} = 40\,\mu\text{m}$, dimple depth of $h_{dpl} = 4\,\mu\text{m}$ and a relative velocity of $u_r = 0.1\,\text{m}\,\text{s}^{-1}$.

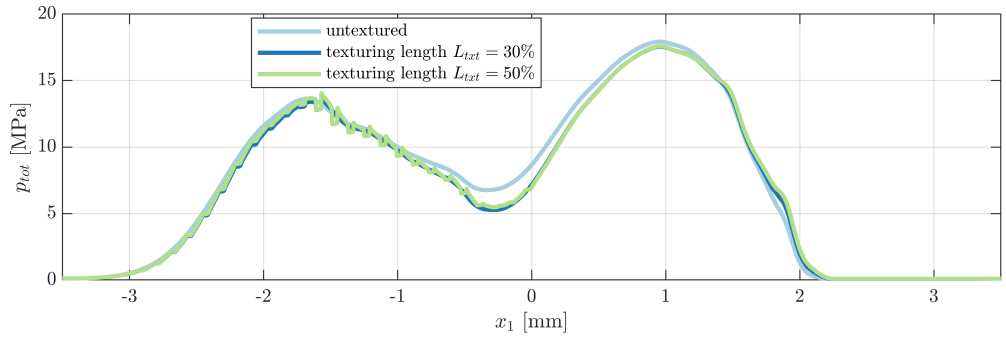

(a)

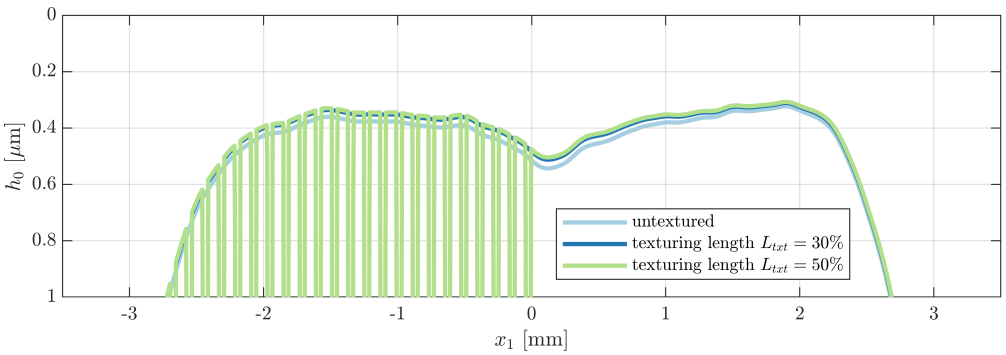

(b)

Figure 6.17: (a) Total pressure p_{tot} and (b) macroscopic gap height h_0 along the center line for different texturing lengths L_{txt} at a texturing width of $W_{txt} = 100\%$, texturing density of $\rho_{txt} = 10\%$, dimple diameter of $d_{dpl} = 40\,\mu\text{m}$ and dimple depth of $h_{dpl} = 4\,\mu\text{m}$ at a relative velocity of $u_r = 0.1\,\text{m}\,\text{s}^{-1}$.

In contrast to the simulation results, the Stribeck curves and texture efficiencies obtained in real-life pin-on-disk experiments of fully textured pins with a dimple diameter of $d_{dpl} = 40\,\mu\text{m}$ and dimple depth of $h_{dpl} = 4\,\mu\text{m}$ are shown in Figure 6.18. The data was acquired by Gerda Vaitkunaite at IAM-ZM and is solely used as reference within this thesis. The curves show that a significant friction reduction between 29.16 and 84.71% can be consistently obtained in the mixed lubrication regime. This completely contradicts the simulation results in regard of the texturing length and and dimple depth that can result in a positive texture efficiency.

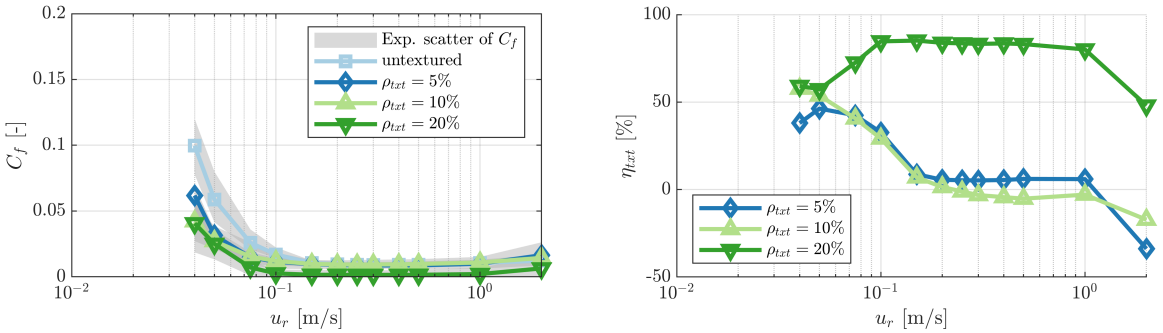

(a) Stribeck curve represented by the friction coefficient C_f as a function of relative velocity u_r.

(b) Texture efficiency η_{txt} as a function of relative velocity u_r.

Figure 6.18: Data sets obtained by Gerda Vaitkunaite in experiments at IAM-ZM for different texturing densities ρ_{txt} at a texturing length of $L_{txt} = 100\%$, texturing width of $W_{txt} = 100\%$, dimple diameter of $d_{dpl} = 40\,\mu\text{m}$ and dimple depth of $h_{dpl} = 4\,\mu\text{m}$.

6.5 Discussion

In summary, the numerical results of this chapter are consistent with an extrapolation of favourable dimple dimensions from the hydrodynamic [19] to the mixed lubrication regime. This is reasonable because in both studies, the Reynolds equation is used to determine the pressure build-up of the fluid. The conclusion is that according to the Reynolds equation, surface textures can only provide more potent pressure profiles for dimple depths in the magnitude of the minimum gap height. Furthermore, the textures have to be applied only at certain parts within the inlet of the lubricated contact. This causes a reduction of the total pressure distribution in the inlet and an increase in the outlet, thus approximating the ideal distribution obtained by a Rayleigh step. If additionally an imposed normal load is prescribed, the more potent pressure profile leads to a larger rigid body displacement of the contacting surfaces. Such behaviour had generally been known in the hydrodynamic regime [36] and it was shown in the course of this work that it first also holds in the mixed lubrication regime and second causes friction reduction by decreasing the amount of roughness asperity contact.

At the same time, the significant friction reduction in the mixed lubrication regime obtained in real-life pin-on-disk experiments of fully textured pins and large dimple depths cannot even remotely be replicated by the performed simulations. For texturing lengths that approximate fully textured pins, none of the simulations resulted in a more potent pressure profile. In fact, the load carrying capacity gets worse the more of the rear side of the pin is textured which is accompanied by higher friction in the mixed lubrication regime. The same is observed when the dimple depths become significantly deeper than the roughness height.

The obtained results indicate that the employed model does not seem to incorporate the effect that is actually responsible for the friction reduction in the mixed lubrication regime of the experiments. Thus, several aspects of the current model are discussed in the following to estimate whether a correspond-

ing improvement of the model could potentially lead to an increase in the load carrying capacity and consequently lead to a reduction of the friction in the mixed lubrication regime.

As a first hypothesis, the virtual macroscopic geometry might not be replicated properly because the pin inclination is not necessarily fixed after the pin levelling. It could be possible that the pin changes its inclination during the Stribeck curve acquisition according to the total pressure profile even though the pin holder itself is not lifted from the base plate. In this case however, the friction in the contact between pin holder and base plate acts as a resistance against further rotations of the pin. Since the exact magnitude of this resistance is difficult to determine it is not possible to completely model the occurring torque balance and thus the pin inclination during the Stribeck curve acquisition. Nonetheless, even if the inclination of the pin changes, the knowledge from the literature [23, 36] about the hydrodynamic load carrying capacity of textured inclined contacts rather suggests that this will cause a decrease in texture efficiency and will not change any of the findings considering fully textured pins or dimple depths significantly larger than the roughness height.

Moreover, the macroscopic gap height is influenced by elastic deformation. In the current work, elastic deformation is computed according to the elastic half-space theory because it can be efficiently incorporated into the solver via FFT. While the assumption of a half-space shape is remotely met by the disk, it does not correspond to the geometry of the pin, thus resulting in an incorrect computation of the surface deformation for the applied total pressure. The validity of the half-space assumption was for example investigated by Zhang *et al.* [95] in the context of heavily loaded roller bearings. They concluded that under EHL conditions with non-conformal contact shapes, the elastic half-space assumption leads to notable errors in the simulated deformation and pressure distributions. Nonetheless, it has to be kept in mind that the elastic deformations are significantly smaller in a pin-on-disk tribometer because of the conformal contact shape and much smaller loads. For a pin-on-disk tribometer, an FEM guided correction was applied to the deformation kernel function of the elastic-half space in a preliminary work by [Hansen et al., 2020]. There, it was shown that for a typical pressure profile as it occurs in a pin-on-disk tribometer, errors in the deformation of the pin are mostly caused by a constant offset. At the same time it was shown that when Stribeck curves are simulated for constant imposed normal loads, this offset is automatically compensated by an adjustment of the rigid body displacement of the contacting surfaces. Thus, the resulting macroscopic gap height distribution is almost the same in cases with or without correction of the kernel function and the subsequent differences of the final Stribeck curves are negligible. It can therefore be concluded that a more accurate deformation model is unlikely to resolve the observed disagreement between textured experiments and numerical simulations.

Furthermore, the employed model assumes constant dynamic viscosity and density of the fluid over the gap height. Instead, it is also possible to use a generalized version of the Reynolds equation [69] which can take changes due to shear thinning or temperature variations into account. On the downside, these models additionally require a discretization along the gap height, which increases the computational complexity of the problem. On the other hand, this would allow to consider decreases in the effective viscosity due to shear thinning, which in turn would decrease the load carrying capacity of the flow. In combination with surface textures, it is theoretically imaginable that the shear stresses drop within the textures, thus causing the effective viscosity within the textures to be higher than in untextured areas. This might also lead to higher load carrying capacities for textured profiles. Still, such an increase would also have to compensate the enormous load carrying decrease due to the less efficient gap geometry that was demonstrated in Figure 6.16. While this seems unrealistic, it would also only come into effect if significant shear thinning actually occurs on the macroscopic scale of the simulation. Therefore, an

a-priory way of testing the applicability of this hypothesis in the future would be to first check whether a limiting shear stress is remotely reached at any point within the gap.

Similarly, temperature variations over the whole computational domain might require the additional consideration of the thermal energy conservation equation [38]. This is not only due to dissipation within the fluid itself, but especially due to the heating of the fluid because of the dissipation caused by asperity contact in the mixed lubrication region. Therefore, the textures could potentially act as low temperature reservoirs that increase the dynamic viscosity also downstream of the texture within the mixed lubrication contact. While it cannot be directly ruled out at this point that this might result in a higher load carrying capacity when compared to an untextured surface, this effect would also have to overcompensate the large load carrying decrease numerically observed for the isothermal system. As a first step in the future, the applicability of this hypothesis could be roughly checked by estimating the temperature rise in the fluid and consequently any changes in the effective dynamic viscosity. This could be further facilitated by assuming isothermal or adiabatic surfaces as an initial step.

Moreover, the current model neglects any inertia effects. These can be taken into account either with a correction of the Reynolds equation [6] or by directly solving the full Navier-Stokes equations. While results in the literature [22] suggest that the load carrying capacity can be slightly increased by considering inertia, this is only the case for dimple depths in the magnitude of the minimum gap height. Deeper dimples will result in even lower load carrying capacities if inertia is considered. For this reason, it is not expected that additional modelling of inertia will lead to a better agreement of the simulation results with the experiments.

Additionally, the question might be raised whether the employed JFO cavitation model is not applicable because cavitation does not necessarily occur uniformly over the gap height. For example in the work of Brajdic-Mitidieri *et al.* [15], this is shown to happen along with first cavitation already occurring upstream of the dimple. In their considered geometry, cavitation occurs at some parts along the gap height, while other parts are still fully lubricated and allow a pressure build-up. However, this only happens when the untextured part of the geometry is not able to generate any significant pressure build-up on its own. Furthermore, the pressure build-up due to the texture is negligible compared to the increase that can be obtained when the gap inclination is slightly increased. Since for a pin-on-disk tribometer, the untextured pin is already able to create a significant hydrodynamic lift on its own, these cavitation related considerations are likely not applicable. Thus, a computational fluid dynamics (CFD) simulation with a more sophisticated cavitation model is not expected to deliver higher load carrying capacities for fully textured pins and deep dimples.

The inability to simulate any additional load carrying capacity for fully textured pins and dimple depths significantly larger than the minimum gap height eventually leaves room for another theory: the experimentally observed friction reduction in the mixed lubrication regime might not be caused at all by additional surface separation due to an increased hydrodynamic lift, but rather by a direct decrease of the shear stresses occurring at surface contact. This friction reduction is not expected to happen due to the formation of tribofilms [10, 86] because of the absence of any friction modifiers or additives in the employed base oil. Instead, the textures might simply act as lubricant reservoirs [36] that prevent local dry-out or starvation downstream of the textures. This might reduce the amount of dry friction occurring at asperity contact by supplying a thin film of lubricant. For fully textured surfaces, the corresponding friction reduction could be large enough to overcompensate the friction increase due to the lower load carrying capacity. Considering future simulations, this idea could be tested by enforcing lower boundary friction coefficients along a certain length downstream of the textures.

This discussion can be summarized as follows: the friction reduction observed in the mixed lubrication regime of pin-on-disk tribometer experiments with fully textured contacts cannot be replicated with the current numerical model. Thus, the initial idea that this friction reduction is due to an additional hydrodynamic lift cannot be confirmed since none of the simulations resulted in a more potent pressure profile for fully textured surfaces, especially for dimples that are significantly deeper than the roughness height. This could be due to two reasons. On the one hand, the employed model could be too simplified and thus not able to replicate the relevant mechanism that is responsible for the additional hydrodynamic lift. If this is indeed the case, then it can be deduced that the isothermal Reynolds equation is not an applicable tool to investigate real-life surface textures in mixed lubrication. While several shortcomings of the employed model and possible improvements were discussed, there is no clear indication that a more sophisticated model will resolve this issue. On the other hand, this could also mean that the friction reduction is actually not related to additional hydrodynamic lift at all, but instead only to a direct reduction of the boundary friction that occurs in the mixed lubrication regime. In other words: the friction reduction is not caused by less surface contact due to larger surface separation but rather by lower contact friction that occurs at roughness asperity contact when surface textures are present. The phenomenon behind this might be that surface textures can supply just enough lubrication to prevent a downstream dry-out. This does not result in any additional hydrodynamic lift but rather decreases the friction occurring at the contact of roughness asperities by resulting in boundary instead of dry friction. In this case, models based on the Reynolds equation might be suitable to determine the load carrying capacity of the lubricant but need to be extended by a more sophisticated modelling of the surface contact friction.

7 Conclusion and Outlook

Due to its significant potential in reducing friction losses, surface texturing has received great attention in the tribology community over the recent decades. Over time, several general mechanisms have been suggested in the literature to explain the phenomenon that is responsible for the friction reduction. While in some cases it has been possible to support the theory of fluid pressure enhancement in the hydrodynamic lubrication regime, there is still no rigorous explanation for the experimentally observed friction reduction in the mixed lubrication regime of fully textured contacts. On the contrary, an extrapolation of favourable dimple arrangements from available numerical results in the hydrodynamic regime to mixed lubrication even suggests an increase in friction for the fully textured surfaces used in experiments. Since the clarification of this inconsistency is a requirement for the applicability of numerical surface texturing studies to the mixed lubrication regime, the current work aims at resolving this contradiction with a numerical model based on the the Reynolds equation. The fundamental research question addressed in this thesis was whether simulations based on the Reynolds equation can be employed to investigate the experimentally observed friction reduction due to surface texturing in the mixed lubrication regime. Incorporating three publications by [Hansen et al., 2020], [Hansen et al., 2022] and [Hansen et al., 2023], this research question was approached with the following steps.

First, the fundamental model of a generalized lubricated gap was established. It considers the lubricant with the isothermal Reynolds equation, takes cavitation with the JFO model into account and incorporates piezoviscosity and compressibility. Furthermore, the gap deformation due to the acting pressures is modelled with the elastic half-space theory. Finally, the hydrodynamics are coupled in a two-scale model with the surface contact by consideration of averaged roughness effects on the fluid and contact pressure. Together with the associated equations for the tangential stresses of the hydrodynamics and the surface contact, a closed system of equations is constructed that allows the determination of the friction coefficient in the boundary, mixed and hydrodynamic lubrication regime.

Subsequently, two novel solvers were introduced that allow the computation of the solutions of the equations presented. The first one is the EHL-FBNS solver, which only provides the solution in the hydrodynamic regime when no surface contact occurs. It was used to determine the influence of the discretization scheme when surface textures are present in the gap geometry. By comparing numerical and analytical results for a convergent slider with rectangular pocket, it was found that a first order discretization scheme of the Couette term in the Reynolds equation provides more accurate results than higher order discretization schemes when discontinuities are present in the gap height. Further comparison with numerical results in the literature suggested that this is also the case when there are no discontinuities in the gap height, but only in the solution of the cavity fraction due to full-film reformulation. Independently of the discretization scheme, it was additionally found that the elasticity of the surfaces has a significant effect on the load carrying capacity and should therefore not be neglected.

Moreover, the EHL-FBNS solver was employed to simulate a single texture which is passing transiently through the EHL contact of a ball-on-disk tribometer. Being impossible to perform with previously existing solvers, simulations of the same dimple dimensions that were used in the reference experiments finally became realizable with the EHL-FBNS solver. The comparison of the gap height obtained with numerical simulations and experimental measurements from the literature confirmed the benefit

of employing lower order discretizations of the Couette term in the presence of gap height discontinuities. It was shown that in such cases, higher order schemes do not only converge more slowly but also to completely different and non-physical solutions. The good agreement between the experimentally measured gap height distributions and simulations with first order discretizations of the Couette term eventually allowed to validate the EHL-FBNS solver as a tool for studying deep textures with strongly discontinuous shapes.

As an extension to the first solver, the HMEHL-FBNS solver was subsequently incorporated in the digital twin of a pin-on-disk tribometer. Macro- and microscopic topography measurements of untextured post-test pin and disk specimens were used in order to virtually replicate the gap geometry of real-life experiments. The evaluation of the deviations in the Stribeck curve showed that filtering of the macroscopic topographies is an essential calibration step to obtain a representative macroscopic geometry. Furthermore, the Stribeck curve produced by the digital twin was shown to be highly sensitive to the employed roughness patch. At the same time, averaging the influence factors obtained from several microscopic roughness patches resulted in very good agreement with the Stribeck curves of the real-life experiments. Moreover, the Hersey number of a pin-on-disk tribometer was derived as $\mathcal{H} = \mu_0 UD/F_{N,imp}$ and used to validate the Stribeck curves of the digital twin at oil temperatures of 24 and 50 °C. This further demonstrated that the Stribeck curves, and thus the lubricant's load carrying capacity, of both the simulations and experiments scale consistently with the oil's dynamic viscosity. Lastly, it was shown that averaging over only a small amount of macroscopic pin topographies and microscopic roughness patches is sufficient to obtain a digital twin that represents the general friction behaviour of different sample pairings and temperatures.

As a last step, the developed digital twin of the pin-on-disk tribometer was used to analyze the effect of surface textures on top of the pin. The study showed that the developed two-scale model predicts friction reduction only when the inlet region of the lubricated contact is textured with dimples whose depth is in the magnitude of the minimum gap height. In the mixed lubrication regime, the roughness root-mean-square value S_q is a representative measure of the minimum gap height and the highest friction reduction was obtained with a dimple depth of $d_{dpl} = 1.5S_q$. These results are consistent with an extrapolation from literature results that have been obtained numerically in the hydrodynamic regime. Thus, the present thesis shows that the scaling laws obtained in the hydrodynamic regime are also replicated by numerical simulations in the mixed lubrication regime. This is reasonable because both approaches compute the load carrying capacity of the lubricant using the Reynolds equation. In the case of pin-on-disk tribometers that operate under an imposed normal load, the higher load carrying capacity eventually results in a greater separation of the surfaces. This in turn reduces the amount of surface contact on the roughness scale, which finally leads to a lower friction coefficient in the mixed lubrication regime. Summarizing, the current study confirmed the literature knowledge from the hydrodynamic regime and extended it to mixed lubrication that according to the numerics, the highest load carrying capacity and hence the lowest friction can be achieved by approximating a Rayleigh step.

While these results are consistent from a numerical point of view, a comparison with real-life experiments using fully textured pins demonstrated that the isothermal Reynolds equation is not able to reproduce the surface texture induced friction reduction in mixed lubrication. Any simulation that approached fully textured dimple configurations always resulted in a friction increase, especially for dimples much deeper than S_q. The experiments, on the other hand, are able the demonstrate a reduction in friction also for these cases. One reason for this might be that the model is incomplete and is thus missing the physical mechanism that actually causes the friction reduction. While the improvement of several aspects of the model was discussed, only the additional modelling of shear thinning or thermal dissipation were evaluated as potentially having a positive effect on the load carrying capacity when surface textures are present. At the same time, these effects would also have to overcome the numerically already observed highly detrimental effects which again limit their potential for friction reduction. Therefore, with respect to the originally posed research question, the present work strongly indicates that simulations based on the Reynolds equation are not suitable for investigating the experimentally observed friction reduction due to surface texturing in the mixed lubrication regime.

This conclusion, however, is only valid under the prerequisite that the friction reduction in the mixed lubrication regime is actually caused by a higher load carrying capacity, which is still not proven. With this in mind, an alternative theory was finally proposed: since fully textured surfaces do not appear to result in any increase of the load carrying capacity, the friction reduction in the mixed lubrication regime might not be related to any changes in the fluid pressure at all. Instead, the idea was suggested that textured surfaces only prevent local dry-outs of the tribological contact, but do not induce any increase in fluid pressure. Thus, they may result in a lower hydrodynamic load carrying capacity, but primarily cause a lower boundary friction coefficient downstream of the dimples, which overcompensates for the friction increase due to the additional surface contact. In order to evaluate this theory in future work, further development of a simulation code based on the Reynolds equation to incorporate a variable boundary friction coefficient downstream of surface textures might be a promising approach.

Bibliography

[1] A. Akchurin, R. Bosman, P. M. Lugt, and M. van Drogen. On a model for the prediction of the friction coefficient in mixed lubrication based on a load-sharing concept with measured surface roughness. *Tribology letters*, 59(1):19, 2015.

[2] Q. Allen and B. Raeymaekers. Surface texturing of prosthetic hip implant bearing surfaces: a review. *Journal of Tribology*, 143(4), 2021.

[3] A. Almqvist, J. Fabricius, A. Spencer, and P. Wall. Similarities and Differences Between the Flow Factor Method by Patir and Cheng and Homogenization. *Journal of Tribology*, 133(3):031702, 2011.

[4] A. Almqvist, R. Larsson, and P. Wall. The homogenization process of the time dependent Reynolds equation describing compressible liquid flow. *Tribologia: Finnish Journal of Tribology*, 26(4):30–44, 2007.

[5] A. Almqvist and P. Wall. Homogenization of the Reynolds Equation. In Q. J. Wang and Y.-W. Chung, editors, *Encyclopedia of Tribology*, pages 1685–1689. Springer, New York, Heidelberg, Dordrecht, London, 2013.

[6] M. Arghir, A. Alsayed, and D. Nicolas. The finite volume solution of the Reynolds equation of lubrication with film discontinuities. *International Journal of Mechanical Sciences*, 44(10):2119–2132, 2002.

[7] R. Ausas, P. Ragot, J. Leiva, M. Jai, G. Bayada, and G. C. Buscaglia. The Impact of the Cavitation Model in the Analysis of Microtextured Lubricated Journal Bearings. *Journal of Tribology*, 129(4):868–875, 2007.

[8] D. Bartel. *Simulation von Tribosystemen*. Vieweg+Teubner, Wiesbaden, 2010.

[9] G. Bayada, S. Martin, and C. Vázquez. An Average Flow Model of the Reynolds Roughness Including a Mass-Flow Preserving Cavitation Model. *Journal of Tribology*, 127(4):793, 2005.

[10] D. Berman and A. Erdemir. Achieving Ultralow Friction and Wear by Tribocatalysis: Enabled by In-Operando Formation of Nanocarbon Films. *ACS nano*, 15(12):18865–18879, 2021.

[11] L. Bertocchi, D. Dini, M. Giacopini, M. T. Fowell, and A. Baldini. Fluid film lubrication in the presence of cavitation: a mass-conserving two-dimensional formulation for compressible, piezo-viscous and non-Newtonian fluids. *Tribology International*, 67:61–71, 2013.

[12] A. Bertram and R. Glüge. *Solid mechanics*. Springer, Cham, 2015.

[13] L. Bobach, D. Bartel, R. Beilicke, J. Mayer, K. Michaelis, K. Stahl, S. Bachmann, J. Schnagl, and H. Ziegele. Reduction in EHL Friction by a DLC Coating. *Tribology Letters*, 60(1):17, 2015.

[14] F. P. Bowden and D. Tabor. *The Friction and Lubrication of Solids*. At the Clarendon Press, Oxford, 2nd edition, 1954.

[15] P. Brajdic-Mitidieri, A. Gosman, E. Ioannides, and H. Spikes. CFD analysis of a low friction pocketed pad bearing. *Journal of Tribology*, 127(4):803–812, 2005.

[16] D. Braun, C. Greiner, J. Schneider, and P. Gumbsch. Efficiency of laser surface texturing in the reduction of friction under mixed lubrication. *Tribology International*, 77:142–147, 2014.

[17] M. Braun and W. Hannon. Cavitation formation and modelling for fluid film bearings: a review. *Proceedings of the Institution of Mechanical Engineers, Part J: Journal of Engineering Tribology*, 224(9):839–863, 2010.

[18] F. Chevalier, A. A. Lubrecht, P. M. E. Cann, F. Colin, and G. Dalmaz. Film Thickness in Starved EHL Point Contacts. *Journal of Tribology*, 120(1):126–133, 1998.

[19] A. Codrignani, B. Frohnapfel, F. Magagnato, P. Schreiber, J. Schneider, and P. Gumbsch. Numerical and experimental investigation of texture shape and position in the macroscopic contact. *Tribology International*, 122:46–57, 2018.

[20] A. Codrignani, D. Savio, L. Pastewka, B. Frohnapfel, and R. van Ostayen. Optimization of surface textures in hydrodynamic lubrication through the adjoint method. *Tribology International*, 148:106352, 2020.

[21] F. Crameri, G. E. Shephard, and P. J. Heron. The misuse of colour in science communication. *Nature communications*, 11(1):5444, 2020.

[22] S. Cupillard, S. Glavatskih, and M. Cervantes. Inertia effects in textured hydrodynamic contacts. *Proceedings of the Institution of Mechanical Engineers, Part J: Journal of Engineering Tribology*, 224(8):751–756, 2010.

[23] M. Dobrica, M. Fillon, M. Pascovici, and T. Cicone. Optimizing surface texture for hydrodynamic lubricated contacts using a mass-conserving numerical approach. *Proceedings of the Institution of Mechanical Engineers, Part J: Journal of Engineering Tribology*, 224(8):737–750, 2010.

[24] M. B. Dobrica and M. Fillon. About the validity of Reynolds equation and inertia effects in textured sliders of infinite width. *Proceedings of the Institution of Mechanical Engineers, Part J: Journal of Engineering Tribology*, 223(1):69–78, 2009.

[25] M. B. Dobrica and M. Fillon. About the validity of Reynolds equation and inertia effects in textured sliders of infinite width. *Proceedings of the Institution of Mechanical Engineers, Part J: Journal of Engineering Tribology*, 223(1):69–78, 2009.

[26] H. G. Elrod. A cavitation algorithm. *ASME Journal of Tribology*, 103:350–354, 1981.

[27] I. Etsion. State of the art in laser surface texturing. *Journal of Tribology*, 127(1):248–253, 2005.

[28] I. Etsion and L. Burstein. A model for mechanical seals with regular microsurface structure. *Tribology Transactions*, 39(3):677–683, 1996.

[29] I. Etsion, G. Halperin, V. Brizmer, and Y. Kligerman. Experimental investigation of laser surface textured parallel thrust bearings. *Tribology Letters*, 17(2):295–300, 2004.

[30] A. Ferretti. *Elastohydrodynamic analysis in engine lubricated contacts: managing of fluid cavitation and asperity contact problems*. PhD thesis, University of Modena and Reggio Emilia, 2018.

[31] A. Ferretti, M. Giacopini, L. N. Mastrandrea, and D. Dini. Investigation of the influence of different asperity contact models on the elastohydrodynamic analysis of a conrod small-end/piston pin coupling. *SAE International Journal of Engines*, 11(6):919–934, 2018.

[32] J. H. Ferziger, M. Perić, and R. L. Street. *Computational methods for fluid dynamics*. Springer, Cham, 4th edition, 2020.

[33] M. Fowell, A. V. Olver, A. D. Gosman, H. A. Spikes, and I. Pegg. Entrainment and Inlet Suction: Two Mechanisms of Hydrodynamic Lubrication in Textured Bearings. *Journal of Tribology*, 129(2):336–347, 11 2007.

[34] M. Giacopini, M. T. Fowell, D. Dini, and A. Strozzi. A Mass-Conserving Complementarity Formulation to Study Lubricant Films in the Presence of Cavitation. *Journal of Tribology*, 132(4), 09 2010. 041702.

[35] M. Grieves and J. Vickers. Digital twin: Mitigating unpredictable, undesirable emergent behavior in complex systems. In *Transdisciplinary perspectives on complex systems*, pages 85–113. Springer, 2017.

[36] D. Gropper, L. Wang, and T. J. Harvey. Hydrodynamic lubrication of textured surfaces: A review of modeling techniques and key findings. *Tribology International*, 94:509–529, 2016.

[37] P. G. Grützmacher, F. J. Profito, and A. Rosenkranz. Multi-scale surface texturing in tribologyâcurrent knowledge and future perspectives. *Lubricants*, 7(11):95, 2019.

[38] C. Gu, X. Meng, Y. Xie, and J. Fan. A thermal mixed lubrication model to study the textured ring/liner conjunction. *Tribology International*, 101:178–193, 2016.

[39] W. Habchi. *Finite element modeling of elastohydrodynamic lubrication problems*. Wiley Online Library, Chichester, 2018.

[40] D. B. Hamilton, J. A. Walowit, and C. M. Allen. A Theory of Lubrication by Microirregularities. *Journal of Basic Engineering*, 88(1):177–185, 03 1966.

[41] B. J. Hamrock, S. R. Schmid, and B. O. Jacobson. *Fundamentals of Fluid Film Lubrication*. Marcel Dekker, Inc., New York, Basel, 2004.

[42] Y. Henry, J. Bouyer, and M. Fillon. An experimental analysis of the hydrodynamic contribution of textured thrust bearings during steady-state operation: A comparison with the untextured parallel surface configuration. *Proceedings of the Institution of Mechanical Engineers, Part J: Journal of Engineering Tribology*, 229(4):362–375, 2015.

[43] M. D. Hersey. The laws of lubrication of horizontal journal bearings. *Journal of the Washington Academy of Sciences*, 4(19):542–552, 1914.

[44] K. Holmberg, P. Andersson, and A. Erdemir. Global energy consumption due to friction in passenger cars. *Tribology international*, 47:221–234, 2012.

[45] K. Holmberg and A. Erdemir. Influence of tribology on global energy consumption, costs and emissions. *Friction*, 5(3):263–284, 2017.

[46] K. Holmberg and A. Erdemir. The impact of tribology on energy use and CO2 emission globally and in combustion engine and electric cars. *Tribology International*, 135:389–396, 2019.

[47] B. Jakobsson and L. Floberg. The finite journal bearing, considering vaporization. *Transactions of Chalmers University of Technology*, 190, 1957.

[48] X. Jiang, D. Y. Hua, H. S. Cheng, X. Ai, and S. C. Lee. A Mixed Elastohydrodynamic Lubrication Model With Asperity Contact. *Journal of Tribology*, 121(3):481–491, 1999.

[49] K. L. Johnson. *Contact mechanics*. Cambridge University Press, Cambridge, 2004.

[50] D. Jones, C. Snider, A. Nassehi, J. Yon, and B. Hicks. Characterising the Digital Twin: A systematic literature review. *CIRP Journal of Manufacturing Science and Technology*, 29:36–52, 2020.

[51] H. P. Jost. Tribology - origin and future. *Wear*, 136(1):1–17, 1990.

[52] S. Kango, R. Sharma, and R. Pandey. Thermal analysis of microtextured journal bearing using non-Newtonian rheology of lubricant and JFO boundary conditions. *Tribology International*, 69:19–29, 2014.

[53] A. Kovalchenko, O. Ajayi, A. Erdemir, G. Fenske, and I. Etsion. The effect of laser texturing of steel surfaces and speed-load parameters on the transition of lubrication regime from boundary to hydrodynamic. *Tribology Transactions*, 47(2):299–307, 2004.

[54] A. Kovalchenko, O. Ajayi, A. Erdemir, G. Fenske, and I. Etsion. The effect of laser surface texturing on transitions in lubrication regimes during unidirectional sliding contact. *Tribology International*, 38(3):219–225, 2005.

[55] L. D. Landau and E. M. Lifshitz. *Theory of Elasticity*, volume 7. Pergamon Press, Oxford, 2nd edition, 1970.

[56] R. Larsson. Modelling the effect of surface roughness on lubrication in all regimes. *Tribology International*, 42(4):512–516, 2009.

[57] R. J. LeVeque. *Numerical methods for conservation laws*, volume 132. Birkhäuser, Basel, 2nd edition, 1992.

[58] S. Liu, L. Qiu, Z. Wang, and X. Chen. Influences of Iteration Details on Flow Continuities of Numerical solutions to Isothermal Elastohydrodynamic Lubrication with Micro-Cavitations. *Journal of Tribology*, 143(10):101601, 2020.

[59] P. Lu and R. J. Wood. Tribological performance of surface texturing in mechanical applications-A review. *Surface Topography: Metrology and Properties*, 8(4):043001, 2020.

[60] P. M. Lugt and G. E. Morales-Espejel. A review of elasto-hydrodynamic lubrication theory. *Tribology Transactions*, 54(3):470–496, 2011.

[61] M. Marian, A. Almqvist, A. Rosenkranz, and M. Fillon. Numerical micro-texture optimization for lubricated contacts-A critical discussion. *Friction*, 10(11):1772–1809, 2022.

[62] M. Marian, P. Grützmacher, A. Rosenkranz, S. Tremmel, F. Mücklich, and S. Wartzack. Designing surface textures for EHL point-contacts-transient 3d simulations, meta-modeling and experimental validation. *Tribology International*, 137:152–163, 2019.

[63] M. Marian, M. Weschta, S. Tremmel, and S. Wartzack. Simulation of microtextured surfaces in starved EHL contacts using commercial FE software. *Materials Performance and Characterization*, 6(2):165–181, 2017.

[64] L. Mourier, D. Mazuyer, A. Lubrecht, and C. Donnet. Transient increase of film thickness in micro-textured EHL contacts. *Tribology International*, 39(12):1745–1756, 2006.

[65] L. Oestringer and C. Proppe. On the fully coupled quasi-static equations for the thermoelastic halfspace. *Mechanics of Materials*, 177:104554, 2023.

[66] K.-O. Olsson. Cavitation in dynamically loaded bearings. *Transactions of Chalmers University of Technology*, 308, 1965.

[67] N. Patir and H. S. Cheng. An Average Flow Model for Determining Effects of Three-Dimensional Roughness on Partial Hydrodynamic Lubrication. *Journal of Lubrication Technology*, 100(1):12, 1978.

[68] N. Patir and H. S. Cheng. Application of Average Flow Model to Lubrication Between Rough Sliding Surfaces. *Journal of Lubrication Technology*, 101(2):220, 1979.

[69] Y. Peiran and W. Shizhu. A Generalized Reynolds Equation for Non-Newtonian Thermal Elastohydrodynamic Lubrication. *Journal of Tribology*, 112(4):631–636, 10 1990.

[70] R. Pohrt and Q. Li. Complete boundary element formulation for normal and tangential contact problems. *Physical Mesomechanics*, 17(4):334–340, 2014.

[71] I. Polonsky and L. M. Keer. A numerical method for solving rough contact problems based on the multi-level multi-summation and conjugate gradient techniques. *Wear*, 231(2):206–219, 1999.

[72] O. Reynolds. IV. On the theory of lubrication and its application to Mr. Beauchamp tower's experiments, including an experimental determination of the viscosity of olive oil. *Philosophical transactions of the Royal Society of London*, (177):157–234, 1886.

[73] A. Rosenkranz, A. Szurdak, C. Gachot, G. Hirt, and F. Muecklich. Friction reduction under mixed and full film EHL induced by hot micro-coined surface patterns. *Tribology International*, 95:290–297, 2016.

[74] F. Sahlin, R. Larsson, A. Almqvist, P. Lugt, and P. Marklund. A mixed lubrication model incorporating measured surface topography. Part 1: theory of flow factors. *Proceedings of the Institution of Mechanical Engineers, Part J: Journal of Engineering Tribology*, 224(4):335–351, 2009.

[75] P. Sainsot and A. A. Lubrecht. Efficient solution of the dry contact of rough surfaces: a comparison of fast Fourier transform and multigrid methods. *Proceedings of the Institution of Mechanical Engineers, Part J: Journal of Engineering Tribology*, 225(6):441–448, 2011.

[76] M. Scaraggi, F. P. Mezzapesa, G. Carbone, A. Ancona, D. Sorgente, and P. M. Lugarà. Minimize friction of lubricated laser-microtextured-surfaces by tuning microholes depth. *Tribology International*, 75:123–127, 2014.

[77] M. Scaraggi, F. P. Mezzapesa, G. Carbone, A. Ancona, and L. Tricarico. Friction properties of lubricated laser-microtextured-surfaces: an experimental study from boundary-to hydrodynamic-lubrication. *Tribology Letters*, 49:117–125, 2013.

[78] H. Schlichting. *Boundary-Layer Theory*. Springer, Berlin, Heidelberg, 9th edition, 2017.

[79] J. Schneider, D. Braun, and C. Greiner. Laser textured surfaces for mixed lubrication: influence of aspect ratio, textured area and dimple arrangement. *Lubricants*, 5(3):32, 2017.

[80] M. Singh, E. Fuenmayor, E. P. Hinchy, Y. Qiao, N. Murray, and D. Devine. Digital twin: Origin to future. *Applied System Innovation*, 4(2):36, 2021.

[81] A. Sommerfeld. Zur Theorie der Schmiermittelreibung. *Archiv für Elektrotechnik*, 3(1):1–5, 1914.

[82] H. Spikes. Mixed lubrication-an overview. *Lubrication Science*, 9(3):221–253, 1997.

[83] H. Spikes. Film-forming additives-direct and indirect ways to reduce friction. *Lubrication Science*, 14(2):147–167, 2002.

[84] Spurk and Aksel. *Fluid Mechanics*. Springer, Cham, 3rd edition, 2020.

[85] R. Stribeck. Die wesentlichen Eigenschaften der Gleit-und Rollenlager. *Zeitschrift des Vereines Deutscher Ingenieure*, 46(36):1341–1348, 1902.

[86] G. Vaitkunaite, C. Espejo, B. Thiebaut, A. Neville, and A. Morina. Low friction tribofilm formation and distribution on an engine cylinder tested with MoDTC-containing low viscosity engine lubricants. *Tribology International*, 171:107551, 2022.

[87] G. Vaitkunaite, C. Espejo, C. Wang, B. Thiebaut, C. Charrin, A. Neville, and A. Morina. MoS2 tribofilm distribution from low viscosity lubricants and its effect on friction. *Tribology International*, 151:106531, 2020.

[88] A. Vakis, V. Yastrebov, J. Scheibert, L. Nicola, D. Dini, C. Minfray, A. Almqvist, M. Paggi, S. Lee, G. Limbert, et al. Modeling and simulation in tribology across scales: An overview. *Tribology International*, 125:169–199, 2018.

[89] C. H. Venner and A. A. Lubrecht. *Multi-level methods in lubrication*. Elsevier, Amsterdam, 2000.

[90] E. A. Vollebregt. A new solver for the elastic normal contact problem using conjugate gradients, deflation, and an FFT-based preconditioner. *Journal of Computational Physics*, 257:333–351, 2014.

[91] Q. Wang, L. Sun, X. Zhang, S. Liu, and D. Zhu. FFT-Based Methods for Computational Contact Mechanics. *Frontiers in Mechanical Engineering*, 6:61, 2020.

[92] Y. Wang, A. Dorgham, Y. Liu, C. Wang, M. C. Wilson, A. Neville, and A. Azam. An assessment of quantitative predictions of deterministic mixed lubrication solvers. *Journal of Tribology*, 143(1):011601, 2020.

[93] Y. Wang, Y. Liu, and Y. Wang. A method for improving the capability of convergence of numerical lubrication simulation by using the PID controller. In *IFToMM World Congress on Mechanism and Machine Science*, pages 3845–3854. Springer, 2019.

[94] T. Woloszynski, P. Podsiadlo, and G. W. Stachowiak. Efficient Solution to the Cavitation Problem in Hydrodynamic Lubrication. *Tribology Letters*, 58(18), 2015.

[95] H. Zhang, W. Wang, S. Zhang, and Z. Zhao. Elastohydrodynamic lubrication analysis of finite line contact problem with consideration of two free end surfaces. *Journal of Tribology*, 139(3):031501, 2017.

[96] S. Zhang and C. Zhang. A New Deterministic Model for Mixed Lubricated Point Contact With High Accuracy. *Journal of Tribology*, 143:1–33, 2020.

[97] D. Zhu. On some aspects of numerical solutions of thin-film and mixed elastohydrodynamic lubrication. *Proceedings of the Institution of Mechanical Engineers, Part J: Journal of Engineering Tribology*, 221(5):561–579, 2007.

[98] D. Zhu and Q. J. Wang. Elastohydrodynamic Lubrication: A Gateway to Interfacial Mechanics-Review and Prospect. *Journal of Tribology*, 133(4):041001, 2011.

[99] L. Zhu, J. Dong, and Q. Zeng. High temperature solid/liquid lubrication behaviours of DLC films. *Lubrication Science*, 33:229–245, 2021.

Journal Publications

[Hansen et al., 2020] Hansen, E., Frohnapfel, B., and Codrignani, A. (2020). Sensitivity of the Stribeck Curve to the Pin Geometry of a Pin-on-Disc Tribometer. *Tribology International*, 151:106488.

[Hansen et al., 2022] Hansen, E., Kacan, A., Frohnapfel, B., and Codrignani, A. (2022). An EHL Extension of the Unsteady FBNS Algorithm. *Tribology Letters*, 70(3):1–25.

[Hansen et al., 2023] Hansen, E., Vaitkunaite, G., Schneider, J., Gumbsch, P., and Frohnapfel, B. (2023). Establishment and Calibration of a Digital Twin to Replicate the Friction Behaviour of a Pin-on-Disk Tribometer. *Lubricants*, 11(2):75.

Conference Contributions

[HFC19] E. Hansen, B. Frohnapfel, and A. Codrignani. Sensitivity of the Stribeck Curve to the Macroscopic Geometry of the Pin-on-Disc Tribometer (Poster). In *46th Leeds-Lyon Symposium on Tribology*, Lyon, France, 2019.

[HFC22] E. Hansen, B. Frohnapfel, and A. Codrignani. An EHL Extension of the FBNS Algorithm (Presentation). In *7th World Tribology Congress*, Lyon, France, 2022.

[HVS+23] E. Hansen, G. Vaitkunaite, J. Schneider, P. Gumbsch, and B. Frohnapfel. Scaling of Friction Behaviour in the Mixed Lubrication Regime through a Modified Hersey Number (Presentation). In *77th STLE Annual Meeting & Exhibition*, Long Beach, USA, 2023.

Code Repositories

[Han21] E. Hansen. MATLAB solver for the deformation of an elastic half-space based on the Boundary Element Method (BEM). https://github.com/ErikHansenGit/Contact_elastic_half-space, commit d32c3f548d8e77b2825f576265593743064de6e1 on 01.12.2021.

[Han22] E. Hansen. MATLAB solver for Elastohydrodynamic Lubrication (EHL) problems. https://github.com/ErikHansenGit/EHL, commit ba58141fdaccbe3633eacdc2881adce1a3720388 on 01.08.2022.

[Han23] E. Hansen. Exemplary code and data files for the submission of the article "Establishment and Calibration of a Digital Twin to Replicate the Friction Behaviour of a Pin-on-Disk Tribometer" [Hansen et al., 2023] in Lubricants. https://zenodo.org/records/7540491, 16.01.2023.

Co-supervised Theses

[Ell22] N. Ellenbogen. Numerische Untersuchung von Geometrieeinflüssen in einem Stift-Scheibe Tribometer. Bachelor's Thesis, 2022.

[Kaç21] A. Kaçan. Unsteady Numerical Simulation of the Pressure Distribution in a Ball-on-Disc Tribometer. Bachelor's Thesis, 2021.

[Kra22] J. Krause. Flux Limiter Implementation in a MEHL Solver. Master's thesis, 2022.

[Sam22] M. Samuel. Numerische und experimentelle Untersuchung von Welligkeiten in einem Stift-Scheibe Tribometer. Bachelor's Thesis, 2022.

[Wan21] S. Wang. Numerische Untersuchung von Oberflächentexturen in einem Stift-Scheibe Tribometer. Bachelor's Thesis, 2021.

[Yse21] T. Ysermann. Numerische Untersuchung des Anstellwinkels in einem Stift-Scheibe Tribometer. Bachelor's Thesis, 2021.

Nomenclature

Latin letters – Upper case

SYMBOL	SI UNIT	DESCRIPTION
A		matrix with homogenization factors of the Reynolds equation
A_{dpl}	m^2	projected dimple area
A_h		matrix with pressure coefficients due to the Couette term
A_{Po}		matrix with pressure coefficients due to the Poiseuille term
A_{dpl}	m^2	unit triangle area
A_{trib}	m^2	tribological contact area
B		matrix with cavity fraction coefficients due to the Couette term
C		matrix with homogenization factors of the homogenized viscous stresses of the fluid
C_1	Pa	constant of the Dowson-Higginson model
C_2		constant of the Dowson-Higginson model
C_f		friction coefficient
$C_{f,b}$		boundary friction coefficient
$C_{f,dev}$		deviation of the friction coefficient in relation to the boundary friction coefficient
D	m	pin diameter
D_{dpl}	m	distance to dimple center
E	Pa	Young's modulus
E'	Pa	reduced elastic modulus
Eu		Euler number
F		non-dimensional Fischer-Burmeister equation
F_N	N	normal force
$F_{N,imp}$	N	imposed normal load
F_T	N	friction force
Fr		Froude number
$\vec{F}$		vector with discrete non-dimensional Fischer-Burmeister equations
G		non-dimensional Reynolds equation
$\vec{G}$		vector with discrete non-dimensional Reynolds equations

H	m	characteristic gap height
Hrd	Pa	hardness
$\mathcal{H}$		Hersey number
J		Jacobian matrix of the FBNS algorithm
K		kernel
K_D, K_I, K_P		coefficients of the PID controller
L	m	characteristic length in the direction of U
L_{txt}		texturing length
L_{x_1}, L_{x_2}	m	geometry length and width
N		spatial grid resolution
$N_{1,R}$, $N_{2,R}$		amount of the rectangular discretization cells on the surface of an elastic half-space in the respective direction
N_{it}		amount of iterations
N_t		amount of discrete time steps
$N_{X_1,R}$, $N_{X_2,R}$		amount of the rectangular discretization cells on the surface of an elastic half-space in the respective direction of the macroscale
N_{x_1}, N_{x_2}		amount of discretization cells in the respective direction
$N_{r,1}$, $N_{r,2}$, $N_{r,t}$		amount of the averaged discretization cells in space and time on the microscale
$N_{\xi_1,R}$, $N_{\xi_2,R}$		amount of the rectangular discretization cells on the surface of an elastic half-space in the respective direction of the microscale
R_{x_1}	m	radius of ball curvature in x_1-direction
Re		Reynolds number
SSR		slide-to-roll ratio
S_q	m	root-mean-square value of the roughness patches when the zero-height mark of the patch is at its mean plane
$\mathcal{S}$		Sommerfeld number
T	s	macroscopic time
Trq_{x_1}, Trq_{x_2}	N m	resulting torques around the respective axis
U	$\mathrm{m\,s^{-1}}$	sliding velocity
U_{up}	$\mathrm{m\,s^{-1}}$	velocity of the upper surface
U_{low}	$\mathrm{m\,s^{-1}}$	velocity of the lower surface
W_{txt}		texturing width
X_1, X_2	m	macroscopic coordinate components

Latin letters – Lower case

SYMBOL	SI UNIT	DESCRIPTION
a	m	length of the rectangular discretization cell on the surface of an elastic half-space
b	m	width of the rectangular discretization cell on the surface of an elastic half-space
$\vec{b}$		vector with homogenization factors of the Reynolds equation
$\vec{c}$		vector with constants of the Reynolds equation
d_{dpl}	m	dimple diameter
$\vec{d}$		vector with homogenization factors of the homogenized viscous stresses of the fluid
$e_{fl,ij}$	s^{-1}	strain rate tensor
$e_{sl,ij}$		strain tensor
g	$\mathrm{m\,s}^{-2}$	gravitational acceleration
h	m	gap height
h_0	m	macroscopic gap height
$h_{0,d}$	m	rigid body displacement on the macro-scale
$h_{0,el}$	m	elastic gap height deformation on the macro-scale
$h_{0,ri}$	m	rigid variation of the gap height due to the shape of the surfaces on the macro-scale
h_1	m	microscopic variation of the gap height
$h_{1,el}$	m	elastic contribution of the microscopic variation of the gap height
$h_{1,ri}$	m	rigid contribution of the microscopic variation of the gap height
h_d	m	rigid body displacement
h_{dpl}	m	dimple depth
h_{el}	m	elastic gap height deformation
h_{max}	m	maximum inlet gap height of a slider
h_{min}	m	minimum gap height of a slider
h_p	m	pocket depth of a slider with pocket
h_{ri}	m	rigid variation of the gap height due to the shape of the surfaces
$\overline{h}$	m	mean gap height
k_1, k_2, k_3	$\mathrm{m\,s}^{-2}$	components of gravitational acceleration
l_{in}	m	inlet length of slider with pocket
$l_{B,txt}$	m	base length of unit triangle
$l_{H,txt}$	m	height of unit triangle
l_h	m	step length

l_p	m	pocket length of slider with pocket
p	Pa	reduced pressure
p_0	Pa	macroscopic reduced pressure
p_1	Pa	microscopic variation of the reduced pressure
$p_{0,fl}$	Pa	macroscopic fluid pressure
p_{amb}	Pa	ambient pressure
p_{asp}	Pa	asperity contact pressure
p_{cav}	Pa	cavitation pressure
p_{con}	Pa	contact pressure
p_{fl}	Pa	fluid pressure
p_{tot}	Pa	total pressure
$\overline{p}_{con}$	Pa	mean contact pressure
r		residual
r_a	m	radius of Hertzian contact
r_{dpl}	m	dimple radius
r_H	m	holding radius
r_S	m	sliding radius
r_τ		gap height fraction
s_h	m	shoulder height
t	s	time
tol		tolerance
u_1, u_2, u_3	$\mathrm{m\,s^{-1}}$	velocity components
u_{dpl}	$\mathrm{m\,s^{-1}}$	dimple velocity
u_m	$\mathrm{m\,s^{-1}}$	mean entrainment velocity
u_r	$\mathrm{m\,s^{-1}}$	relative velocity
v_1, v_2, v_3	m	displacement components
v_1', v_2', v_3'	m	components of combined displacement
w	m	pocket width of slider with pocket
x_1, x_2, x_3	m	coordinate components
$\overline{x}_3$	m	auxiliary height coordinate
$x_{1,0}, x_{2,0}$	m	coordinate components of the initial dimple center
$x_{1,dpl}, x_{2,dpl}$	m	coordinate components of the dimple center
$x_{1,R}, x_{2,R}$	m	coordinate components of the center of the rectangular discretization cell on the surface of an elastic half-space
$\tilde{x}_1, \tilde{x}_2$	m	distances to the center of the rectangular discretization cell on the surface of an elastic half-space

z_{up}	m	x_3-position of the upper surface
z_{low}	m	x_3-position of the lower surface

Greek letters – Upper case

SYMBOL	SI UNIT	DESCRIPTION
Δt	m	time step length
Δx_1, Δx_2	m	spacing of discretization cells in the respective direction
Ω	$\mathrm{rad\,s^{-1}}$	angular velocity

Greek letters – Lower case

SYMBOL	SI UNIT	DESCRIPTION
α_B, α_R	$\mathrm{Pa^{-1}}$	pressure viscosity coefficients of the Barus and Roelands model
α_{p^*}, α_θ, $\alpha_{\overline{p}^*_{con}}$		relaxation factors of non-dimensional reduced pressure, cavitity fraction and mean contact pressure
α_{tri}	°	angle of the unit triangle
α_{x_1}, α_{x_2}	°	levelling angles around the respective axis
β_{tri}	°	angle of the unit triangle
γ_{tri}	°	angle of the unit triangle
δ_{ij}		Kronecker delta
$\vec{\delta}$		update vector of the FBNS algorithm
ϵ		magnitude ratio of macro- and microscale
ε		machine expsilon
η_{txt}		texture efficiency
θ		cavity fraction
κ	s	microscopic time
λ_{dpl}		dimple aspect ratio
λ_κ	s	periodic time span on the microscale
λ_{ξ_1}, λ_{ξ_2}	m	periodic length and width on the microscale
μ	Pa s	dynamic viscosity
μ_0	Pa s	dynamic viscosity of the lubricant's liquid phase at ambient pressure
μ_l	Pa s	dynamic viscosity of the lubricant's liquid phase
ν		Poisson ratio
ξ_1, ξ_2	m	microscopic coordinate components
ξ^*_{Co}		coefficient of Couette term in the dimensionless Reynolds equation

ξ^*_{Po}		coefficient of Poiseuille term in the dimensionless Reynolds equation
ξ^*_{Ti}		coefficient of unsteady term in the dimensionless Reynolds equation
κ	s	microscopic time
ρ	$\mathrm{kg\,m^{-3}}$	density
ρ_0	$\mathrm{kg\,m^{-3}}$	density of the lubricant's liquid phase at ambient pressure
ρ_l	$\mathrm{kg\,m^{-3}}$	density of the lubricant's liquid phase
ρ_{txt}		texturing density
σ_{ij}	Pa	stress tensor
τ_{ij}	Pa	viscous stress tensor
$\tau_{con,1}$	Pa	tangential stress due to surface contact
$\tau_{fl,1}$, $\tau_{fl,2}$	Pa	viscous stresses of the fluid
τ_{tot}	Pa	total tangential stress
$\overline{\tau}_{con,1}$	Pa	mean tangential stress due to surface contact
$\overline{\tau}_{fl,1}$, $\overline{\tau}_{fl,2}$	Pa	homogenized viscous stresses of the fluid
χ_1	$\mathrm{m^{-1}}$	solution of the first local problem
χ_2, χ_3	m	solution of the second and third local problem

Subscripts

SYMBOL	DESCRIPTION
$*$	non-dimensional quantity
C	center cell
EB	east boundary cell
i	tensor dimension
j	tensor dimension
low	lower surface
NB	north boundary cell
n	iteration
ref	reference quantity
SB	south boundary cell
up	upper surface
WB	west boundary cell

Abbreviations

SYMBOL	DESCRIPTION
CFD	computational fluid dynamics
CG	conjugate gradient
EHL	elasto-hydrodynamic lubrication
FBNS	Fischer-Burmeister-Newton-Schur
FDM	finite difference method
FEM	finite element method
FFT	fast Fourier transform
FVM	finite volume method
HMEHL	homogenized mixed elasto-hydrodynamic lubrication
IAM-ZM	Institute of Reliability and Microstructure
JFO	Jakobsson-Floberg-Olsson
LBE	load balance equation
NDE	Navier's displacement equations
NSE	Navier-Stokes equations
PID	proportional integral derivative
QUICK	quadratic upwind interpolation
UI	upwind interpolation

List of Figures

List of Tables

Acknowledgements

I would like to thank my doctoral adviser Prof. Dr.-Ing. Bettina Frohnapfel for providing the free and creative research environment that allowed me to follow various research directions and productively develop ideas. Furthermore, I would like to express my gratitude to Prof. Dr. Peter Gumbsch and Dr.-Ing. Johannes Schneider for their highly valuable input during discussions in the course of a collaborative research project. Special thanks go to my project partner Dr. Gerda Vaitkunaite at IAM-ZM who trained me on topography measurement devices, supplied excellent experimental data and crucially contributed to the progress of the collaborative research project. Funding wise, this research would not have been possible without the highly appreciated support from the Friedrich und Elisabeth Boysen-Stiftung and the Deutsche Forschungsgemeinschaft (DFG Project Number 438122912). Moreover, I would like to express my gratitude to Dr.-Ing. Andrea Codrignani, Dr.-Ing. Davide Gatti, Dr.-Ing. Lukas Oestringer and Dr. Yuechang Wang who greatly supported me with their knowledgeable input during discussions of scientifically highly specific subjects. Lastly, I want to thank the thesis students and research assistants Jan Krause, Mikel Samuel, Noah Ellenbogen, Shuhang Wang, Christian Sax, Simon Dalpke, Altay Kaçan and Timo Ysermann who helped me by preliminarily testing various ideas in the course of their work.